Doctoral Thesis

Structural Condition Assessment of Existing Steel Bridges Based on Non-destructive Evaluation.

2023.03

Gifu University
Graduate school of engineering Doctorate program
Mechanical and Civil Engineering Division

Supervised by Koji KINOSHITA

Barasa Anthony KUSIMBA

Table of Contents

List of Figures

Chapter 1

Chapter 2

Chapter 3

Chapter 4

Chapter 5

List of Tables

Chapter 1

Chapter 2

Chapter 3

Chapter 4

Acknowledgement

I appreciate the inspiration of various persons and institutions; Gifu University, Japan International Cooperation (JICA) vide Road Asset Management Program (RAMP) and Kenya National Highway Authority (KeNHA) for the support and assistant offered in the entire period I conducted this study.

Most importantly, I would like to express my sincere gratitude to my supervisor Associate Professor Koji KINOSHITA for his advice, thoughtful suggestions, patience, continuous motivational and support of my Doctoral research Study. His intellectual inspirations and invaluable insight were instrumental and helpful throughout the Doctoral course.

Besides my supervisor, I would like to thank my co-supervisor Professor Yuichi UCHIDA and the thesis committee: Professor(s) Koichi KOBAYASHI and Minoru KUNIEDA for their immense push that culminated into finalising the research.

I would also wish to thank Assistant Professor Yuki BANNO for his tireless effort toward seeing me through. Additionally, I would also candidly express thanks my seniors Mr. Inoue KAZUMA and Mr. Takahashi MUSAMUNE former lab mates Mr. Kiyoaki SUGAWA, Mr. Ryosuke FUKAMI and Mr. Tshewang RINZIN; present lab-mates Mr. Takehisa NOUDO, Mr. Takahiro IWATA, Mr. Yuta MEZAKI, Mr. Al Amin SIKDER, Mr. Ahmadzai NIAMATULLAH, Ms. Rie BAMBA, Mr. Sasaki YUYA, Ms. Yukina TAKAI, Mr. Tsuruta MOTOHIKO, Mr. Watanabe KAZUKI, Mr. Saito KYOHEI, Mr. Adachi DAIGO, and Mr. Sasaki SHUN.

I would like to acknowledge Ms. Yumi AKIYAMA for her seamless administrative role during my entire study.

Finally, I would like to thank my family, Aiden NAKTARE and Mrs. Mideva KUSIMBA; parents Mr. and Mrs. Barasa KUSIMBA for the support offered through the entire period of my research, emotional and social life in general. Their inescapable optimism and love have driven me to date.

Barasa A. Kusimba

Abstract

The geography of Japan requires reliable transportation infrastructure. Additionally, natural disasters, for instance earthquakes, tsunamis and typhoons are a common phenomenon in the nation. As such the existing infrastructure is at risk. Road assets such as bridges are most common in overcoming the wanting terrain. Bridge structures constitute the largest percentage in road assets ranging from beam, arch, truss, cantilever, suspension, and cable stayed bridges. However, steel bridges are the most predominant structures due to their reliability to withstand the phenomena, ease in fabrication and readily available as the primary material of bridges. Most of these structures were commissioned in the 1970s towards the onset of the 21st century and as such more than two decades old at minimum. The situation is predicted to rise in two-fold annually. As a result, fatigue cracks and corrosion due to aging are the most common issues accelerating degradation exhibited by the rampant number of traffic restrictions on prefectural and municipal roads. The reliability and safety of the now in use structures are encouraging structural inspection (intermittent and periodic). The conventional inspection methods have inherent shortcomings from inspection manuals, availability of structural information (as-built drawings and previous inspection results) to inspection methods.

Therefore, this thesis focused on in-situ, ex-situ, and analytical experimentation as cases to project the prevailing conditions. The primary purpose of inspection is to assess structural conditions through examining the bearing capacity and structural degradation deploying non-destructive evaluation approaches. Hence it is prudent to develop innovative inspection techniques short of predispositions. Owing to this the thesis addressed the prospects of non-destructive evaluation (NDE) for structural health monitoring; evaluated the condition and adaptation of steel bridges, proposed a framework based on existing manuals for evaluating the bearing capacity of an in-service bridge and finally propose a fatigue crack inspection approach by proposing an alternative surface fatigue crack evaluation method based on principles of fracture mechanics. Consequently, this thesis was based on the latter concerns to generally investigate NDE approaches based on structural health degradation of existing steel bridges and specifically:

1. Reviewing the prospects of NDE(s) and their suitability for Structural Health Monitoring.
2. A research based on the condition assessment of steel bridges deploying finite element/numerical models for structural analysis validated with in-situ measurements through loading tests will be put forward.
3. A technique for evaluating the bearing capacity will be researched and presented using the structural resistance of critical members and a framework developed for adaptation of steel structures from temporary to permanent.
4. Propose an ex-situ and in-situ fatigue crack inspection approach utilizing Static and Transient Thermography in both Active and Passive domains.

Inspection of aging structures is vital to ensure safety of users and alleviate financial predicaments to the owner. Through incorporating Non-destructive evaluation, it is viable to bring into focus issues relating to structural degradation. The review covered NDE approaches based on:

1. Limited historical data
2. Surface fatigue crack evaluation

Most of the steel structures are old thus degraded to some extent. However, some of them are still used for more than a century. Rapid replacement of the same subjects the owner to unwanted financial demands. The deployment of optimized maintenance approach to curb on the degradation was envisioned through presenting NDE inspection approaches based on the two issues. The review presented the classification of the technology into acoustic, vision-based, magnetic, penetrant, and thermal methods, their popularity was based on the reviews over the years, and best practices from a global perspective through cases. Further, it reviewed how the approaches can be integrated for evaluation for steel structures and check for accuracy through developing/proposing a framework for bridge inspection.

The study further assessed the condition and adaptation of a bailey bridge as a semi-permanent or permanent structure. The investigation was both done on site through dynamic static loading tests and responses drawn from suitable acoustic methods and vison-based methods. The structure was then numerically modelled through onsite geometric, material properties and validated for accuracy using Linear analysis i.e., Newton Raphson method. The digital model was deployed to check for resistance of members employing linear buckling analysis and further nonlinear analysis using nonlinear buckling to check for the limit states. The findings i.e., bearing capacity, and structural health conditions were then used to formulate a framework for adaptation as a permanent structure.

Additionally, surface fatigue cracks were evaluated under laboratory conditions to develop and an approach for onsite evaluation. First, the study used active thermography under steady/static and transient domain for fatigue crack sizing and establishing its sensitivity against other approaches of fatigue characterization. Plate bending fatigue testing machines were used to simulate fatigue on welded sections. The fatigue initiation and failure were denoted according to the fatigue life of the given specimen. The technique was thus checked for deployability and being employed as an alternative fatigue characterization approach on welded joints. Secondly, the approach developed was deployed passively to evaluate the reliability of fatigue life extension using Impact crack Closure Retrofit (ICR).

Basically, the author proposed from literature NDE based approaches for evaluation of structural health condition through accurately determining its dynamic and static response. He further developed a numerical model using onsite geometric and material data and validated with onsite response. The author addressed structural limit states by buckling analysis. Consequently, a numerical formed the basis of the initial database for inspection of the steel structure deployed for monitoring structural degradation. Hence, summarised a framework for adaptation and inspection of steel structures. Thermal Non-destructive Evaluation was established as an alternative, noninvasively, and sustainable screening technique for fatigue crack characterization.

Keywords*: bailey bridge, bearing capacity, bending moment, deformation, deflection, static and dynamic loading, historical data, Fatigue crack inspection, Welded joint, Active thermography, passive thermography.*

Chapter 1

Introduction

1.1. Background

The challenging landscape of Japan deems it necessary to have a reliable transportation infrastructure. Moreover, natural disasters such as earthquakes, tsunamis, and typhoons are common in the country [1]. The former impedes the use of the existing infrastructure. Bridges are peradventure the most common infrastructural asset to overcome distinctive terrain in the country. The bridge structures constitute 730000 in road assets [2] presented in Figure 1.1. The bridges range from the beam, arch, truss, cantilever, suspension to cable-stayed types. Steel bridges (48%) are the widely used due to their reliable performance as illustrated in Figure 1.2. Steel bridges can primarily and at ease withstand natural disasters. Further, due to the nation's maturity in steel production sector, fabrication and cost are critical factors to their popularity [3].

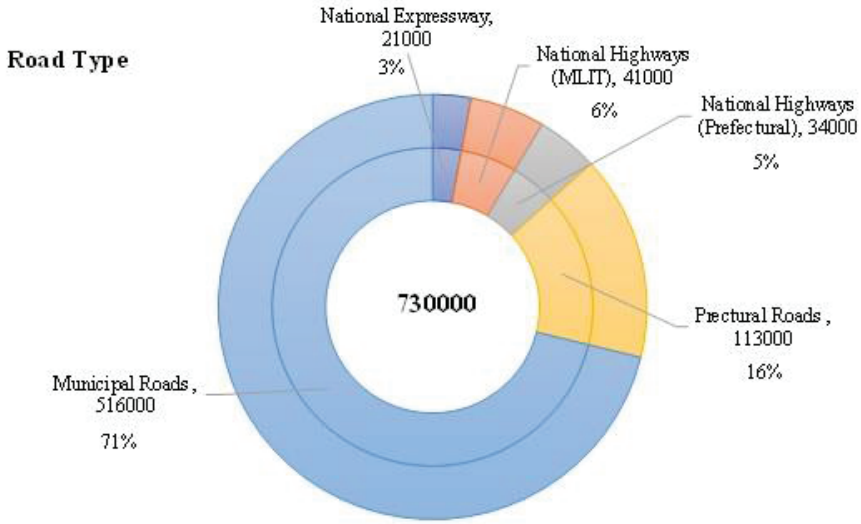

Figure 1.1. Bridges to Road Type (Japan Road Bureau-MLIT, 2018 & 2021).

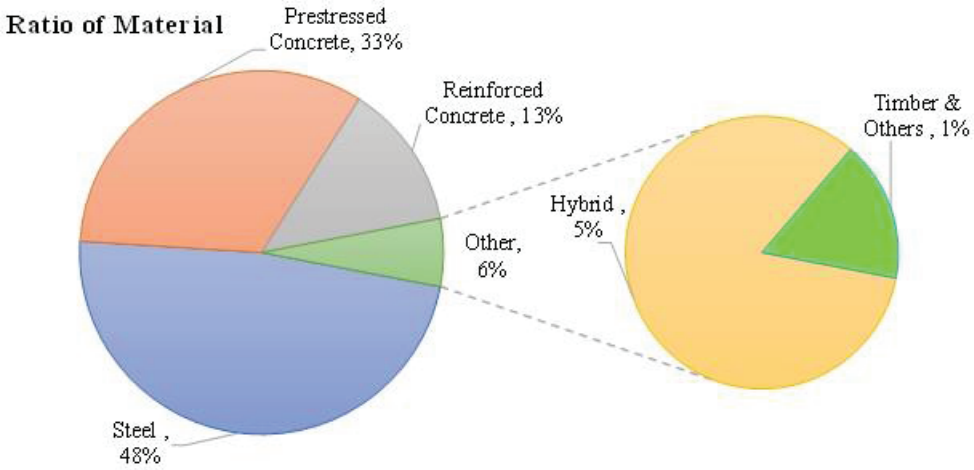

Figure 1.2. Ratio of Material to Bridge (Japan Road Bureau-MLIT, 2018 & 2021)

However, most of the steel bridges were built before the 1970s to early 2000s [3] as observed by the consumption of steel during the mentioned period as demonstrated in Figure 1.3. Hence, they are more than or approximately 22-50 years old, projected to be higher than 43% by 2023 and 67% by 2033 while progressively rising in two-fold per annum. Therefore, deformation due to aging has become noticeable and predominantly associated with corrosion and fatigue cracks [4] as shown in Figure 1.4. Traffic restrictions [5] on municipality bridges have increased twice over the past five years on structures longer than 2 m [6]. It is evident maintenance rather than construction has become a norm giving credence to the 2013 infrastructure maintenance era declaration. Additionally, new insights concerning the development in measurement and maintenance are envisioned through research. Consequently, there are doubts about the existing steel bridge structures concerning their safety and reliability, encouraging intermittent and periodic inspection.

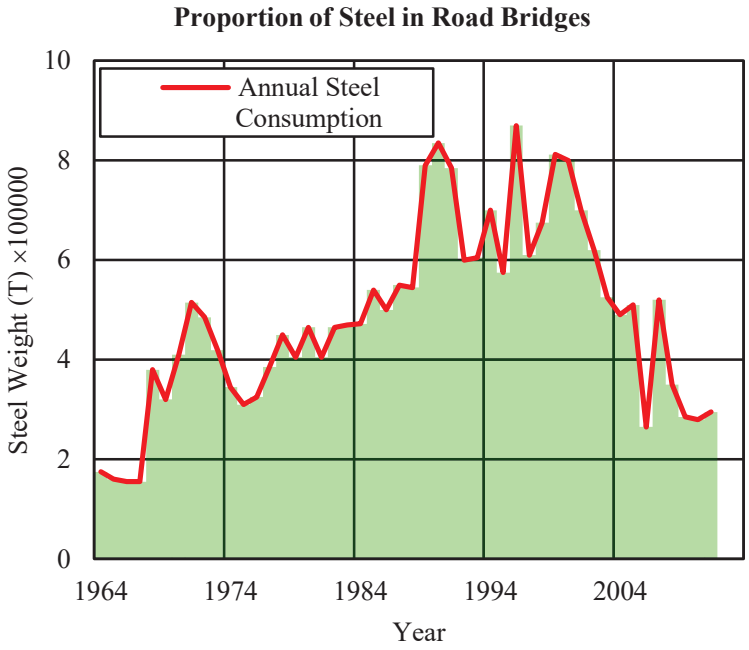

Figure 1.3. Annual Steel Consumption of the Steel Bridge Market (Fujino et. al., 2016)

Figure 1.4. Miharashi Bridge - Yokohama City - Constructed in 1978 (MLIT, 2015)

Structural maintenance starts with inspection, which, when wrongly done, cannot guarantee the structure's safety. Under this prevailing circumstance, this thesis will focus on steel bridges, mainly in-situ and ex-situ experimentation, to project the bigger picture. The primary purpose of a bridge inspection is to assess the subject bridge condition (fatigue and corrosion), determine the as built drawings and design documents, response (due to missing members or rigidity), determine causes of damage if any, examine the rate of deterioration, evaluate the urgency of repair or rehabilitation and bearing capacity. Some of the steel bridges, for instance the bailey bridges within the country were built to serve as temporary structures [7] for transporting material during the construction of major highways. Thus, most of them are partially abandoned and are typified by maintenance issues. According to the 2013 ordinance declaration [6], the classical inspection (periodic - 5 years) approach commences with a short range visual inspection, reporting on underlying issues and diagnosis of the outcomes, similar to the Kingdom of Cambodia Bridge inspection manual [8]. However, the conventional method illustrated

in Table 1.1 is subjective or biased based on the current inspector; the results are founded on conservative assumptions; time-consuming because most of the activities are manual; it is not clear in the absence of historical data, limited work force and the safety of the individual is not addressed culminating to a costly exercise as relayed in Figure 1.5.

As a result, it is prudent to adopt innovative techniques [9] to demonstrate that the inspection is devoid of predispositions; employ empirical methods; automate; address limitations on records and ensure safety conditions are fulfilled to reduce or avoid maintenance and replacement costs [8,9]. One of the most feasible methods is deployment of analytical, field experimentation, in-situ, and ex-situ Non-Destructive Evaluation (NDE) oriented to certify the structural integrity. The immediate deployment of these approaches is essential for the management of the deteriorating road asset.

Table 1.1. Schedule of Conventional Evaluation (Min. of Public Works & Transport Kingdom of Cambodia, 2018)

Phase	Item	Exercise	State
i	Review of previous inspection reports	Evaluate design records	in + ex situ
ii	Resources: Equipment, safety	Planning	
iii	Evaluation of performance & Deterioration	Visual inspection Testing	ex-situ
iv	Identification of probable triggers	Diagnosis	

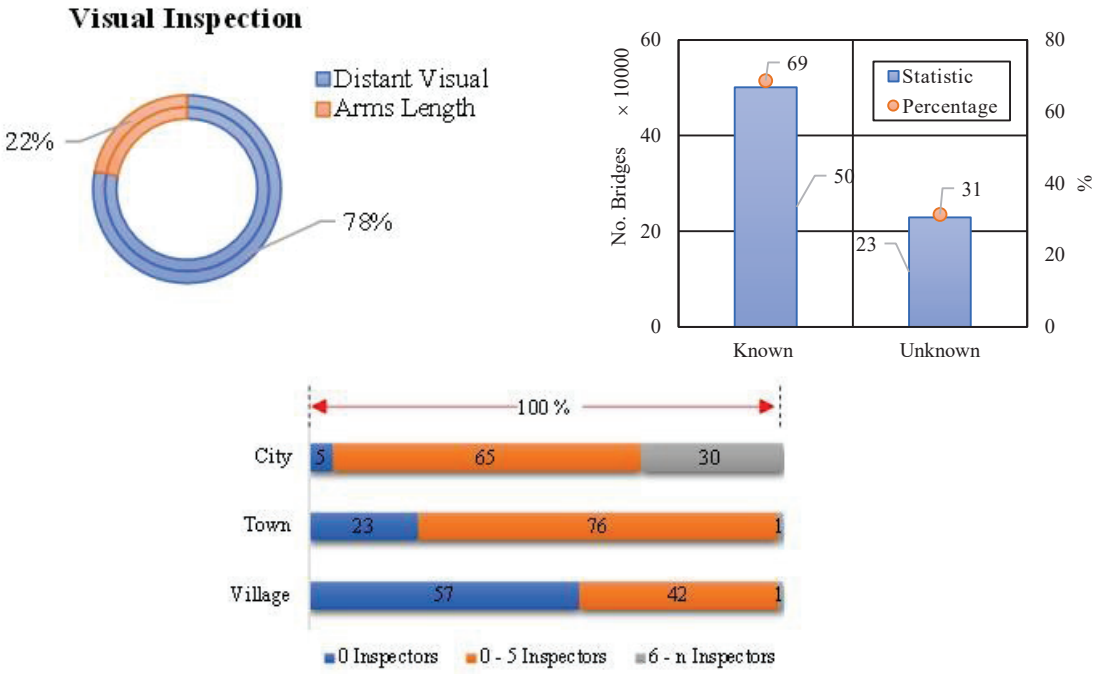

Figure 1.5. Visual Inspection, Structures with no Historical Data and Statistics for Inspection personnel (MLIT, 2021).

Subsequently, conventional methods for structural inspections have presented their limitations. The main reason for the limited focus was due to the period of rapid infrastructural expansion that posed no significant problem to steel structures between the 1960s to 2000s. However, a considerable number of structures have approached or surpassed their design life [2]; out-dated codes/manuals and traffic loads have tremendously changed; hence maintenance has become a concern. The illustration which is a depiction of the deterioration curve explains how maintenance is key to prolonged structural life, as illustrated in Figure 1.6. In essence repairs comprise of inspection that is enshrined in a maintenance plan. If the service life of a structure is defined as say $\boldsymbol{x}$ years, an example; repair works should commence prior to the prescribed service life. Most bridges are in urban areas where the classical methods are no longer suitable.

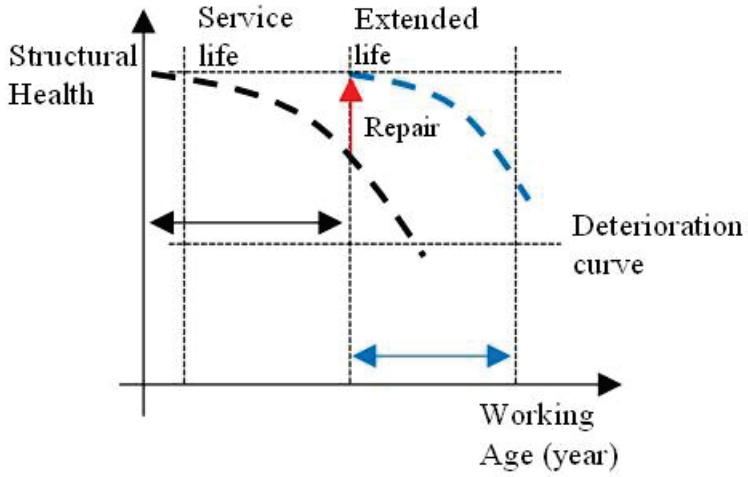

Figure 1.6. Structural Service Life

1.2. Aims of this thesis

Owing to the current structural conditions, maintenance takes precedence over construction hence inspection. The word structure solely means steel structure in this thesis. Proposing Non-Destructive Evaluation (NDE) methods is essential for effectively maintaining — inspection of the existing structures. This thesis' trajectory will be based on four concerns hereafter listed:

1. The prospects of NDE methods for assessing the current structural conditions, integrity, and redundancy are not well documented.
2. The shortcomings of the assumptions made from models fundamental in computer-based structural analysis programs are not supplemented and addressed.
3. The evaluation approaches of structural analysis of individual members in the ultimate limit state are conservative hence limited in adaptation.
4. The in-situ and ex-site fatigue inspection technologies are limited on inspection records and limited in capacity to evaluate fatigue cracks using the principles of fracture mechanics; thus, they are not simply integrative.

The thesis strives to report the abovementioned concerns with cases (steel bridges and specimens) carefully selected from Japan vide:

1. Reviewing the prospects of NDE(s) and their suitability for Structural Health Monitoring.
2. A research based on the condition assessment of steel bridges deploying finite element/numerical models for structural analysis validated with in-situ structural response measurement through loading tests will be put forward.
3. A technique for evaluating the bearing capacity will be researched and presented using the structural resistance of critical members and a framework developed for adaptation of steel structures from temporary to permanent.
4. Propose an ex-situ and in-situ fatigue crack inspection approach utilizing Static and Transient Thermography in both Active and Passive domains.

Based on the abovementioned specific objectives, this thesis' main objective was to investigate the structural condition of existing bridges based on Non-destructive evaluation.

1.3. Organization of this thesis

In Figure 1.7, the organization of this thesis is presented. This dissertation consists of 5 chapters with the introduction and summary of conclusions in Chapter **1** and **5**. The Literature Review, Field, Laboratory and Analytical experimentations contents are included in Chapters **2** to **4**.

Chapter 1: Introduction

This chapter discussed the background, concerns related to steel bridges and objectives of this thesis. In this thesis, to achieve the set objectives, the historical perspective was covered with respect to jurisdiction, current state of the structures and classical approaches for maintenance of the same.

Chapter 2: A Review based on Non-Destructive Evaluation for Monitoring Strength Degradation of existing steel bridges.

Findings from the literature review, presents the outcome of on the NDE based approaches that are deemed feasible in the present industry. The chapter discusses the NDE approaches based on two issues: limited historical data and surface fatigue crack evaluation, and it presents their basic approaches and best practices from a global perspective. Moreover, the chapter presents the theoretical approaches for load testing and attempt to propose a framework based on existing manuals.

Chapter 3: Non-Destructive Evaluation of the Structural Condition and Adaptation of temporary and existing Steel Bridges as permanent Structures

This chapter details a bailey bridge as the case for the research on steel bridge inspection. The study assessed the Bailey bridge's condition and investigated its adaptation as a permanent structure. Therefore, on-site diagnostic experiments were performed under various loading conditions, such as dynamic and static loading tests. The data was acquired using Acoustic and image processing methods (vision based NDE methods).

The bridge was then accurately modelled based on the in-situ geometric configuration of the bridge. The model's accuracy was validated with the onsite data and previous studies employing validation coefficient(s) courtesy of the solution from Newton's Raphson method from the numerical model. The model was deployed to check for resistance of critical members in the ultimate state using the Arc Length Method. The findings obtained in the study highlight the bridge's Structural Health Condition, bearing capacity, and eligibility for adaptation as a semi-permanent or permanent structure and will be used to formulate the framework for steel bridge inspection and adaptation.

Chapter 4: Fatigue crack inspection using thermographic techniques

This chapter presents the NDE approach using Thermal techniques for evaluation of fatigue analytically, on-site and laboratory for development of a fatigue evaluation approach. The study used static and transient thermography for fatigue crack inspection and characterization of welded joint(s). First, laboratory tests using plate bending fatigue test machine were performed to simulate fatigue crack scenarios that were then inspected

using an infrared thermal camera implementing Active Thermography (AT) from fatigue crack initiation — N_{toe} to failure — N_{20}. The method was then examined to check for reliability and accuracy for fatigue crack life extension approaches hence be proposed as an alternative qualitative and quantitative fatigue topology surface crack inspection method. In consequence, the approach was deployed onsite to assess the fatigue crack condition/situation before and after Impact Crack-closure Retrofit (ICR) for fatigue life extension.

Chapter 5: Summary of Conclusions

From the studies, the proposed framework is practically determined and summarised as a technical guide for management of temporary existing steel bridges (Chapter 3) and propose a remote, non-invasive, surface fatigue crack inspection approach (Chapter 4) and finally outline the research findings. An assorted study of Non-destructive Evaluation for the condition of existing steel bridges is summarised herein Figure 1.7. and recommendation for management of steel bridges proposed.

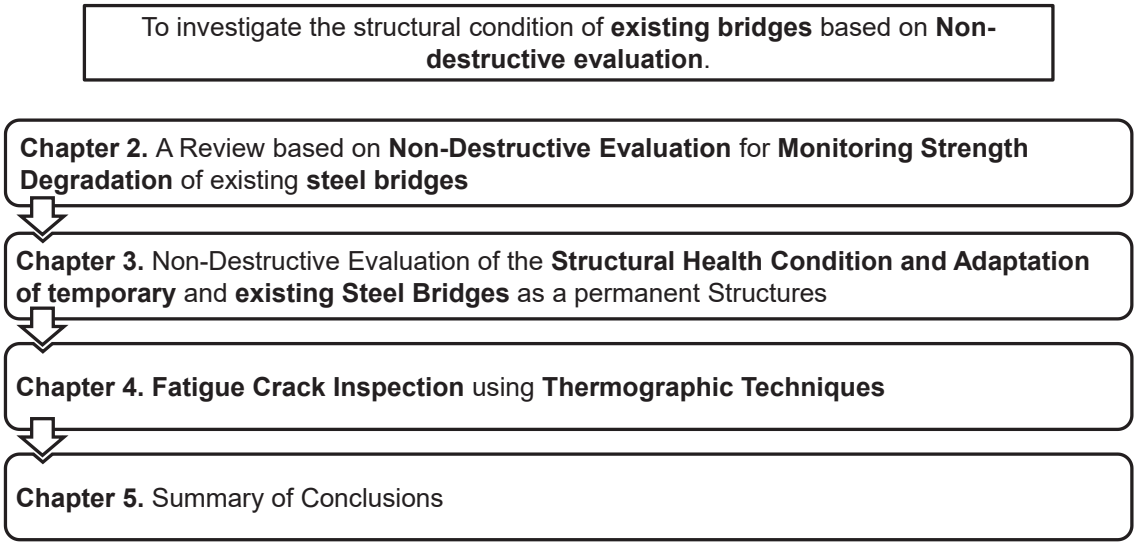

Figure 1.7. Organization of this thesis

Chapter 2

A Review Based on Non-Destructive Evaluation for Monitoring Strength Degradation of Existing Steel Bridges

2.1. Overview

2.1.1. Introduction

A growing number of bridge stocks need maintenance within Japan, with steel structures taking a larger percentage [2]. As the structure age, loading associated with the dynamic vehicular hammering leads to wear and tear, reducing its service life. Most of the structures were built two to five decades ago are manifested with aging issues [5]. The issues related to aging, span from the lack of historical data to fatigue crack of welded sections, are the most common and require immediate attention. Japan, through its declaration of 2013 [6], enforced the inspections of structures at a maximum of five-year intervals. Inspecting structural conditions is necessary to ensure serviceability and determine the course of action, for instance, repair or total replacement of the bridge. The 2013 declaration further recommends close visual inspection — arm's length, which has numerous issues ranging from being skewed, labour intensive, based on hypotheses, significant financial implications, and the wellbeing of the superintendent is put at risk. Additionally, 80% of the inspection manuals [5] from the municipalities recommend visual inspections at a distance that is in itself problematic due to numerous blind spots and overlooking. A cross ministerial approach was adopted through the Strategic Innovation Promotion Program (SIP). The program investigated five research fields from inspection; structural materials; information and communication; robotics, and asset management technologies, evaluating the need for innovative methods for inspection. Consequently, Non-Destructive Evaluation (NDE) [11] would play a critical role as remedy for the innate burden associated with classical methods that is evident on old steel structures greater than or equal to 22 years old.

2.1.2. Steel Structural Bridges

2.1.2.1. Classification of Steel Bridges

There are five basic types of steel bridges ranging from Girders to suspension bridges. The girder type steel bridges, have the flexure as the main structural action between their supports. They come in various nomenclatures such as simple spans, suspended and cantilevered spans. The Rigid frame type come with the longitudinal girders being continuous with the verticals or rather inclined supports by means of moment carrying joints through pins, bolts, facing plates or bolts. The main actions of this class of bridges includes flexure and axial forces. The Arch type of steel bridge is characterised by loads being transferred to the abutments through arches as the primary structural element with a combination of bending. Any horizontal thrust at the ends is controlled by a tie running longitudinally for the full span of both sides of the structure – bow string arch [12]. On the other hand, the cable stayed type is where the longitudinal girders are supported by ties in the vertical or inclined plane which hang from towers and anchored at the bottom of the girders [13]. Additionally, the suspension bridges structural form entails the decking section being suspended from cables spanning across the entirety of the span that are anchored at the two ends of the bridge and passing over tall towers installed near both ends [14]. This type of bridge is most common spanning across long stretches as illustrated in Figure 2.1 and Table 2.1.

Table 2.1. Classes of Steel Bridges and Typical span length (Chen et al, 2000).

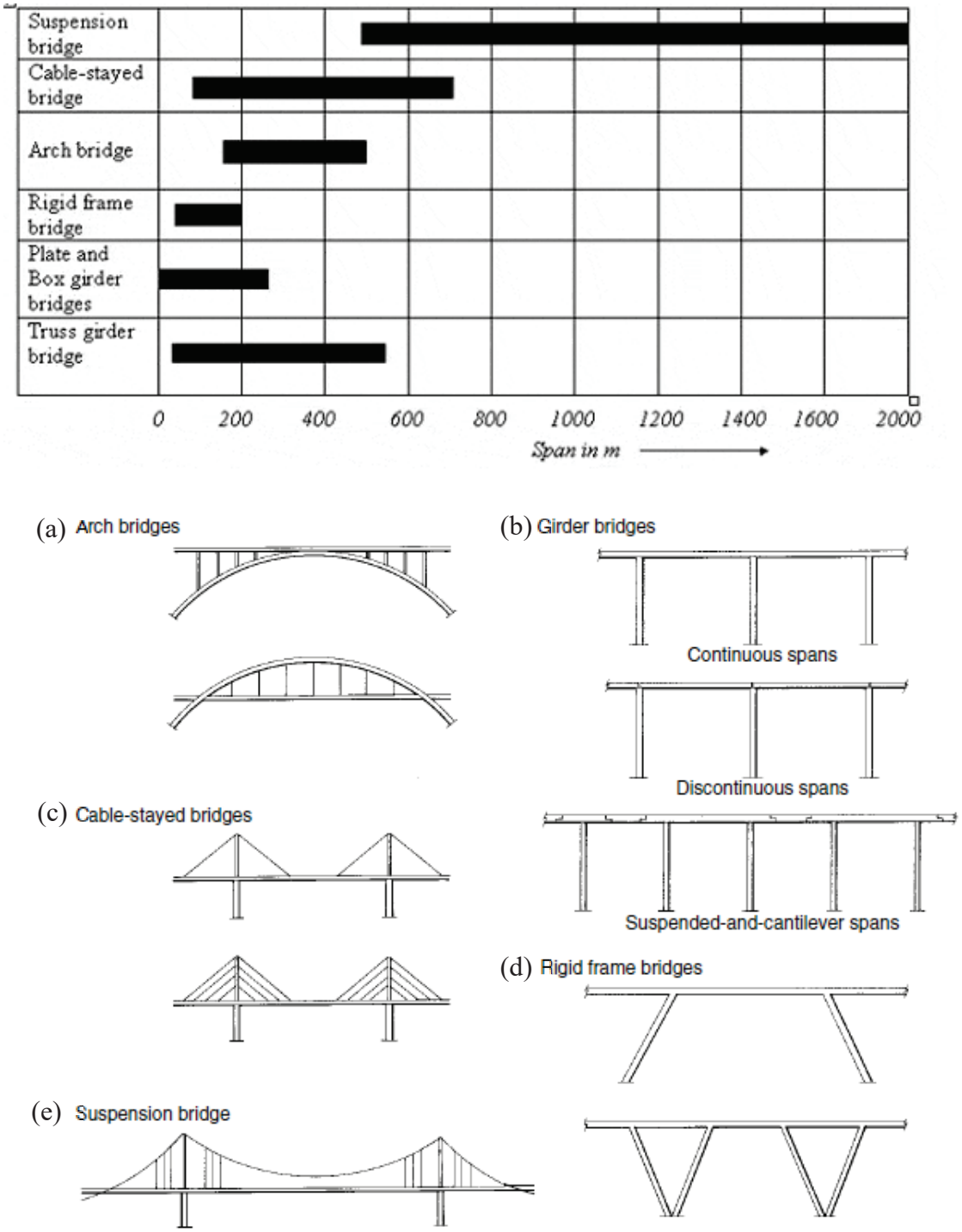

Figure 2.1. Classes of Steel Bridges (Chen et al, 2000).

2.1.2.2. Factors that lead to the choice of steel bridge

The choice of steel bridges depends on the span arrangement however, based on various factors for designing a cost-effective bridge. One of the factors include the preferences of the owner, most owners tend to push for the bridge towards the shortest span possible due to costs incurred on materials and labour. The decision is seldom

unbiased. However, due to the inclusion of public opinions the decision might shift. Alternatively, the owner might decide to build a signature bridge for popularity. Navigational clearance is another factor that affects more so the structural form of the bridge and the span. For instance, in the US, the US coast guards, and environmental committee are the sole decision makers when it comes to structures spanning across water ways. Location is another factor that directly affects the number and arrangements of spans. For example, when the structure is meant to stretch across an existing interchange. Though it is usually cost effective to move the existing structures to accommodate the new structure, however this is not the case in an urban setup. Moreover, when the structure crosses a railroad moving the railroad is rarely occasioned due to the resulting effect on the affected infrastructure. Moreover, access to site will also determine the structural form. When the bridge spans across a valley, it is desirable to avoid piers while increasing the span length making an arch or truss type more economical [13,15].

2.2. Literature Review

2.2.1. Review for Non-destructive Evaluation of Strength Degradation

The inspection of aging structures is vital. This ensures safety and further determine the residual strength of the steel structure. Therefore, incorporating NDE is relevant in highlighting any issues. In this thesis Non-Destructive Evaluation (NDE) and Non-Destructive Testing (NDT) will be used interchangeably. NDE does not alter the current condition of the structure in any way. It is meant to determine the stability and any discontinuity on the subject structure either remotely or by contact [11]. The evaluation addresses issues that might threaten the structural integrity through probing for potential flaws, characterization, and sizing of flaws. The review covers NDE inspection approaches based on limited historical data (Acoustic and vision-based methods) and surface fatigue crack(s) (magnetic, penetrant, and thermal based methods).

2.2.2. Review Method

The methodology deployed in this thesis was done according to the approach summarised from now on. Initially literature statistics was collected from SCOPUS database because of its indexing approach with the largest number of papers within the engineering-civil engineering sphere. The search was done in late 2022 with key words ‘structural health OR condition AND monitoring OR assessment OR evaluation’. The main aim was to obtain the NDE approaches based on limited historical data: acoustic emission, and vision-based methods. On the other hand, for surface fatigue crack: visual, penetrant testing and magnetic approaches. To obtain the cumulative perspective the search was exclusively based on the specific query: TITLE-ABS-KEY and employed the Boolean operators (AND, OR and *) to narrow down the search to specific NDE approaches. The searches were limited to approximately 22 years i.e., considering the commencement of the maintenance era within Japan. The cumulative search was based the query sequence: TITLE-ABS-KEY (Structural AND health OR condition AND monitoring OR assessment OR evaluation) AND PUBYEAR (2000) AND LIMIT-TO (English and Japanese) AND EXCLUDE PUB YEAR (2023) while the specific search had an additional NDE based approach appended i.e., AND acoustic, vision, penetrant testing, magnetic testing, and thermographic based approaches. Consequently, acoustic based, vision based, penetrant testing, magnetic testing and thermographic had 3101, 799,

21, 905, 3415 publications respectively presented in Figure 2.2a and b while under the generally structural health monitoring had 49304 publications based on all NDE approaches.

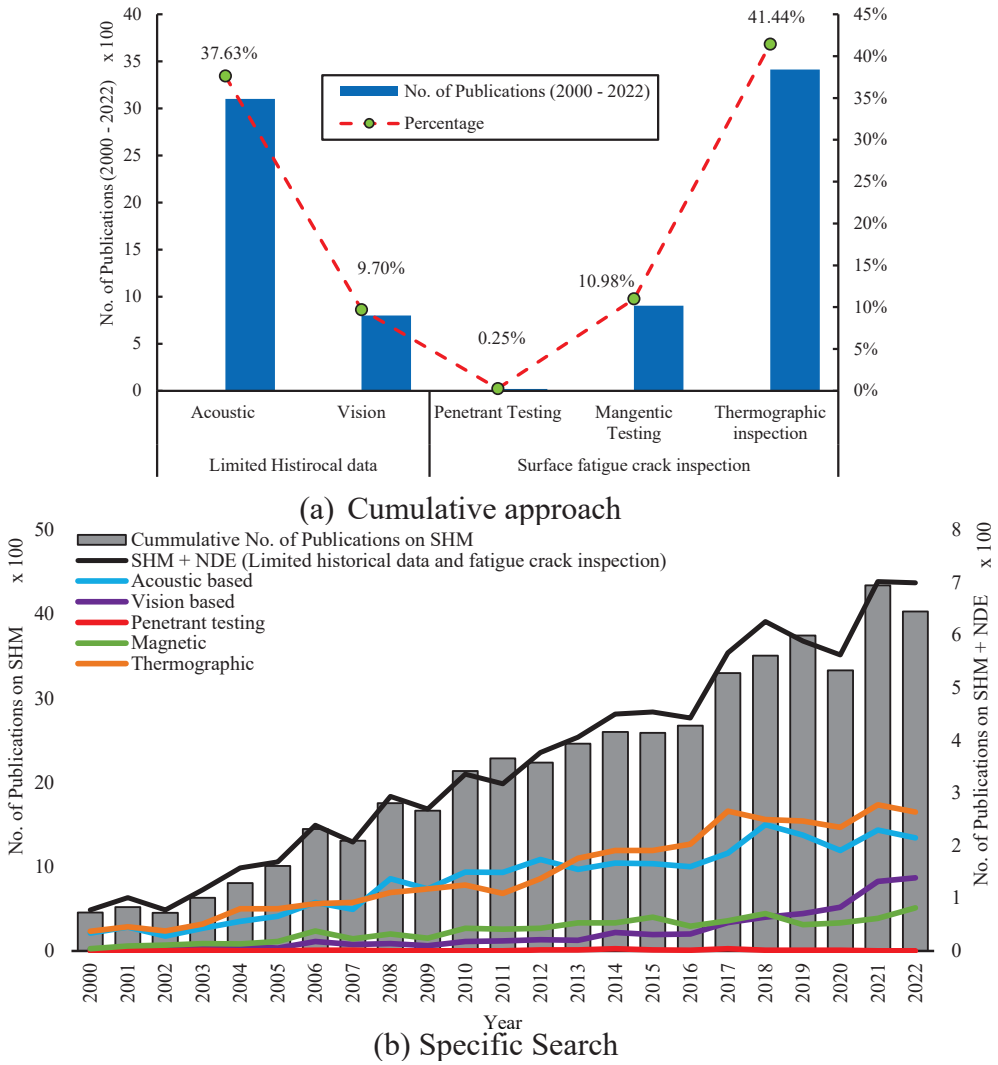

Figure 2.2. Number of publications on Structural Health Monitoring based on NDE approaches.

2.2.3. Limited Historical Data

Most of the steel bridges are old but still in operation, though to some extent degraded. For instance, Dejima Bridge Nagasaki, that was constructed in 1890 (132 years ago) shown in Figure 2.3 [16]. Rapid replacement of the same would subject the responsible authority to unwanted financial predicaments. Thus, preventive maintenance approach [17] is held in high regard over corrective maintenance approach to curb on the cost and vulnerability due to failure. Though, best practices call for the combination of the two for optimization. However, the old structures' design and specification documents are mostly not readily available or even completely absent in the authority in charge i.e., municipal offices that account for 80% of the total road assets [5]. Furthermore, as of 2021 more than 31% - approximately 230,000 structures lacked historical information in

Japan from the existing 730,000 bridge structures. The lack of such design data creates uncertainties and solo use of analytical methods pose numerous assumptions minus a validation scheme [18]. Therefore, field loading tests are encouraged [19].

Figure 2.3. Dejima Bridge – Nagasaki 1890 (Sanchez & Ney, N.d).

2.2.3.1. Dynamic and Static Loading Tests

The loading of bridges is compared to the age of bridge engineering due to it being an old age practice. Traditionally the practice was meant to demonstrate structure is safe for users. However, over time the practice was employed in the development of codes/manuals and guidelines for testing across different countries. As a result, Dynamic and Static Loading (DSL) provides a quantitative tool for assessing the bridge's serviceability, implied Saisai et al. The inspection tool offers a scientific basis for acceptance of quality coupled with Finite Element Analysis (FEA) to check for agreement [20]. Deformation monitoring through loading caters for the shortcomings of the assumptions made from mathematical models inherent in computer-based structural analysis programs [18] i.e., boundary element or finite element methods. Other than providing responses on the behaviour (performance, safety) of the bridge, they also give details of the carrying capacity of the bridge with respect to predefined codes, for instance, American Association of State Highways and Transport Officials (AASHTO) Design specifications or Japanese Bridge Design Standards [5,6]. The two main types of DSL include Proof Load testing and Diagnostic Loading for in-service structures. Additionally, ‘Acceptance tests’ combines both methods for commissioning new structures [23].

Diagnostic Loading is a loading approach exploited for evaluating and validating of models for the design and evaluation of bridges. For newly commissioned bridges it is used to illustrate that the bridge operates as designed [24,25]. On the other hand, for an existing bridge it is used for testing the accuracy and validation of models for decision making that is load rating. Proof load testing is employed to illustrate that a structure has a load bearing capacity that is safe for use and is as highlighted in the design drawings. A load within the design specification is applied on the structure. When the structure shows no signs of distress the test is considered to have fulfilled its functions. Before the onset of the 'Stop criteria,’ various problems arose during the implementation of this test related to its financial implications, safety; reliability; environmental impacts, and analytical issues. For instance, one wondered — '…when is it reasonable to terminate the test?'. 'Stop criteria' uses a simple principle of maximum threshold through monitoring the linear behaviour of the bridge [13]. Diagnostic loading is primarily used for evaluation of stiffness and assessing a structure prior to commissioning or after rehabilitation. The latter load testing is used to establish the maximum live loads a structure can bear with no observable stress, it is also at times used to evaluate structures with no plans of lack

historical data (when evaluating for safety). In summary, loading test examine the deterioration of structures [26] through deployment of sensors.

2.2.3.2. NDE Instrumentation for Dynamic and Static Loading

Acoustic Emission (AE)-based Methods

Peng et. al., during the condition assessment and load rating of a 'Engineers Bridge' pinned arch bridge spanning 55 m in Australia established that the design drawings were not available. For the bridge to be brought to service based on Military classification (MLC), the authors did onsite loading tests and used the data for modelling the existing bridge geometry. Further, the authors established the load rating based on serviceability and ultimate limit through the current Australian load standards AS 5100.2, FM 5-277 for geometric configuration and BS15-1948 & BS548-1941 for material properties, albeit many assumptions with a disclaimer [27]. In the absence of as built drawings Peng et. al. demonstrated a technique for establishing the structural capacity using the current codes for a historical bridge. Thus, non-destructive field tests using acoustic and optical methods were proposed. Acoustic methods have been recognized for detection of mechanically loaded structures [10,15]. They provide information about strains, deflection, and propagation of fatigue – deformation monitoring.

Acoustic methods are passive in nature principally relying on energy initiated from the structure under investigation. Flaws that can essentially be detected from the approach are not limited to fatigue but also their propagation and structural displacement. The process starts with the onset of forces acting on the body under investigation triggering strains that cause a deformation resulting to a local elastic or plastic deformation causing acoustic emissions. Waves travel from the sources outwards towards the sensor that effects an electrical signal for interpretation [10].

Acoustic Emission (AE) rely on the microstructural sources. For instance, fatigue that might be because of tensile, compressive or shear stresses from the loads externally or internally imposed. Khounsida et. al [29] during the study of the Load Carrying behaviour and capacity of existing bailey bridge established that during loading on a rigid state bridge the top chord experiences maximum compressive stresses than the bottom chord. On the other hand, dislocation that is the primary source of fatigue initiates from an atomic scale involves sliding of atomic planes over one another. From a large-scale source that is a crack that is a macrostructural source of AE is expected to return a high amplitude AE taking place in mixed mode. Due to cyclic loading that exceeds the local yield stress the crack tip forms new surfaces due to work hardening giving the crack enough impetus to propagate [30]. Energy released from stress fields creates new plastic wakes which is a source of AE travelling as stress waves in the material. Therefore, a sensor can record such energy and translate them into electrical signals for further interpretation. In short, due to crack nucleation and displacement AE phenomena (elastic wave generation or propagation) is observed through sensors that are not limited to accelerometers, strain gauges and displacement transducers; summarized in Equation 2-1 where $g(t)$ is the sensor response that is because of convolving the source $f(t)$ and the impulse of the system $w(t)$.

$$g(t) = f(t) * w(t) \qquad \text{Eq. 2-1}$$

Vision-based Methods

Vision-based noncontact methods measure distances and related parameters such as displacements, velocities, and vibrations. They are based on intensity, time of flight, triangulation, confocal sensing, doppler sensing [31]. The working distance of each method is a function of resolution that decreases with increase of the working distance as illustrated in Figure 2.4. Vision-based methods have a variety of uses ranging from asset management and monitoring. The approach has gained attention for structural health monitoring over the last decade, specifically from 2006 as presented in Figure 2.2 and the due to the rise of powerful computing industry and digital cameras. Their core advantage is provide remote short and long-range measurement depending on the application. Based on the approach more data is acquired as opposed to the point-based measurements such as the total station [32] for monitoring static displacement of panels.

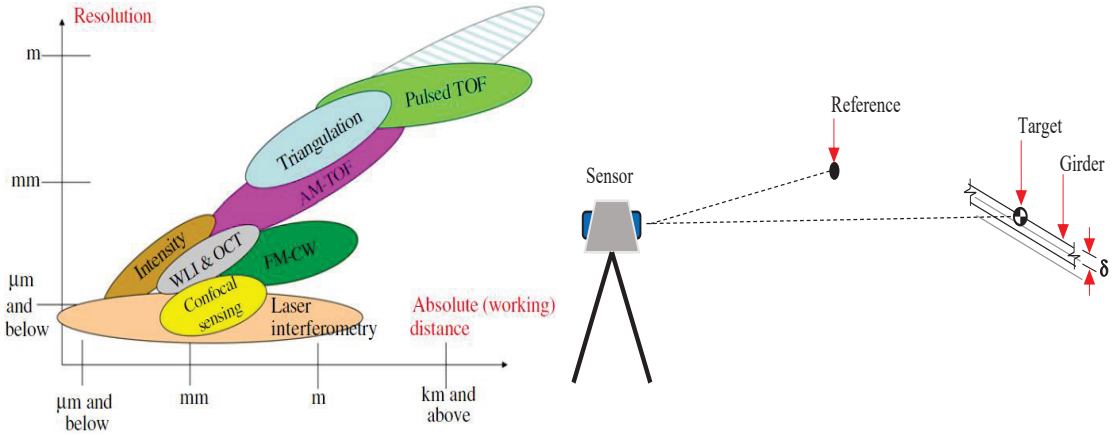

Figure 2.4. Vision-based methods

2.2.4. NDE for Surface Fatigue Crack Evaluation

Steel bridges are susceptible to fatigue at joints or members that have geometric discontinuities. The phenomena are mainly attributed to fabrication embodied by cracks that are benign during fabrication, deterioration due to aging and service exposure due to increased traffic volumes at the welded sections as illustrated in Figure 2.5a-d [33]. Previous structural details before 1960s were joined using rivets and bolts though rivets have a lower fatigue tolerance [34]; their geometry were more resistant to failure during fatigue propagation compared to welded details. Welded details introduce a severe critical stress concentration creating the initial crack situation and due to their monolithic nature, it is possible for fatigue to propagate from one element to the adjacent.

The initial stage of degradation involves the development of crack nucleation, proceeded by micro-cracks that distance and arm's length visual and NDE inspection are not sensitive. The detection of fatigue during their onset would lead to preventive mechanisms and estimation of the severity of the fatigue. Though the critical crack size is mainly considered sufficiently large enough to be visually detected, this poses a greater risk since it is difficult to assess the definite critical size [35]. For a passive component i.e., steel bridge has three stages (initiation, propagation, fracture or propagation and fracture for benign crack conceived during fabrication) during its degradation, however conventional NDE are only reliable during stage III that is perceived as the most severe stage albeit being time and labour intensive. On the other hand, emerging NDE methods

based on physical properties measurement are sensitive during stage II. Consequently, there is need evaluate the sensitivity between initiation and failure i.e., stage I to stage III.

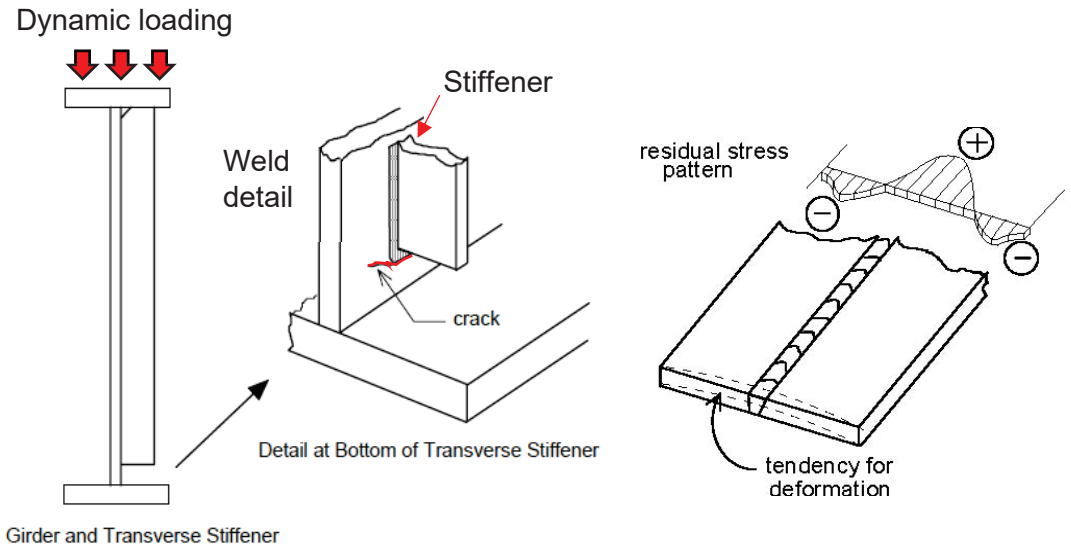

(a) Fatigue due to Dynamic Loading

(b) Fatigue due to tensile residual stress

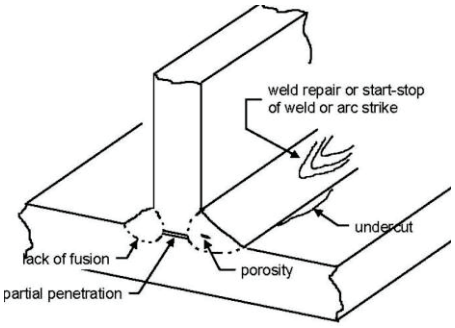

(c) Fatigue initiation point by inclusion

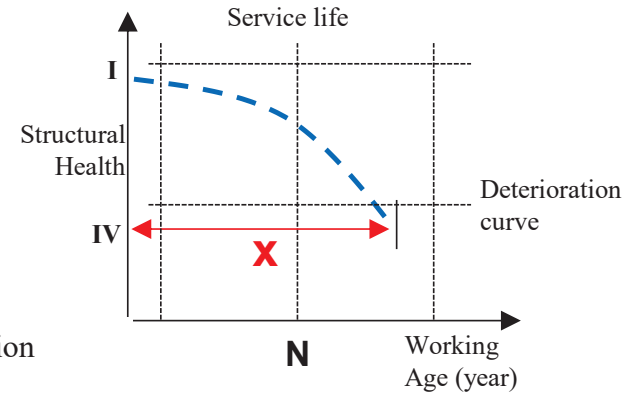

(d) Fatigue due to aging

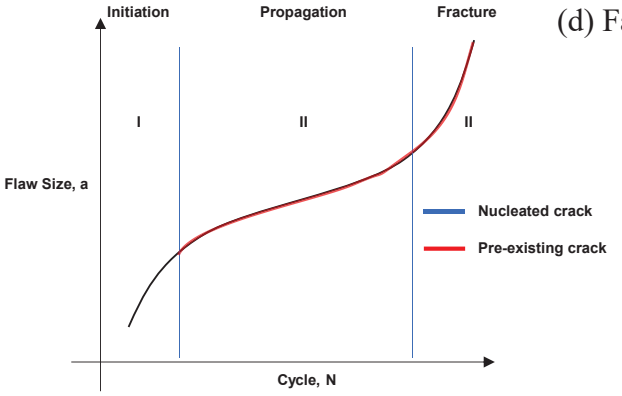

(e) Fatigue initiation and propagation

Figure 2.5. Causes of fatigue on welded sections (Mertz et al., 2012)

Steel structures if not managed their safety margin will be reduced putting at risk the owner and the users. On the other hand, replacement of structures is costly more so to local authorities who have jurisdiction over the asset. Effective management through early detection of precursors qualitatively and quantitatively is prudent. During the 1960s

Japan massively constructed the Orthotropic steel decks (OSD) that were assisted by the cable stayed and suspension bridges. Due to the massive weld details in OSD fatigue has been observed especially on structures beyond 40 years [4,45]. The phenomena in addition to limitations on conventional NDEs have illustrated the significance of an effective NDE method is essential for efficient management of steel structures and mainly detection of fatigue at an early stage. Common NDE approaches are usually classified either as surface or subsurface methods. This thesis will mainly focus on surface fatigue NDE approaches, however it should be noted that some NDE approaches can detect both surface and subsurface flaws. Common approaches for steel bridge inspection are not limited to:

2.2.4.1. Non-Destructive Evaluation for Surface fatigue crack(s)

Visual Inspection

This approach is widely used and perhaps the oldest approach for bridge inspection. The method is primarily limited to only surface flaws that are adequately pronounced to be noticed [10,11]. For one to notice such, proximity to the affected areas is key i.e., arm's length distance. Though, conventionally this is not the case. Moreover, the inspector maybe complacent or focused on other issues associated with the bridge as a result overlook most of the details. Additionally, when under poor lighting condition even the most prominent of surface flaws can easily go unnoticed [11]. Consequently, bridge inspectors must possess attributes, physical and psychological attributes that result to good judgement for instance having a good score on the Jaeger Test. The method at other times involves use of simple tools such as digital cameras and is mainly suitable for general inspection or routine inspection of the super structure. This approach predominantly qualitative devoid of other accessories. Consequently, there are other NDE methods that have enhanced evaluation properties such as Penetrant, magnetic, and thermographic testing.

Penetrant Testing (PT)

This is perhaps the low cost NDE method for detecting minute cracks or discontinuities. Its approach was from the railway industry first known as the oil and white method for inspecting cast railroad wheels [37]. The technique is based on the ability of the non-viscous liquid to penetrate cracks by capillary action summarised in Equation 2-2, and some may stay when the rest is removed. A developer is employed to cause surface tension making the affected areas pronounced. The method's principle uses a coloured non-viscous or luminous pigment that is applied onto the suspected area. The excesses are wiped off to an extent that the surface is clearly visible. A developer is then applied that deposits a thin white film over the area effecting surface tension that extract the remnants of the penetrant providing a coloured contrast an indicator of the presence of cracks. The process usually takes a few minutes in addition to preparation of the surface. The interpretation of the area is straightforward whereas linear intermittent indications reveal presence of cracks and determining its dimensions as relayed in Figure 2.6a. The method is, however, time consuming if more than one section needs to be evaluated as well as requires the preparation of the surface prior to applying the penetrant [11,38]. Additionally, it is not an effective method for irregular, porous surfaces and may contaminate the affected surface when the thin liquid sips behind.

$$h = \frac{2T\cos\theta}{\rho g r} \quad \text{Eq. 2-2}$$

Whereas h penetrant elevation (μm), T surface tension, θ contact angle, ρ density, g Gravity, and r Radius.

Magnetic Testing (MT)

Magnetic particle testing is an inspection method employed mainly on ferromagnetic material. A magnetic field is created on a steel bridge component between the poles or legs of a yoke. This results into lines of magnetic flux which when intersects with a crack will create a localized area of flux leakage summarised in Equation 2-3. The flaw will not create a uniform field as the surrounding areas causing the magnetic field to spread out i.e., magnetic flux leakage. When the magnetic flux is oriented normal to the flaw direction the fatigue is more pronounced considered to be the most reliable condition for the generation of an indication. Proper alignment of the yoke is hence advisable to be oriented at 45^0. Thus, when employing magnetic particles, they accumulate on the flawed area in form of clusters around the region as illustrated in Figure 2.6b. the method is however, limited when it comes to areas with thick paint or irregular surface finishes and roughness.

$$\begin{cases} \phi_l = \phi - \phi_u \\ \lambda = \dfrac{\phi}{\phi_u} \end{cases} \quad \text{Eq. 2-3}$$

Whereas ϕ_u useful flux, ϕ total flux, ϕ_l Flux leakage (Wb), λ leakage coefficient.

Infrared Thermographic Testing (ITT)

The evaluation of a structure based on fracture mechanics is considered essential for mainly deteriorating steel structures. Conventional, approaches for surface crack detection i.e., visual inspection, magnetic particle testing and liquid penetrant cannot be used to directly evaluate the remaining strength of the structure or determine the rate of deterioration. As a result, fatigue evaluation based on fracture mechanics when monitoring fatigue with respect to its various stages from initiation to fracture [11,39]. ITT is an imaging-based method that exploits IR radiation remotely. There are various classes of classifying ITT ranging from the detector type as presented in Figure 2.6c, source of excitation energy and approach. Active ITT requires additional energy stimulation based on mechanical waves, optical radiation or eddy current. on the other hand, passive ITT one would monitor the temperature distribution on an object and decide based on the self-emitted temperature or self-excitation. Unlike other approaches the method can work on both ferrous and non-ferrous material though its efficiency highly depends on the thermal properties of the material under investigation [4].

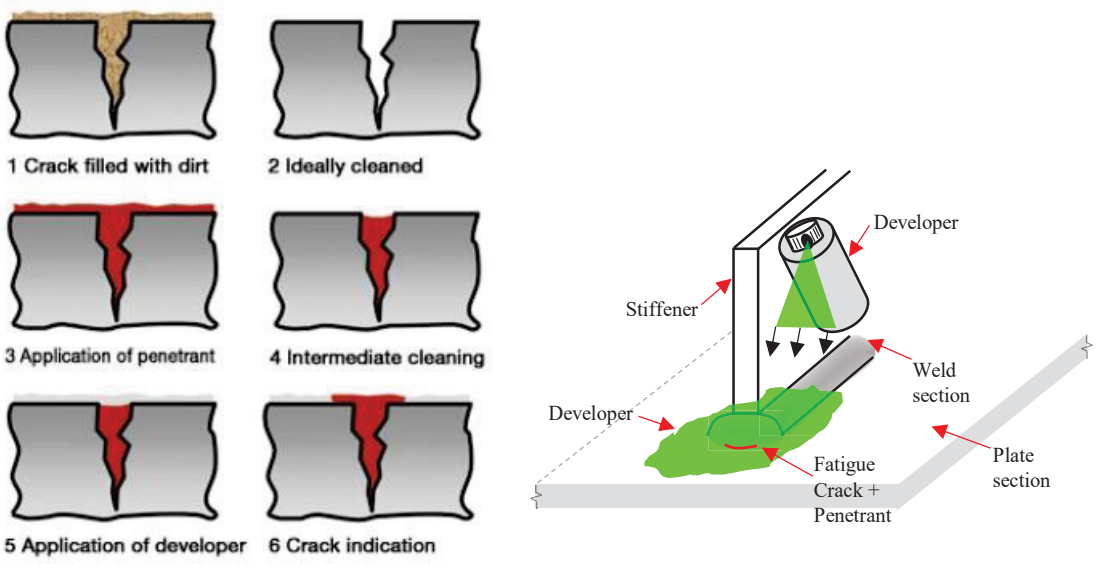

(a) PT preparation method and pronounced surface after application.

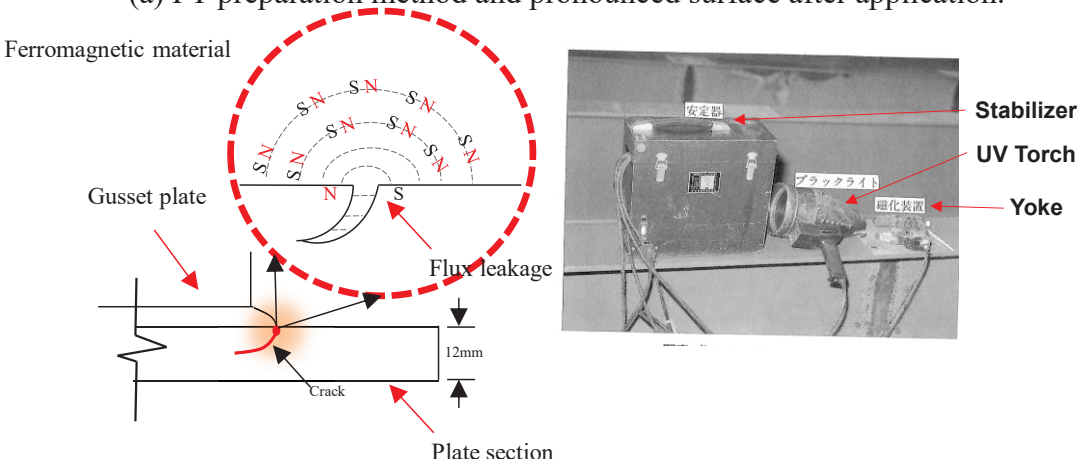

(b) MT preparation approach and leakage flux on welded section

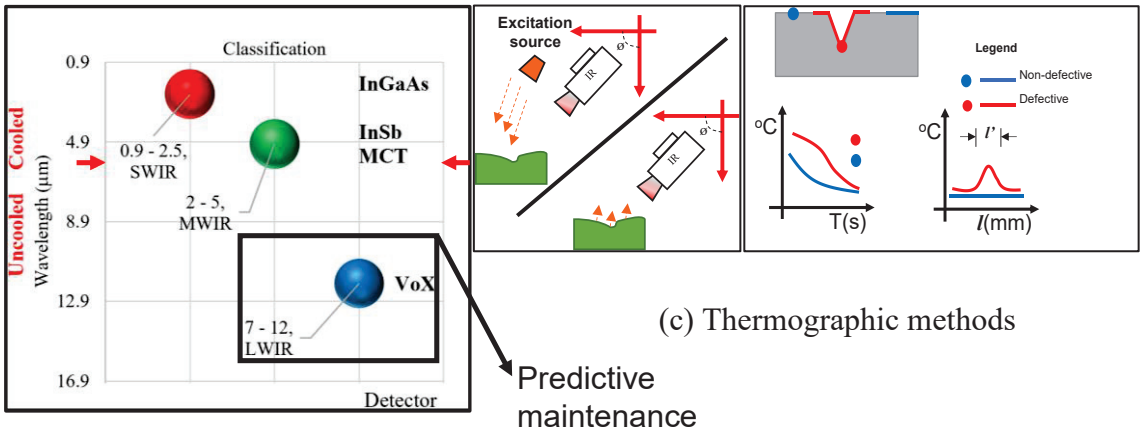

(c) Thermographic methods

Figure 2.6. NDE Approaches (Japan Road Association, 1997)

2.2.4.2. Destructive Evaluation for Fatigue

Beach-mark Testing

Conventionally internal cracks cannot be observed directly after failure hence destructive evaluation takes precedence for sections under investigation prior to putting them in service i.e., a member is as strong as its weakest link. The main purpose of destructive testing is to ensure that a reliable component will be used. The exploited destructive testing is not limited to corrosion testing, hardness testing, tensile testing torsion testing stress testing, and residual stress measurement. Therefore, in ductile materials there is usually a conspicuous appearance of a brittle fracture appearance indicating crack fronts at each cycle stage. These are known as fatigue stratification, widely known as beach-marks presented in Figure 2.11a. The section that experienced the final fracture usually have a dimpled appearance. There are characteristic features of a fracture surface impacting from irregular loading during fatigue propagation. Therefore, for experimental purposes, controlled beach-marks can be obtained through repeated two step fatigue tests using Yamada fatigue testing machine [40] illustrated in the waveform in Figure 2.11b [41]. Predefined but irregular stresses are introduced at intervals creating marks that that relay the nature of fatigue propagation [42].

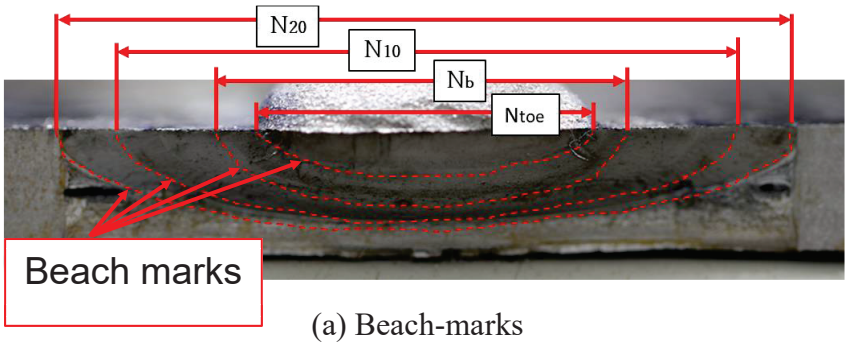

(a) Beach-marks

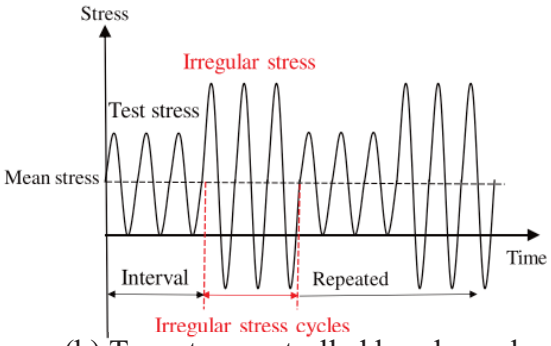

(b) Two step-controlled beach-marks

Figure 2.7. Beach-mark Testing

2.2.5. Best Practices

In this section some best practices of instrumentation and monitoring with an intent to generate the initial data for historical use and inspection for surface fatigue cracks are presented based on various NDE approaches:

2.2.5.1. Acoustic-based Methods

Kolkata India

The shortcomings resulting from assumptions made from computer based analytical methods can be supplemented by onsite loading tests. Parivallal et. al., [18] determined an approach of instrumenting and evaluating the response measurement of a 24.38 m span truss bridge during loading employing 14 displacement transducers and 50 strain gauges as illustrated in Figure 2.8a-c. The method used the Indian standard code, Indian Road Congress (IRC), and guide to establish the maximum the permitted load. The stiffness of the bridge was established through the mean global deflection of the chords. Local responses such as fatigue were evaluated using strains. The response spells the need for further evaluation [18]. The study further established an approach of determining the suitable location of evaluating stresses along the panels by determining the maximum bending moments through analytical methods using Finite Element Analysis [18]. To establish the bearing capacity of the bridge, stagewise loading was observed by placing the loads at symmetry, eccentrically and loading diagnostically within the linear elastic region of the bridge. The response was further checked for agreement with an analytical model. The deflection for higher loads were established through commutation from the influence profiles. The research established that the bridge belonged to the IRC class 24R but can safely be used up to IRC class 40R. Therefore, a framework for instrumenting the steel structure; diagnostic loading plan; validation of onsite data to establish the behaviour and safety of the bridge were determined.

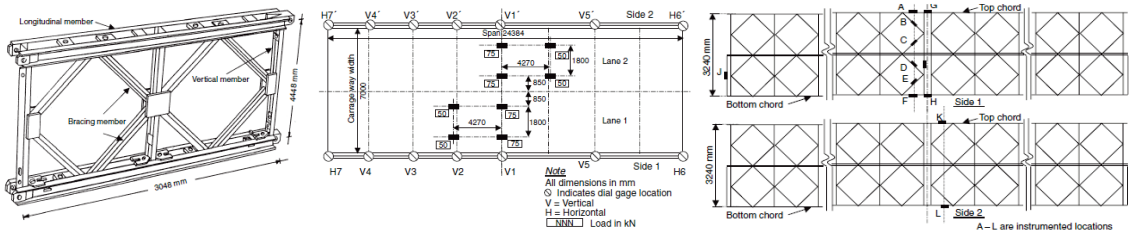

(a) (a) Typical (b) Dial Gauge (c) Strain Gauge

Figure 2.8. Instrumentation of Bailey Bridge (Parivallal et al, 2005)

Vientiane Laos

Loas consists of 516 Bailey bridges that constitute the second most used road asset (15216 m long) after concrete type bridge. To prevent any dangerous situation Khounsida et al., [7] determined the dynamic and static behaviour of a deteriorated bailey bridge. The bridge structure was located on National Road Number 10, Vientiane Province, double span of Double Single Reinforced (DSR) type. It was suspected to be built as a Triple Single Type (TS) in 1995 and later collapsed in 2015 and rebuilt to DSR type [7]. This perhaps illuminating the versatility [43] of the bridge under different configurations [44]. The bridge structure was modelled based on the actual geometries on-site and the behaviour checked for agreement with the measurement results through full scale loading

tests of a maximum of 15.85 Metric-tons. Instrumentation of the bridge was meant to achieve a global deflection and vibration located at predetermined sections. Static response was recorded through determining the deflection with a displacement 4 No. displacement transducers. On the other hand, dynamic responses were recorded using 2 No. accelerometers. An optical method using a total station was employed to supplement a transducer for deflection of the chord [7].

Deterioration on the structure were introduced through reducing the thickness of panel and removing the sway bracing members (50% reduction) to project corrosion. Alternatively, 100% removal of some cross-section members for instance the bracing members or panel that are critical in preventing collapse through allowing the ultimate limit state to be achieved [19,20] to present a missing part. Further, the wooden deck sections would also be assumed to indicate a defective deck section. The superstructure was assumed to be of the same material 250,171 MPa (E). The static results were checked for agreement with field data that led to investigation of the dynamic response. It was established that the superstructure vibrates when damaged i.e., removal of some members or reduction of thickness of members. Moreover, the stiffness of the structure is affected by the absence of critical members [29]. The analytical results may differ from the on-site measurement in case overlooked defects and the stressed were examined to be higher on compression members than tension members [7] i.e., bottom, and top chords respectively.

2.2.5.3. Vision-based Approach

Aspire Nottingham

Conventional geodetic instruments such as the total stations have been widely employed in deformation monitoring of structures. Khounsida et al, when determining the load bearing capacity [7] of a bailey bridge in Laos used examined the deflection values with displacement transducers that give fairly good results. However, the method provides only point data compared with the reference point limiting the evaluation of multiple elements at once – discrete point analysis [32]. The former tends to provide limited information concerning deformation status of the structure. Conversely, Jatmiko et al, when monitoring Aspire structure in Nottingham presented a helical approach of monitoring the structure by restricting horizontal 360^{o} motion and allowing for only 100^{o} vertical motion [45] with a pulse repetition rate of 1.2 MHz. The study assessed the capability of Terrestrial Lidar Scanner in monitoring the dynamic movement of the structure on wind loads. The approach solved the scan time delay inherent in image processing methods [46]. Moreover, TLS allows for acquisition of point cloud data allowing for effective examination. The method takes advantage of the shape observed and reconstructs them from regular objects mathematically modelled.

Bridge 631 – Western Australia

To establish the sensitivity of TLS under different operational modes Lichti et al, deformation of a wooden bridge under static loading was examined. Before decommissioning of the bridge, it was subjected to static load testing on the two wooden spans along 6 m stringers. The purpose was meant to gain insight into their load bearing properties. The structure was instrumented with LVDTs, digital photogrammetry and TLS to measure its stiffness. Loads were applied up to a maximum of 65.75 T at various locations especially at the midspan thought to be a section where there are maximum bending moments. Consequently, the research established that calibration of TLS cannot

be done using the default baselines employed by geodetic methods. A comparison of the TLS and photogrammetry was established that saw, measurements made from the bottom cross-section being biased with an RMS error of ± 9.1 mm while ± 4.9 at the top cross-section [47]. The dominant error source was shape distortion. However, in 2006 the use of reconstruction algorithms improved the accuracy using image processing techniques i.e., target geometry and number of pixel moved for dynamic displacement [39,43].

2.2.5.4. Thermographic-based methods

Longitudinal Coupled prefabricated slab tracks (LCPSTs) are widely deployed in highspeed railroads accounting for at least 35% in China's infrastructure. Due to their in-service life their structural integrity deteriorates and defects such as cracks manifest. To detect the developing cracks in a timely and effective manner requires an approach devoid of manual inspection, characterised by over-reliance on personal experience. Therefore, Zai-Wei et al, adopted thermographic methods using temperature field isotherm. The method determined the difference in amplitudes to determine the presence of cracks and using the isotherm diagram to determine the dimensions of the crack. The method also indicated that crack width affects the probing and detection of cracks [49]. On the other hand, Sakagami et al, used temperature gap approach to evaluate the deterioration of fatigue on OSD welded sections. The research relayed how IRT can be employed in evaluating for integrity based on fracture mechanics. Further, the study assessed the based on the stress distribution in the OSD including the effects of wheel loading conditions [4].

2.2.6. Adaptation for Temporary to Semi-permanent/Permanent Steel Bridges

In response to the damage because of natural phenomena such as earthquakes and floods in the recent years within Japan, there is need to develop a restoration/adaptation framework of temporary/semi-permanent steel bridges. Numerous approaches have been advanced [50] bringing to focus steel bailey bridges. However, within the nation the developments of adaptation frameworks are limited. Temporary bridges are characterised by lack of maintenance and missing historical records i.e., as built drawings and maintenance reports. Therefore, the need to come up with an appropriate maintenance-and adaptation approach to avoid their rapid deterioration and eventual collapse or eminent failure as illustrated in Figure 2.9 is essential [51] hence increase their service life.

Figure 2.9. Bailey bridge collapse due to deterioration (Chowdhury, N.d.)

Traditionally, bridge condition assessment was based on conservative computations of the load bearing capacity. This approach relies on the as-built drawings and visual inspection reports. However, the computations are usually understated due to negligence because it relies solely on personal experience [52] and the nature of visual inspection is at times subjective. However, King et al., [19] suggests that in-situ load testing gives the optimum structural response and validation component for modelling of the numerical model to be employed as an initial database component [53]. Firstly, the structure critical information should be determined regarding structural condition. However, critical bridge information tends to be specific to a particular bridge. As a result, National bridge element (NBE) — remains consistent across the country, and bridge management element (BME) — is local based such as an inspection manual within a municipality; should be endorsed whereas the former is the general perspective meant to determine the general condition while latter is specific hence agency oriented or local in nature [54]. Additionally, information regarding bridge inspection (historical data) is checked for availability to evaluate if the structure has a maintenance record. The main aim is to summarize the information that will be employed to conduct a structural health conditioning hence referred to as bridge characterization i.e., database creation. Secondly, field surveys should be done to complement the missing information and corroborate the available information. Therefore, a numerical model is developed from onsite measurements (geometrics). The condition of the structure can be accounted for through loading tests using either Proof loading or Diagnostic loading under dynamic or static conditions. The bridge can then be rated after validation of the model using onsite data [19]. This forms the basis of the framework [55] that can be used for future condition assessment of the structure and planning.

2.3. Conclusions

This chapter presents the literature review with the intent to outline NDE approaches for evaluating the structural health of existing steel bridges and the best practices associated with the same hence draw a hypothesis for evaluating structures with limited historical data and surface fatigue crack evaluation. The conclusions are as outlined:

1. Research based on Thermographic methods, acoustic and vision-based methods are the most popular indicating their viability for deployment in evaluation for structural health.
2. The NDE approaches are integrated with traditional and conventional approaches to evaluate for accuracy and redundancy i.e., deploying thermal non-destructive evaluation hand in hand with magnetic testing. On the other hand, acoustic methods are integrated with vision-based methods to assess structural stiffness.
3. Due to the limitation of historical data, adaptation of structure is deemed viable to establish their management approach through experimentally proposing an adaptation framework on a case-based approach through characterization, field survey, loading test and bridge rating.

Chapter 3

Non-Destructive Evaluation of the structural Health Condition of Temporary and Existing Steel bridges as Permanent Structures.

3.0. Overview

The present study assessed the Bailey Bridge's condition and investigated its adaptation as a permanent structure, targeting the Acrow Bailey Bridge in Japan. Field diagnostic loading experiments were performed under various loading conditions, such as dynamic and static loading tests. The onsite data were obtained using a transducer, strain gauge, target measurements using the image processing approach, and accelerometer. From the field measurements, the deflection and stresses of the bridge were found to operate within the linear elastic region. The bridge was then accurately modeled based on the in situ geometric configuration of the bridge, and Finite Element Analysis was performed. The model's accuracy was validated with the onsite data and previous studies under the linear elastic domain. The model then was deployed to check for resistance of critical members. A nonlinear analysis based on the linear and nonlinear buckling method was performed to determine the subject bridge's Serviceability Limit State and Ultimate Limit State. The results showed that the first out-of-plane eigenvalue buckling analysis could monolithically assess bridge members. Further, the study established Finite Element models resolves for limited historical data through in situ modeling measurements — loading tests. Therefore, the findings obtained in this study highlight the bridge's Structural Health Condition, bearing capacity, and propose a framework for adaptation as a permanent or semi-permanent structure.

3.1. Introduction

3.1.1. Background

A Bailey Bridge is a rigid frame type, prefabricated truss bridge whose symmetrically bending moments vary from maximum to zero from the centre span to the end posts. This aspect is fundamental during their design because the end bays are not entirely used, exposing the centre bays to maximum stress [18]. Bailey Bridges were initially meant for military use. However, their benefits have been diversified from temporary to semi-permanent or permanent due to their ease of transportation, low cost, flexible structural form, onsite fabrication, and versatility in accommodating various loading requirements [29]. The panel elements are interchangeable, making them easy to assemble by pinning the components under different configurations. It takes at least 40 min for a simple combination of double truss employing the cantilever launching method short of falsework [56]. Structural degradation due to loss of parts is expected; primarily, loose pins that readjust during the dynamic movement of traffic have been reported. Additionally, they are subject to maintenance issues and lack of historical data [27], such as the bearing capacity. Therefore, it is advisable to assess their structural integrity.

To verify the load-bearing performance of an actual Bailey Bridge, Yi et al. [27] King et al. [19] and Khounsida et al. [2,6] are hereafter worth mentioning. The authors [2,4,6] exploited the Diagnostic load test using Dynamic and Static Loading (DSL) to certify the bearing capacity for both in-service [2,6] and out-of-service bridges [27]. Diagnostic load testing is meant to assess the structural response of a bridge, and update or calibrate an analytical model for decision-making. The calibrated model is then deployed to evaluate the load rating factors, particularly to determine load rating and safety. Conventionally, the loads applied are below the bridge's capacity - similar to serviceability limit state conditions; hence larger loads are extrapolated. Consequently, Yi et al. established that the design drawing was unavailable during the load rating of the 'Engineers Bridge'

pinned arch bridge. Three targets were selected, ¼ span, mid-span, and ¾ span, to establish deflection using a total station with an accuracy of 0.2 mm. The author modelled the bridge using existing onsite geometry for the bridge to be analytically examined and compared the deflection results with field measurements. The author went further and established the load rating based on the serviceability and ultimate limit of the bridge using the current codes, demonstrating an approach for establishing the bearing capacity [27]. On the other hand, King et al. found that to evaluate the structural response of a Bailey-type Bridge, actual loading conditions should be tested, and a numerical model was employed to examine the nonlinear response. Under laboratory testing the author used a 130-t Universal dynamic Servo-hydraulic Tester to simulate various loading conditions and Linear Variable Differential Transformer (LVDT) displacement sensor to monitor deflections [19]. Further, Khounsida et al. determined the Bailey Bridge response through onsite experimentations and structural analysis of a bridge in Laos [7]. The author acquired on-site data statically by displacement transducers and total station, and dynamically using an accelerometer positioned at optimum locations along the girders for maximum deflection. In each of these studies, the evaluation of load-bearing performance by linear or nonlinear finite element analysis was based on actual and on-site member measurements. Therefore, it is thought that appropriate maintenance and management of a permanent bridge can be performed by clarifying the bearing capacity and ensuring the conversion from a temporary bridge to a permanent bridge.

3.2. Experimental Objective

The present study aims to assess a Bailey Bridge's condition and investigate its adaptation as a semi-permanent or permanent structure through proposing a conversion framework. The Sukumo bridge was targeted, the only Bailey Bridge type in Uchiko Town, Shikoku Island, Japan. First, diagnostic loading field experiments were performed through DSL tests to examine the static and dynamic behavior of the Sukumo bridge. The structural responses were determined both statically and dynamically. The displacement transducer and image processing approach assessed the deflection on static loading conditions, while the Micro-electromechanical Systems (MEMs) accelerometer for dynamic loading deflection [46,57]. Frictional strain gauges [58,59] accounted for the strains. Then, the bridge's Finite Element Analysis (FEA) model was developed, and its validation was confirmed compared to the field measurement results and previous experiment. Further, nonlinear analysis was performed using the validated model to examine the load bearing capacity of the Sukumo Bailey Bridge. Based on these, the possibility of adaptation of the Sukumo bridge as a permanent structure was evaluated similarly its framework.

3.3. Bailey bridge structural characteristics

Numerous bridges have been made from the typical bailey bridge panel using assorted designs and material strengths:

3.3.1. First Generation

The Bailey Bridge was designed by Sir Donald Bailey and patented in 1943 [27,56]. It was the basis for the current modular bridge. The bridge was a transportable,

prefabricated truss bridge realized by developing new construction methods and panel connection systems from the Callender-Hamilton Bridge [44,50]. Each member of the Bailey Bridge is standardized, as shown in Figure 3.1a. Depending on the span length and the number of lanes, the strength of the girders can be increased by stacking multiple panels of typical dimensions 3050 mm × 1550 mm or connecting them vertically. In addition, it uses hollow high-grade, lightweight steel material that can be transported manually and does not require special tools launching and fabricating. The first-generation Bailey Bridges are classified into M1, M2, and M3. Bailey M1 is the initial type, while the predecessor Bailey M2 was designed by widening the roadway/width by 20 mm from the initial 4000 mm, and Bailey M3 was an improvement of Bailey M2 [60] similarly increasing its roadway by 180 mm like its predecessor.

3.3.2. Second Generation

After the Bailey Bridge patent expired in 1970, Thos Storey Engineers Ltd. and Mabey Johnson Ltd. introduced the Acrow 1, Acrow 500, and Mabey Super Bailey as well as, the Compact 100 in that order. The Acrow 1 Bailey Bridge had a diamond panel configuration with the transom moving in the diamond panel. It was conspicuous due to its method of eliminating stress related to pinhole sag and global deflection due to the diamond configuration at the fulcrum section. The design could accommodate two transoms per panel. On the other hand, the Acrow 500, introduced in 1987, used a single universal transom at each bay, retaining its panel dimension illustrated in Figure 3.1c. The Mabey Super Bailey was introduced in 1967 with improved detail and strength than the typical Bailey but with similar panel dimensions [44]. The lower chords panel used bolts and facing plates on the top chord for strength. Its predecessor, the Mabey Compact 100 [13,14], used high-grade steel and channel sections as bracing frames with one transom per panel. The second generation of the Bailey Bridge is lighter than the original Bailey Bridge and uses the same end post configuration with varying dimension as the M2–type typical Bailey Bridge demonstrated in Figure 3.1d–measurements from site.

3.3.3. Third Generation

The Mabey Compact 200 and Acrow 700 came with increased panel depth, approximately 50% higher panel height, and 20% more potent in shear than the original Bailey Bridge demonstrated in Figure 3.1b-c. The depth improved its stability and potential to accommodate a wider roadway of 7.3 m. Mabey Compact 200 was used during the construction of the Baker bridge in 2009 in Cambria, Britain. The Acrow 500 was replaced with the Acrow 700, later adopted as Acrow 700XS [44]. The Acrow 700XS were assembled for recovery efforts at ground zero of the World Trade Center, during the terrorist attack, in record time. The structure was erected on prefabricated piers, moving a record 1.8 million tons of debris. Additionally, it was also operational during the rebuilding process. On the other hand, New Jersey Turnpike Authority employed the 700 [44] series to create a diversion during the upgrade of the existing bridge in a record 15 min.

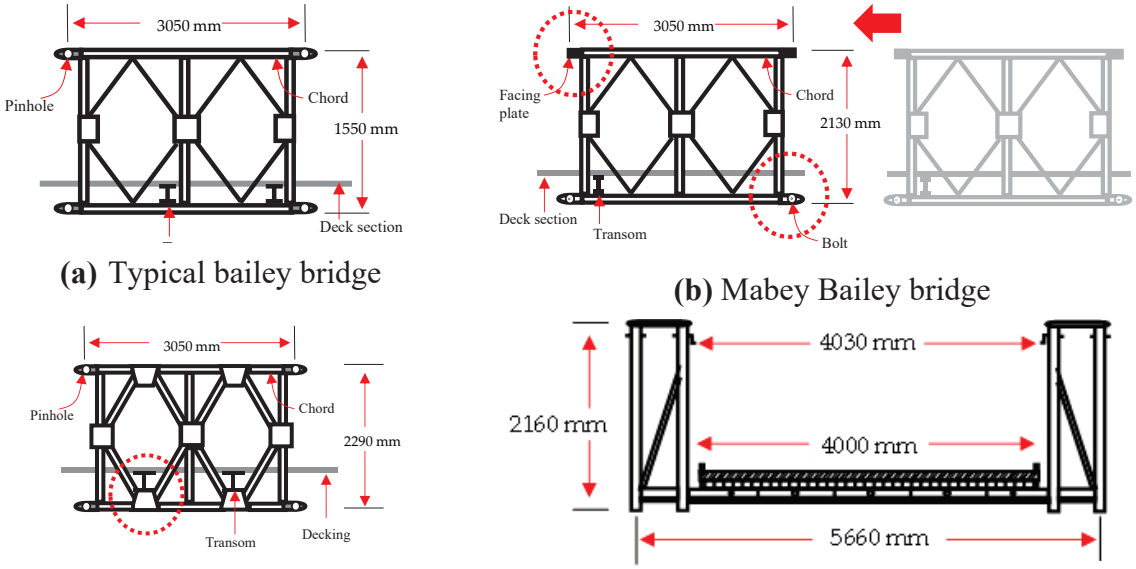

(a) Typical bailey bridge

(b) Mabey Bailey bridge

(c) Acrow Type Bailey

(d) Typical M2 end post

Figure 3.1. Typical Bailey Bridge Structural Characteristics

3.4. Field experiment

3.4.1. Target bailey bridge

Figure 3.2 shows the target bailey bridge referred to as the Sukumo bailey bridge. The bridge is in Uchiko Town, Kita District, Ehime Prefecture, along the junction of Route 56 highway. The bridge was built in 1997 as a temporary structure to serve as an access for constructing one of the Matsuyama Expressway (E56) piers across the Nakayama River. Additionally, after the completion of the main line it was meant to serve as a town road courtesy of Japan Highway Public Corporation. The bridge spans 31.81 m, having a carriage width of 4.0 m, as shown in Figures 3.2a, 3.2b, and 3.2c. The bridge has an alleged loading capacity of 25 T, sourced from interviews from Uchiko Town municipal offices. It is a third-generation bailey bridge Acrow type Double Single Reinforced (DSR), with a panel of 3.976 and 2.134 m, length, and height, respectively.

(a) Sukumo bridge

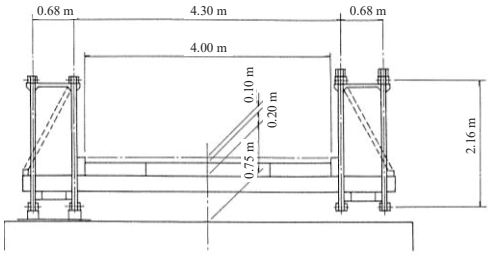

(b) The front view – end shears/posts

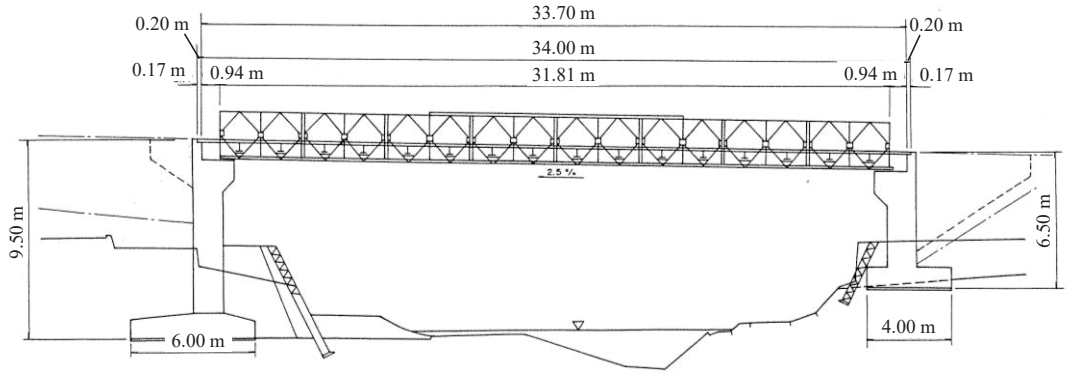

(c) The side view – panel sections

Figure 3.2. Sukumo bridge - Target Bailey Bridge

3.4.2. Load test

Load tests were performed statically and dynamically to examine the static and dynamic behavior of the Sukumo Bridge. Before the loading tests, three types of loading cases were selected, not to exceed the Sukumo bridge's presumed loading capacity (i.e., 25 Tons). It was assumed that the loads chosen were within the elastic region.

Equation (3-1) summarizes the approach for load selection. A bridge (Bailey) has an elasticity range that departs from its linear elastic region when the applied loads exceed its bearing capacity. This principle is critical in the structure's bearing capacity that dictates its capacity–Serviceability Limit State (SLS). Hence, it refrains the structure from plastically deforming (aid in predicting various effects of load on a structure) when the loads are beyond the design capacity–Ultimate Limit State (ULS). The decking joints are critical, considering they receive the full effect of dynamic hammering of loads; it is prudent not to exceed the design tolerance [5,6]. Therefore, the choice of loads was dictated by the principle of superposition summarized in Equation (3-1), where δi-n denoted displacement (mm), Fi-n denoted Load (Tons), and m denoted slope.

$$\begin{cases} (\delta i, \mathrm{F}i), & \mathrm{F}i = \mathrm{m}\delta i + \mathrm{C}i \\ (\delta ii, \mathrm{F}ii), & \mathrm{F}ii = \mathrm{m}\delta ii + \mathrm{C}ii \\ (\mathrm{F}i + \mathrm{F}ii) = m(\delta i + \delta ii) + (Ci + Cii) & \end{cases} \qquad \text{Eq. 3-1}$$

Table 3.1 shows the three types of loading cases. Loading cases/condition included Loading case 1 was a Car whose weight was 1.57 Tons, 2 was a Truck whose weight was 12.24 Tons, and 3 was a Crane whose weight was 19.66 Tons, excluding the average weight of the driver weighing approximately 55 kg. These weights were loaded statically and dynamically onto the bridge. After this, the loading conditions are explained in detail.

Table 3.1. Three Types of Loading Cases

Load	Model	Weight (Tons)	Loading case/condition
Car	DBA-ZRR80G	1.57	1
Truck	KLL-CW55E	12.24	2
Crane	Tadano YDS-T014	19.66	3
The average weight of the driver: 55 Kg			

3.4.2.1. Static Loading Condition

Figure 3.3 shows the static loading conditions. Due to the constrained width of the structure, 4.0 m; symmetrical loading was limited. Hence, the Load's Center of Gravity (COG) was established from the load axles for optimum positioning of the load cases, as shown in Figure 3.3. The bridge deck was demarcated widthwise 0.74, 0.93, and 0.91 m from the center of the lane, as illustrated in Figure 3.3. The dimensions were based on the loading cases. Lengthwise, the structure was divided into 6 sections with 5 targets at 5.0 – 5.905 m along the bridge t_1 to t_5 with the largest interval at the two farthest sections of the span. Loading case 1 was set at the mid-span of the Sukumo Bridge (t_3), while loading cases 2 and 3 were set at targets t_1 to t_5, ensuring the axles COG coincides with the target axis in Figure 3.3a-c.

3.4.2.2. Dynamic Loading Condition

The dynamic load test under ambient conditions was conducted such that the Car, Truck, and Crane drove over the bridge from the left to right banks of the span portrayed in Figure 3.3. RL and LR denoted the situation from the Right bank to the Left bank and vice versa. During the dynamic loading test, a minimum velocity of 3 km/h and a maximum of 20 km/h was maintained to establish the global dynamic behavior of the bridge.

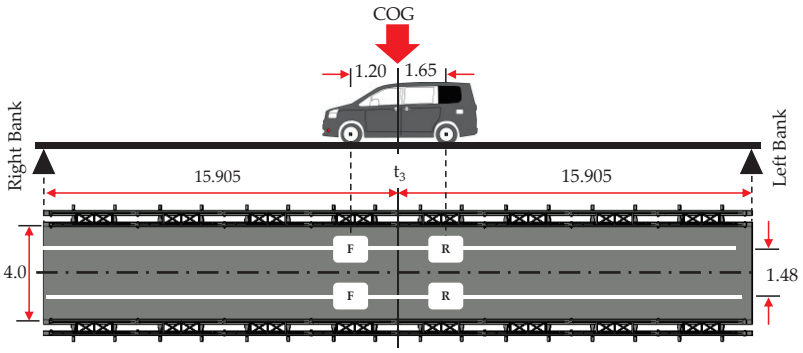

(a) Loading case 1; the target set at midspan (t_3) for measurement of displacement; Metadata: Car, wheel spacing of 1.48 m and axle spacing of 2.85 m.

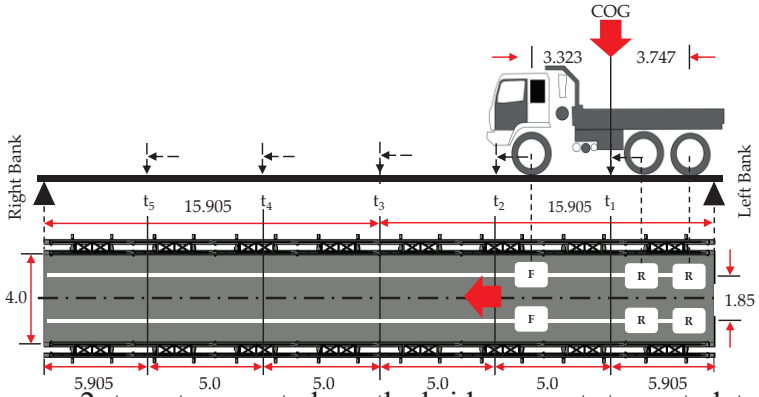

(b) Loading case 2; targets are set along the bridge span t_1-t_5; metadata: Truck, wheel spacing of 1.85 m and axle spacing of 5.7 or 1.37 m.

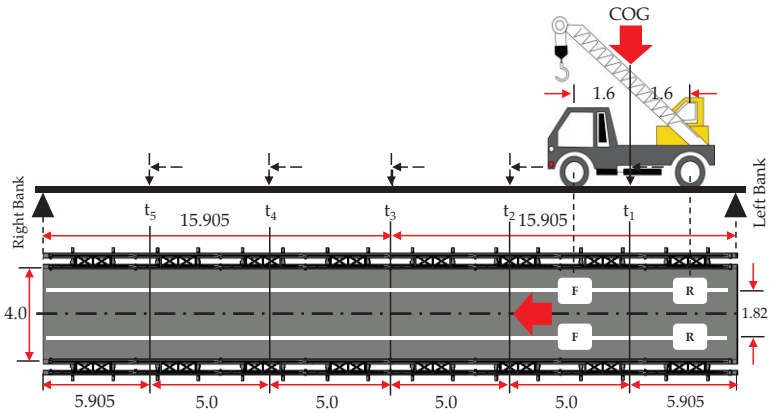

(c) Loading case 3; targets are set along the bridge span t_1- t_5; metadata: Crane, wheel spacing of 1.82 m, and axle spacing of 3.20 m

Figure 3.3. Static loading conditions (unit: m)

3.4.3. Measurement plan

The underlying reason for instrumenting [61] the bridge was to examine the response of the bridge under various loading conditions. The global deformation or deflection of the bridge is a measure of its stiffness [47,62]. On the other hand, stresses will give us the local behavior of elements that might prompt fatigue evaluation of the various elements [61]. Measurement instruments at our disposal were limited to the displacement transducers, Friction-type strain gauge, image processing approach, and MEMs accelerometer. The displacement transducers and image processing approach determined the deflection angle (θ) and deformation (δ). On the other hand, the strain gauges determined the local strains (ε) during loading, while the accelerometer established the structural dynamic response during loading.

3.4.3.1. CDP displacement transducer setting.

Figure 3.4a shows the set locations of the CDP - displacement transducers. CDP-type [63] strain gauge displacement transducers were exploited with a capacity of 25-100 mm, due to their stability, nonlinearity of 0.1% Rated Output, sensitivity of 100-500 ($\times 10^{-6}$ strain/mm), and accuracy of ± 0.1%. They were set at the end of the right and left end shears or post, attached to the bottom chord by a rigid magnet, demonstrated in Figure 3.4b, c denoted as R1, R2, R3, R4, L1, and L2 to achieve a good deflection and deformation profile. The deflection and deformation are attributed to the composite actions between the panels' chords and the respective members. Additionally, the transducers exclusively determined the displacement measurements under static loading conditions. To achieve the profile along both spans at intervals of approximately 0.400 m, 5.0 m and 5.905m, the deflection angle from a point normal to the bearing on the base plate was determined from Equation (3-2). The latter was diagrammatically summarized in Figure 3.4c. CDP displacement transducers were set on the abutment from a point 400 mm from a point normal to the bearing on the base plate presented in Figure 3.4b, c. They were then connected to a data logger DC-204R for recording voltage output emanating from the displacement Transducer. It, in this way, acted as a link to the PC, controlled by DC-7630 Tokyo Sokki as the system interface with multichannel capabilities.

$$\theta = \sin^{-1}\left\{\frac{V_0 - V_1}{r}\right\} \qquad \text{Eq. 3-2}$$

Where θ – Deflection angle, V_0 – Initial transducer reading, V_1 – Transducer reading after loading, r – Distance between the displacement transducer and point on the base plate and normal to the bearing.

In consequence, to resolve for the elastic deflection i.e., deformation profile we were interested in determining the rotation at individual target locations i.e., $t_1 - t_5$, employing an analytical approach because of the structural characteristics of bailey bridge panels [18] being analogous to composite plate beams [64]. Therefore, energy methods i.e., strain energy, principle of virtual work, and Castigliano's and geometric methods i.e., double integration method, moment area method and conjugate beam method were at our disposal [65–68]. Geometric methods are the most preferred due to ease in determining the elastic curve, although when resolving for deflection of specific point along the elastic curve the methods are cumbersome. However, the moment area method was best suited since it is based on the area under the bending moment diagram and can conveniently determine the relative slope and deflection at any point on the elastic curve [69,70].

Additionally, for more complex problems where the flexural rigidity is not uniform throughout the length of the beam, the conjugate approach is takes precedence which is based on the moment area method [71] — improved moment area method. Two theorems are utilized in calculating the deflection angle (First Theorem) and vertical displacement (Second Theorem) presented in Equation 3-3a and b respectively. The flexural rigidity was constant on both theorems; hence the first theorem was substituted in the second theorem to obtain Equation 3-3c through solving for the flexural rigidity to establish the deflection at the center span. Further, the deformation at various locations on the span was examined by considering one section of the span was longer than the other that is side A longer than side B i.e., (L – α) and (α) in that order. The deflection was obtained by the sum of the span with the shortest section under evaluation descripted in Equation 3-3d and the other section obtained through symmetry [18,43] due to its nature of being analogous [64], hence translated to the other section.

(a) First theorem:

$$\theta_B - \theta_A = \mathrm{A/EI}$$

(b) Second Theorem:

$$t_{B/A} = \mathrm{A\bar{x}/EI}$$

(c) Deflection angle:

But deflection and deformation at the centre span:

$$\{\theta_B - \theta_A\} = \Delta\theta = \frac{\mathrm{PL^2}}{\mathrm{16EI}}$$

$$\delta = \frac{\mathrm{PL^3}}{\mathrm{48EI}} \qquad \text{Eq. 3-3}$$

The flexural rigidity is constant across the theorem hence:

$$\delta = \left\{\frac{\theta \times \mathrm{L}}{3}\right\}$$

However, targets other than the centre span of the structure:

(d) When the target is a distance ‘α’ from one end of the span

$$\delta = \left\{\frac{2\theta \times (\mathrm{L} - a) \times a}{\mathrm{L} + a}\right\}$$

Where A Area under the curvature, EI Flexural rigidity, $\bar{x}$ Centroid, δ vertical deformation, P Force or applied load, L Span length, α the distance from end of the span to the point in mm ($< \mathrm{L}/2$).

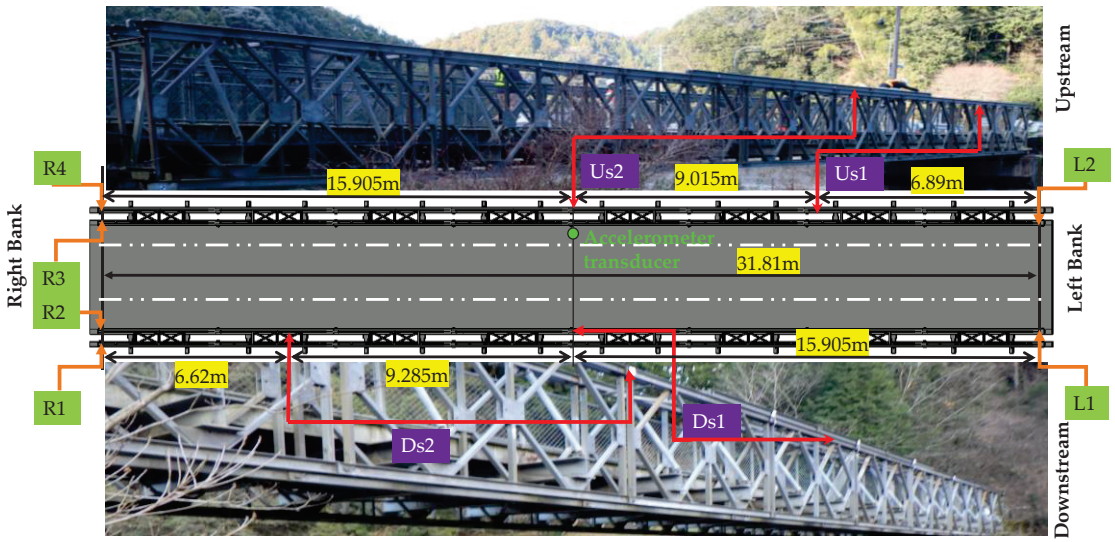

(a) Measurement setup

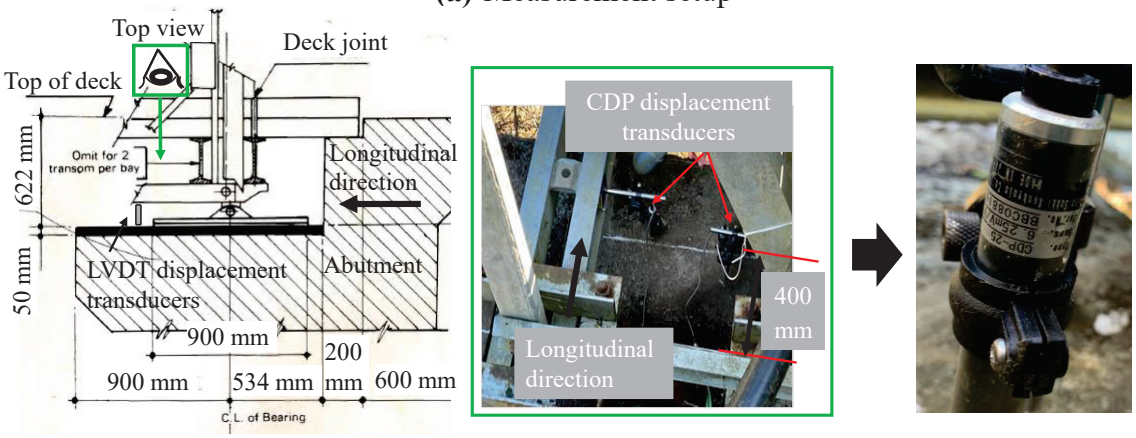

(b) CDP Displacement Transducer setup

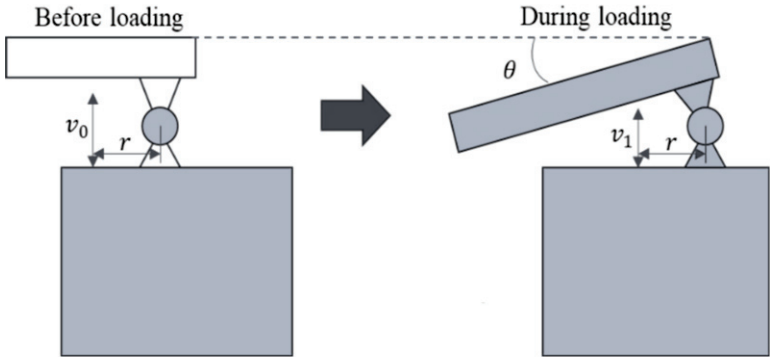

(c) Determination of the deflection angle

Figure 3.4. Measurement Plan

3.4.3.2. Strain gauge setting

Figure 3.4a also show the location of the Frictional type strain gauges [58] attached. The location was chosen to understand the symmetrically bending moments and local behaviour of the components of the Sukumo bailey bridge. Bailey Bridges have maximum compressive stresses at the centre bays' top chord [18,29,43]. Hence, the gauges were placed on the top chords and both sides of the inner bridge panels' web section. They were denoted in relation to the flow of the stream where Us and Ds meant Up-stream and Down-stream likewise. As a result, they were symmetrically skewed along the centre line, Us2 and Ds1. On the other hand, Us1 and Ds2 were placed approximately 9.015–9.285 m from the centre line completing the skew symmetry as detailed in Figure 3.4a. Their placement on the top girder ensured maximum global response. The magnetic frictional strain gauges were the FGMH series with a gauge length of 1.0 mm. They consisted of a rubber layer on their contact surface and a magnetic ring pressing against the web-section on the top chord. Strains are recorded due to friction caused by the target surface because of acoustic emissions [58]. They were wired to the end shears of the bridge with insulated, low-resistance copper wires approximately 15 m long on both spans. They were then connected to a quarter bridge (for voltage input) and a microprocessor data logger DC-204R system through a converter connected to a PC as the controller DC-7630 Tokyo Sokki for calibration, manipulation, visualization, and data extraction interface. The controller had eight channels on either side of the bridge for the strain gauge, and the displacement transducer had a shared interface.

3.4.3.3. Target setting for image processing approach.

Figure 3.5 shows the configuration of the image processing approach employing MOVIAS neo by Nac. Image Technology Co., Ltd. located in Akasaka, Minato City, Japan, which is widely used in automotive crash test analysis [57]. The targets were Quadrants deployed to track the frames for deflection. They were set at 5.0 m at t_1 to t_5 on the top chord of both the left and right spans [57]. Figure 3.5a presents the target setup along one of the spans. The approach is an improvement from conventional totals station that only monitors one point, leading to limited information rather than point cloud data [46,47]. The deformation of the targets was recorded from different monochrome cameras, shooting angles, and resolutions of A: 4608 × 3456 pixels, B: 5472 × 3648 pixels and C: 5184 × 345 pixels. Figure 3.5b illustrates how the image processing approach determined the deformation. A preselected, fixed reference point was established during the experiment for calibration using the recommended spatial resolution on the user interface the guard rail bolt, as shown in Figure 3.5c. The guard rail bolt was then used to determine the displacement in reference to the target Quadrants. With a minimum resolution of 15 pixels, high center detection accuracy can be achieved on the quadrant. The target was set so that the pixel luminance information coincides with the template size [57]. Hence, the difference (Δh) is then resolved as the deflection value encapsulated in Equation (3-4). The instrument was only used during static loading due to scan time delays.

$$(D_0 - D_n) = \Delta h \qquad \text{Eq. 3-4}$$

Where, D_o Deformation reading after loading, D_n Deformation reading before loading, and Δh Deformation or deflection in mm.

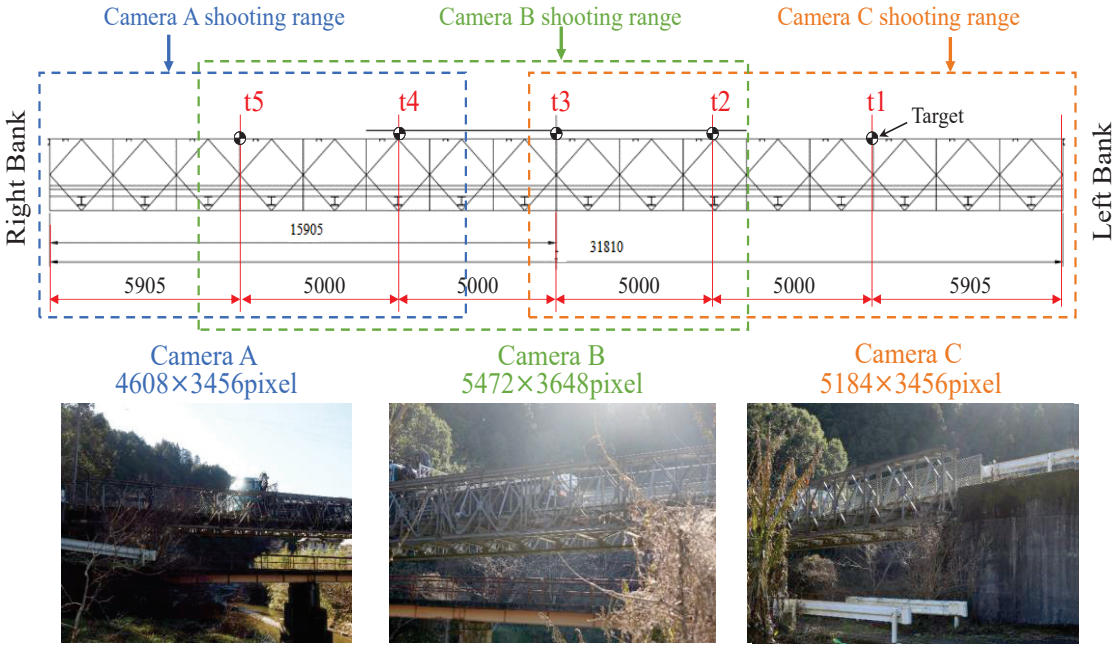

(a) Targets are set at specific spots t_1 – t_5, and structural responses are determined from the recorded frames – Plane view.

(b) Determination of a deflection based on the relationship of the target and fixed guard rail bolt - Plane view.

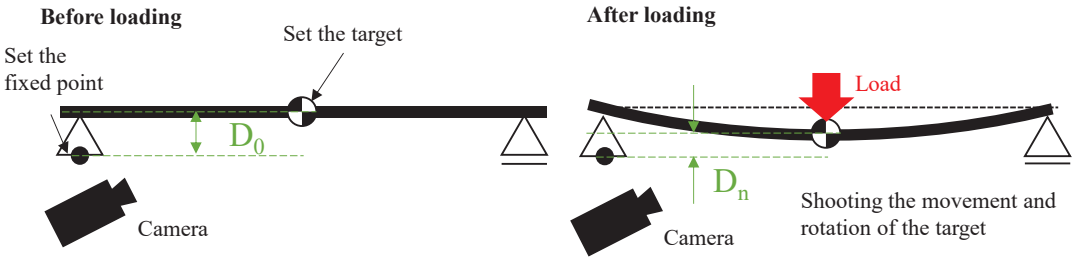

(c) Preselected rigid reference point – the guard rail bolt.

Figure 3.5. Image processing setup

3.4.3.4. Accelerometer Transducer setting

Figure 3.4a also shows the set location of the MEMs accelerometer transducer at upstream side on the center span and above the concrete deck. The device is an INTEGRAL PLUS sensor with 15-min real-time deflection measurement capabilities. The sensor was adopted under a new technology information system within the Ministry of Land, infrastructure, transport, and Tourism Japan for inspection support. It is suitable for bridge spans less than 40 m, with a maximum running test of 40 km/h and an accuracy of 0.08 mm for steel bridges [72]. It was placed at the center span, as shown in Figure 3.4a, on the upstream girder side of the structure. It measured the dynamic behavior of the structure [72–75]. The measure of the vertical displacement of the structure against time under different loading conditions was meant to determine the in-service behavioral response. Such conditions illustrate the ambient condition of the structure relating to its day-in response [72].

Several parameters are employed in evaluating a structure's dynamic condition, such as the natural frequency, vibration modes, damping, and Dynamic Amplification Factor (DAF) [76,77]. Among them, DAF is considered a critical parameter introduced in bridge design codes, for example, AASHTO 1996, 1997, and Eurocode 1-2. It establishes the structures' inherent uncertainties that correlate with other dynamic effects, such as pavement condition and extent of deterioration. Thus, it can contribute to bridges' structural condition. Therefore, a structural condition assessment of the Sukumo bridge was based on DAF. It was calculated using Equation (3-5) [28,29].

$$\mathrm{DAF} = (1 + \mu) = 1 + \left\{\frac{R_{dyn} - R_{stat}}{R_{stat}}\right\} \qquad \text{Eq. 3-5}$$

Where R_{dyn}, R_{stat}, and μ denote maximum dynamic, static response, and dynamic amplitude (deflection or deformation).

3.5. Results of the field experiment

3.5.1. Static behaviour

Figure 3.6 shows the deflection angle calculated from the transducer measurement and image processing approach. In this figure, three loading cases are shown; case 1 (1.57 Tons), case 2 (12.24 Tons), and case 3 (19.66 Tons). The deflection angle calculated from the transducer on Loading case 1 ranged from 0.0004 – 0.0066 with a difference of 0.01; between R4 and R3, causing a deformation ranging from 0.0030 – 0.0460 mm. On the other hand, loading case 2 had a deflection angle ranging from 0.0166 – 0.0596 with a difference of 0.04 and deformation of 0.1160 – 0.4160 mm, while Loading case 3 recorded deflections from 0.0278 – 0.0925 with a residual of 0.06 with deformation of 0.1940 – 0.6460 mm. A deformation (θ) of less than 0.1 from Equation (3-2) was considered reasonable. It meant the structure operated using the concept outlined in Equation (3-1) (principle of super-position). However, transducers R3 and R4, revealed in Figure 3.6c, and d exhibited higher deflections from Loading case 2. It was suspected to be due to the calibration and sensitivity of the transducer to higher loads. On the same note, the image processing approach recorded deflections increasing from Loading cases 1–3, that is, loading case 1 – 0.0079 (0.0548 mm); Loading case 2–0.0340 (0.2377 mm),

and Loading case 3 – 0.0492 (0.3435 mm), with minimal mean deviation from the transducer measurements of 0.0043, 0.0016 and 0.004 from Loading case 1 in that order, exemplified in Figure 3.6. Significant $\Delta\theta$ residuals were observed between the displacement transducer and image processing approach. The Bailey Bridges consist of several panels [38] on each span connected with pins whose tolerances vary. As a result, the pins reset during loading [18], leading to large deflections depending on the spans' side (left or right span). Moreover, the bending moment along the panels does not assume a perfect circular curve because the spans are an assembly of panels having approximately similar rotational angles as opposed to a single continuous beam using the second theorem ($t_{B/A} = A\bar{x}/EI$) in Moment area method. Whereas $t_{B/A}$ tangential deviation, A area under the curve on a cantilever beam, $\bar{x}$ centroid, EI flexural rigidity (E modulus of elasticity and I moment of inertia) [69,70]. Therefore, determining deflection from distinct locations will give rise to varying results, displacement transducer at 400 mm, and image processing method at 5.905, 10.905, and 15.905 m. Further, the image processing method's targets were on the top chord which experienced compression during loading. On the other hand, the displacement transducer was on the lower chord, which was vulnerable to tension [29,70]. The phenomena correspondingly affect the deformation profile hereafter presented in Figure 3.7.

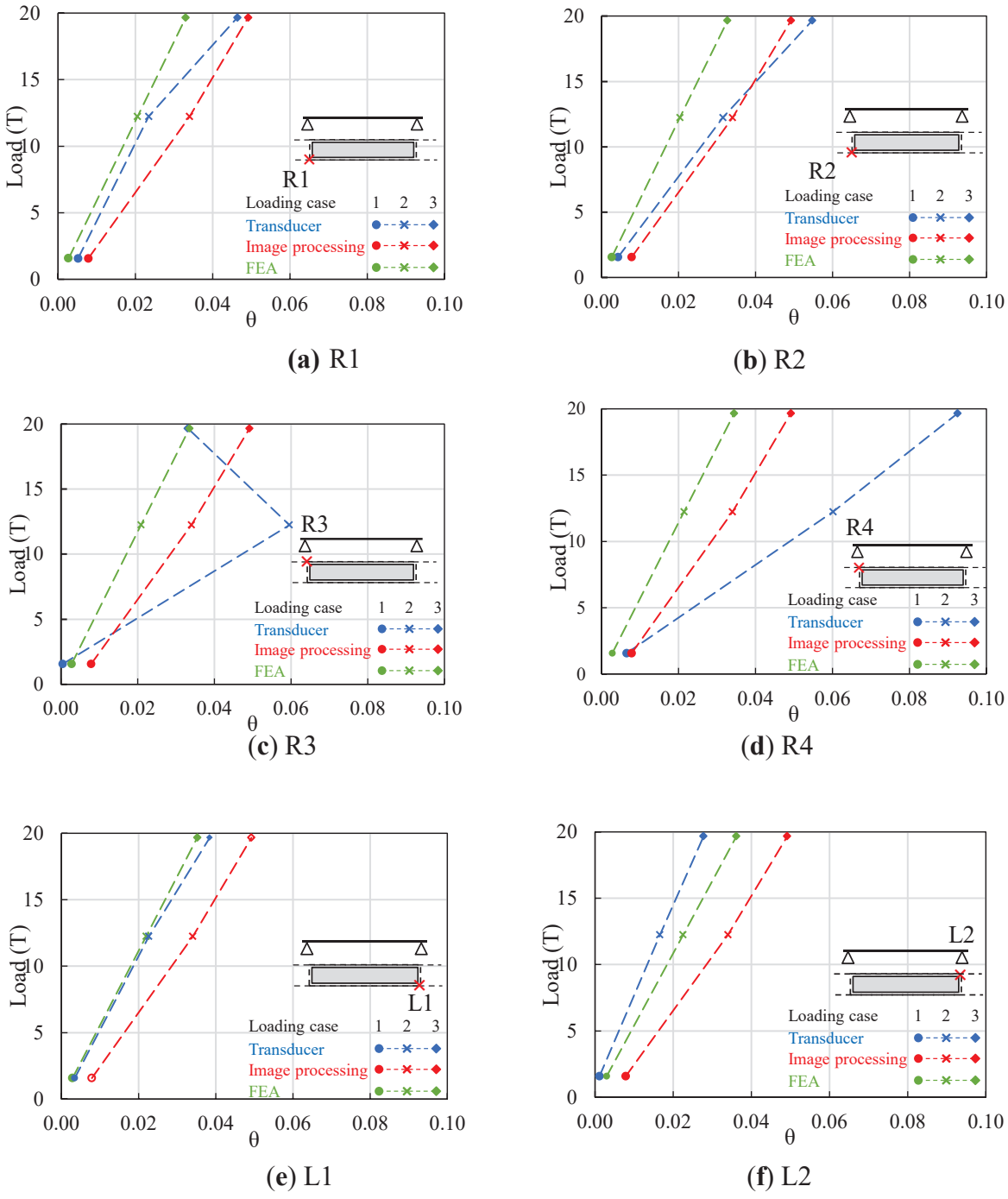

Figure 3.6. Deflection angle calculated from transducer and image processing measurements and FEA at selected locations on the bridge.

Figure 3.7 shows the mean deformation profiles along the bridge span. From the results, the profile showed symmetry at the centre of its span, increasing from loading cases 1 to 3 on both the transducer measurement and image processing approaches. The computed responses were averaged to obtain one similar profile for comparison of structural response across the distinct instrumentation setups. The deformation at the centre span was higher with the image processing (compression members) than with the displacement transducer (tension members) [29,70] with a difference ($\Delta\delta$) of 3.65 mm. The results show a linear-elastic behaviour having approximately similar characteristics in both approaches. Moreover, the mean deformation profile indicated an increasing bending moment from the end shears to the centre of the span [43]. The phenomena were similar in both spans. In reference to the AASHTO 2010 Bridge design specification, the permissible in-service loading including impact is span/800 [78], translating to a maximum allowable deflection of 39.73 mm on a bridge span of 31810 mm. Additionally, the theoretical pinhole sag ($\text{Sag} = dn^2/8$) of 28.48 mm for self-weight, where d was 3.56 (constant), and n was 8 number of bays. From the experimental results, the maximum deflection obtained was 13.66 mm from the image processing approach and approximately 10.50 mm for displacement transducers' influence lines that are below the prescribed limit of (span/800 → < 39.73 mm) illustrated in Figure 3.7.

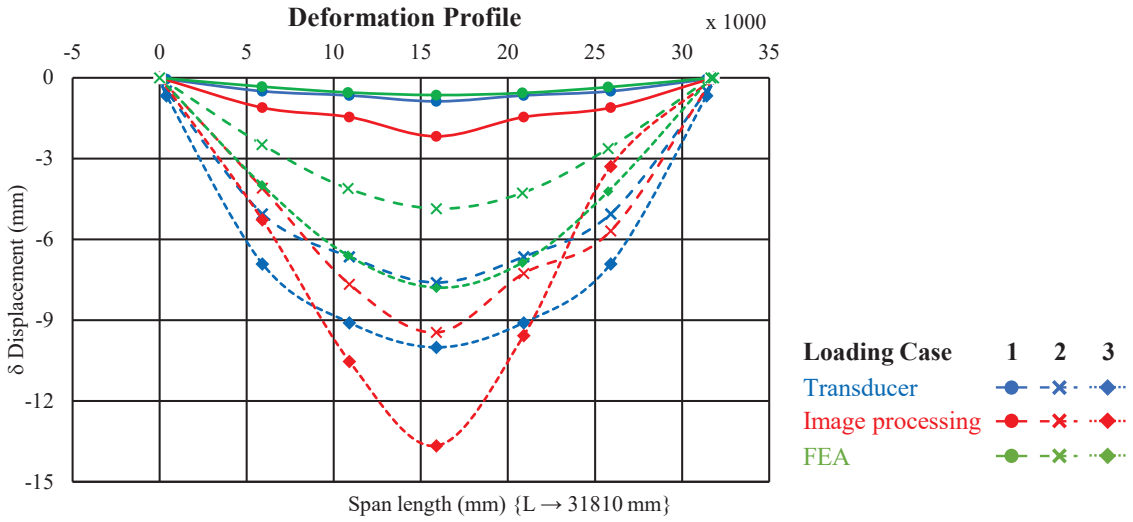

Figure 3.7. Mean deformation profiles under loading cases 1, 2, and 3 along the five targets on the bridge span.

Figure 3.8 illustrates the load versus strain relationship. Bailey Bridges experience significant stress at mid-span than end-shear during loading [43]. This aspect is of great importance in designing truss structures ensuring reinforcement of the critical elements at the mid-span that are fully stressed. The strains were established during loading cases 1–3. Figure 3.8a, b indicates the effects of strain with loading. The strains increased with the loading with no anomaly to indicate underlying local issues such as fatigue. The strains had similar characteristics apart from differences due to the strain gauge placement distances, which were not precisely co-linear (Us1 & Ds1) and alternate (Us2 & Ds2). However, a symmetric relationship varies from the center, as shown in Figure 3.8a, b. The situation is critical for fixed-panel bridges indicating that the end posts or shears are not fully utilized. Consequently, reinforcing the center bays ensures uniform distribution

of stresses. The panel stresses were computed from the mean values of Us1 and Ds1 with a modulus of elasticity of 2.0×10^5 MPa for a steel superstructure with a concrete deck. It was clear that the bridge operated within the linear elastic range. Moreover, the stresses experienced in Loading case 3 correspond to a similar study on the same bridge [79].

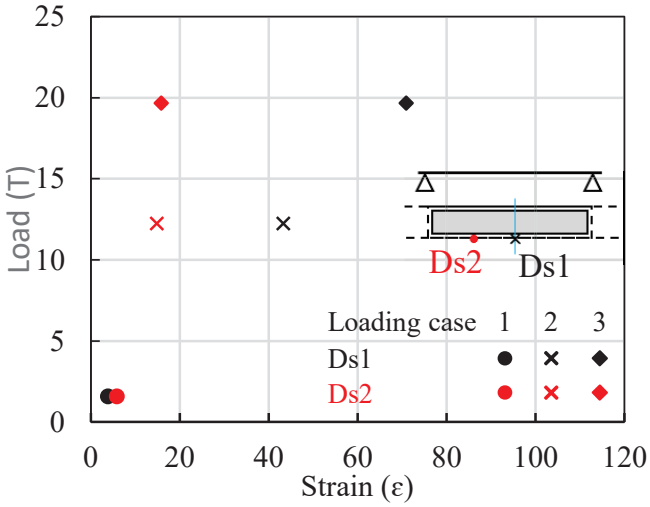

(a) Downstream

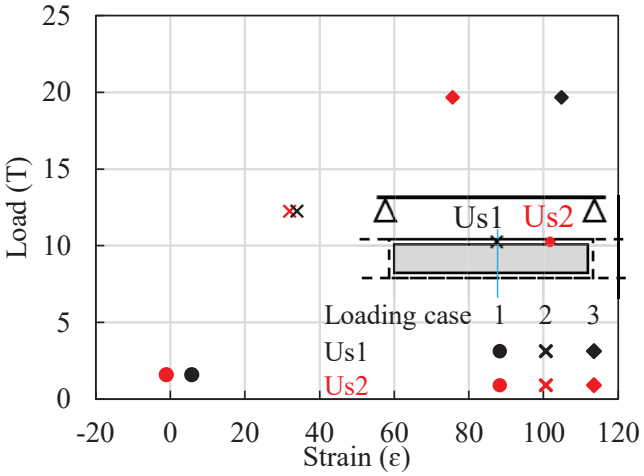

(b) Up-stream

Figure 3.8. Load vs. Strain Relationship

3.5.2. Dynamic behaviour

Figure 3.9 illustrates the structural dynamic response. Figure 3.9a-c relays the various loading cases, indicating the structural dynamic response. Measurements were recorded from cases 1–3 with an average speed of 3–20 km/h practicable to prompt the dynamic structural effect, with 3 km/h considered the crawling speed and 20 km/h considered the average speed [72,76,80,81]. The deformation response ranged from 0–0.031, 1.30–1.932, and 11.249–15.844 mm from the loading cases and 7.42 mm from a 15 T load from a similar study [79], respectively, as indicated in Figure 3.9d. Similarly, the current study had an approximate response of 8.62 mm on corresponding load of 15

T from the previous study — extrapolated from the sampled dynamic responses, the differences are attributed to the instrumentation and specific location where the global response was obtained [18,82]. The responses were random due to the dynamic nature of the decking section. As a result, the structure would seem nonlinear compared to the static response [80]. However, it was observed that the structural characteristic was linear from individual responses concerning the loading and unloading (arrival and departures) from the respective negative displacement amplitudes from Figure 3.9a – c. Each negative peak indicated the maximum deflection and deviation from it during unloading, corresponding to a linear elastic response [53,62].

The maximum dynamic deflection (12.72 mm) is evidently more prominent than the mean static maximum response (7.87 mm) by approximately 4.85 mm. From Equation (3-5), the DAF was derived as 1.05 with a structural span of 31810 mm of a one-lane bridge [76]. The parameter was well within the given threshold by ASSHTO 1997, indicating that the deterioration was significantly low and within maintenance margins [81]. Since DAF is a modal parameter that can reflect the dynamic performance of the bridge, it has proved to be a good indicator of the pavement condition on the decking section of the bridge. Consequently, it lays the foundation for a maintenance schedule concerning a well-conditioned pavement's desirable margins of 1.0 – 1.4 DAF. Structural failure constitutes numerous aspects, such as fatigue failure, surface wear, and corrosion, that manifest [72,73,75,83] under dynamic loading [80].

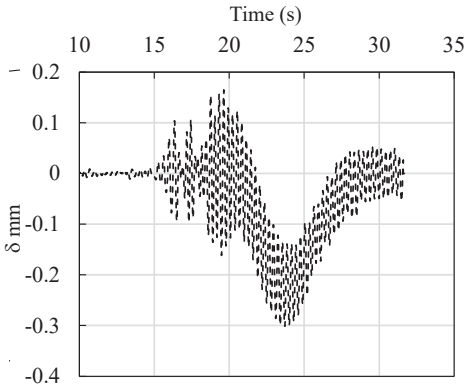

(a) Loading case 1.

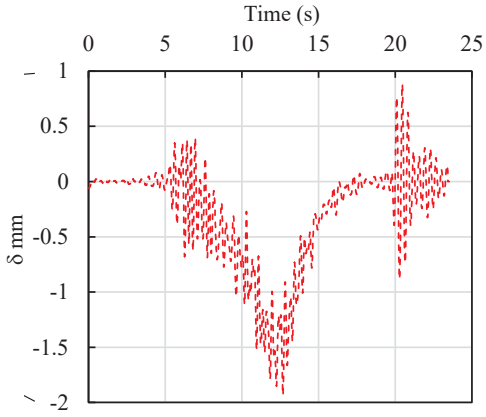

(b) Loading case 2.

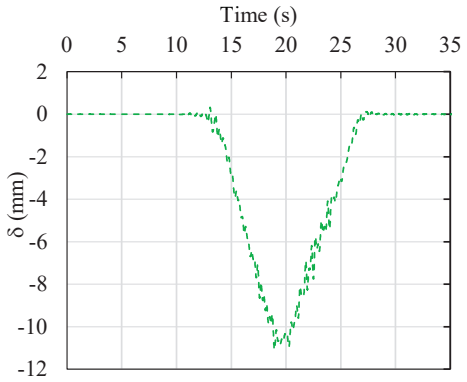

(c) Loading case 3.

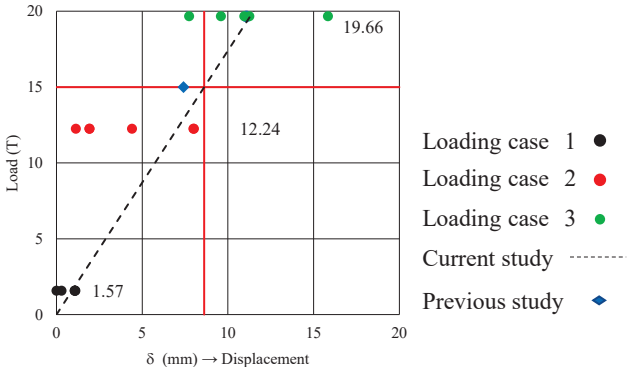

(d) Maximum — Least dynamic deflections at each loading case

Figure 3.9. Dynamic Response

3.6. Structural analysis

3.6.1. Structural modelling

An FEA was done to validate the bridge's static structural behavior. Figure 3.10 shows the numerical structural model. It was modeled according to in situ geometrical dimensions, as shown in Figure 3.2b, c. However, the detailed design and specifications were not available. By design, modeling should adhere to reliable documentation (as-built drawings) related to its geometry and material. The geometric structural details were recorded from the site. Instances where structural details are still unclear even after on-site measurement, the Japanese, Philippine [84], Garden Reach Shipbuilders and Engineers Limited (GRSE) [85], and Eurocode 1 & 2 [86,87] supplemented each other for any unclear details i.e., geometric properties. Consequently, the geometrical properties were considered with on-site dimensions provided in Table 2. A beam element with 6 degrees of freedom at the respective nodes was applied to the superstructure, employing a 1-Dimensional element family convention i.e., B32 (Beam, beam in a 3D space and quadratic). The beam element is mainly used for checking structural support systems. Quality is far more critical than complexity, as is commonly used in structural design [88]. As a result, increasing the computational speed beam element sufficed for the task. Some members were idealized; pin connections were modeled monolithically between the panel members [18]. The deck section was modeled as a shell element [88].

Loading was done at four points, considering the wheel spacing of the car, truck, and crane used in the field experiment. The support (bearing conditions) boundary condition stipulated free and fixed free ends, as shown in Figure 3.10 emulating a pin-roller bearing and pin bearing in that order [89]. Hence, the model assumed different types of boundary conditions to ensure an accurate result of the Sukumo baily bridge bearing. The first boundary condition stated a rotational moment on the x-axis and restrained on the z and y-axis and a translation while the second condition allowed only rotational moments on the x-axis assuming a pin/hinge type bearing and anchored to resist translational movement [79,90]. Permanent loads, specifically, the dead load of the superstructure minus the foundation settlement, were considered with a gravity value of 9.806×10^3 N/kg. This gravity force was applied first in all cases to deal with the dead load preceded by the live load. However, it is worth noting that wind, temperature, and earthquake loads were not considered for the reasons subsequently explained.

As the span and height increase, the wind actions become more critical. Aeroelastic reactions occur because of the dynamic action of winds impacting the galloping, vortex excitation, buffering, and parametric resonance phenomena. However, the subject bridge had approximately 9 m clearance height and an aeroelastic instability of 4 & 2.16, corresponding to the span-to-width and span-to-depth ratio. Due to the consequent aeroelastic instability, it was considered not wind-sensitive (Aeroelastic instability ≤ 30) [78,91–94]. Further, thermal distortions are significant when the superstructure is erected at temperatures that significantly differ from its in-service condition (Δ12 °C-annually), causing deformation by internal actions on constrained sections (welded and pinned joints). However, the bridge's flexible structural form allows thermal distortions of no serious consequence to generate a theoretical structural distortion of less than or approximately 13 mm [12,95]. On the other hand, earthquake actions relate to translational actions to the base foundation, that is, inertial forces dependent on the geographic location. Earthquake loads need not be observed unless the acceleration

coefficient [12] exceeds 0.15 [96]. In that regard, the chances of an earthquake generating an acceleration coefficient of more than 0.15 are close to zero in the next 50 years [97]. This analysis was performed in ABAQUS CAE 2019 Software with a static solver, due to its ability to address linear and nonlinear material and geometric [98] aspects.

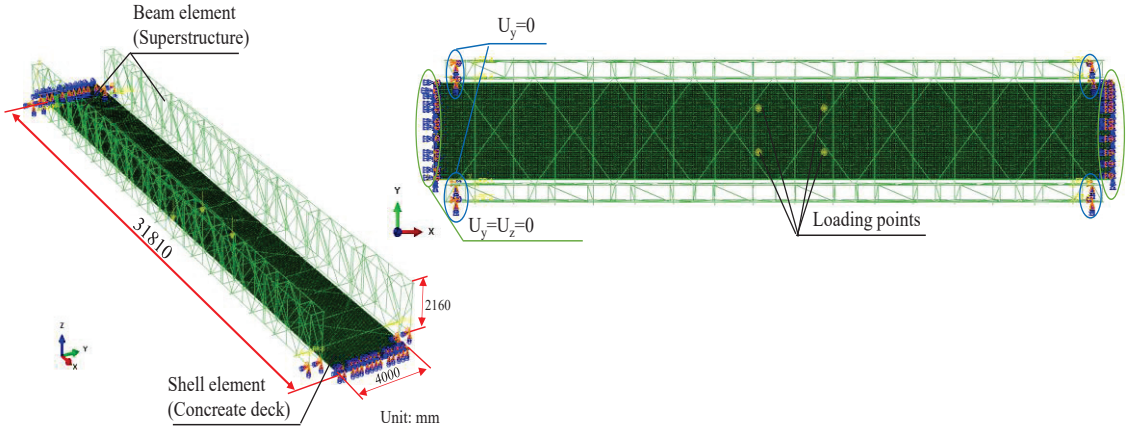

Figure 3.10. Analytical Structural Model

Table 3.2. Onsite Structural Dimensions

S/No.	Description	Section	Dimensions (mm)				
			H	B	t_w	t_f	Diameter
1	Top and Bottom Member	Channel	103	65	9.2	7.5	-
2	Transom/Cross Beam	I-Section	300	300	10	15.6	-
3	Vertical & Diagonals	Box	78	78	7.2	7.2	-
5	Chord reinforcement	Channel	103	65	9.2	7.5	-
6	Sway brays	Rect. Plate	-	-	-	-	-
7	Bracing frame	Channel	75	36	8.5	5.8	-
8	Tubular racker	Tubular	-	-	-	-	d-36; t-8.85
9	Tie-plate	Channel	75.67	38	5.7	7.5	-
10	Racker	Channel	75	36	8.5	5.8	-

3.6.2. Material Modelling

Figure 3.11 illustrates the bilinear stress-strain model. The material properties were adopted from the Bailey Bridge manual, AASHTO 2010, and GRSE of a similar bridge design with Young's modulus of 2.0×10^5 MPa and Poisson ratio of 0.3 [43]. Moreover, it corresponded with previous studies [7,29,79]. In the present study, a linear analysis was performed to validate the model's accuracy, and a nonlinear analysis for the bridge's reliability. The superstructure was set as SM490 steel with a yield strength of 325 MPa (fy). The deck section was composed of concrete material. Hence, a modulus of elasticity of 30,000 MPa and a Poisson ratio of 0.2 was adopted. On the other hand, the nonlinear analysis model had a yield strength of 325 MPa (fy) and ultimate strength of 400 MPa (fp) [30], as shown in Figure 3.11. The deck section made of concrete was constantly

linear elastic to grasp the nonlinear behavior of the panels and distribute the load evenly to the superstructure.

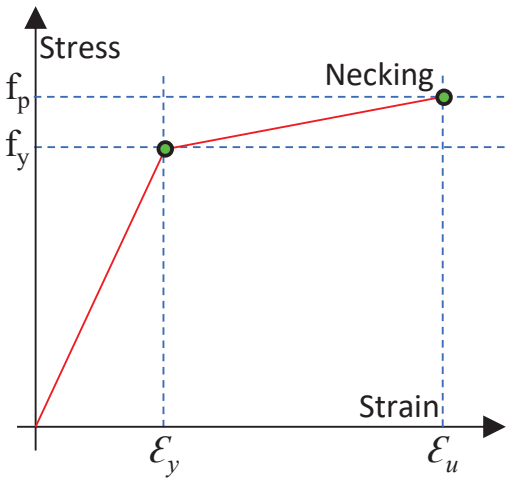

Figure 3.11. Bilinear stress-strain model

The interaction between the superstructure and concrete was not considered, serving as DSL's carrying surface. This approach of zero interaction focuses on distributing force to corresponding elements bearing the dead load. Furthermore, the stresses throughout the model were determined using the Von mises Stress (σ_{vm}) obtained from the Cauchy stress tensor derived from Equation (3-6). The model is suitable for evaluating structural truss systems experiencing small deformations.

$$\sigma_{vm} = \sqrt{\frac{\left[\left(\sigma_x - \sigma_y\right)^2 + \left(\sigma_y - \sigma_z\right)^2 + (\sigma_x - \sigma_z)^2 + 6\left(\tau_{xy}^2 + \tau_{xz}^2 + \tau_{yz}^2\right)\right]}{2}} \quad \text{Eq. 3-6}$$

Further to evaluate for both tension and compressive stresses, the maximum and minimum principal stresses were respectively employed. The stresses were derived from Equation 3-7.

$$\sigma_{1,2} = \frac{\sigma_x + \sigma_y}{2} \pm \sqrt{\left(\frac{\sigma_x - \sigma_y}{2}\right)^2 + \tau_{xy}^2} \quad \text{Eq. 3-7}$$

Where σ_x, σ_y, σ_z, τ_{xy}, τ_{yz}, σ_1, and σ_2 denotes the normal stress component in the X direction, the normal stress component in the Y direction, the normal stress component in the Z direction, the shear stress component in the Y direction applied on the plane normal to the X axis, the shear stress component in the Z direction applied on the plane normal to the X axis and is the shear stress component in the Z direction applied on the plane normal to the Y axis, maximum principal stress and minimum principal stress in that order and .

3.6.3. Linear Elastic and Nonlinear Elastic-Plastic Analysis

3.6.3.1. Condition of Linear Elastic Analysis

A linear elastic analysis was done to obtain the deflection using the Newton-Raphson method [98] and to validate the model's accuracy (using ABAQUS CAE 2019). The loading was prearranged such that the front and rear axles were in ratios of 4 to 3. It was considered that the front axle had a higher capacity due to the location of the engine. The displacement control loading scheme was organized in successive and equal amplitudes of 1.75 Tons ranging from 0-26.25 Tons at a frequency of 1 s at intervals of 0.2 s in the field output request. This approach was meant to accurately resolve for the exact solution rather than extrapolating the value from the general solution. Therefore, to assess the support conditions and its corresponding accuracy a similar load step (15 T) and boundary conditions (pin-roller and pin bearing support) were deployed comparable to the previous study [79]. Additionally, Loading cases 1-1.57, 2-12.24, and 3-19.66 Tons, were set at distinct amplitudes of 0.13, 0.04, and 0.47 Tons respectively to precisely determine the deformation or deflection. The program also checked whether σ_{vm} for every element falls within the material's linear domain (from Equation (3-6)). After establishing the accuracy of the support, the boundary conditions were consistent.

3.6.3.2. Condition of Nonlinear Elastic-Plastic Analysis

The bending moments and compression on bridge elements occur as whole but not as separate elements. However, Eurocode 3 recommends verifying structures in SLS and ULS as constituent members [86]. Conversely, in-situ structures interact as a whole, and their interaction should be analyzed similarly. Bailey Bridges have numerous critical points of tension (bottom chord) and compression (top chord) members. They have pronounced stresses at the center span chord, as presented in Figure 3.8 and 3.9 from the field experimental data. During loading and unloading, Bailey Bridges have random dynamic and static behavior and are vulnerable to instability. The Newton-Raphson method does not account for nonlinearity for structures exhibiting buckling and material nonlinearity. Therefore, the reliability of the structure was assessed using the Arc length method. This method can check material and geometric nonlinearity [98]. In this study, it was first used to identify the linear response about the base state before the affected member fails-buckling. Moreover, the nonlinearity of systems when they exhibit numerous critical points were investigated, i.e., a body that cannot support an increase in load. Procedures of linear and nonlinear buckling analysis were detailed after this. It is worth noting that the used structural model, boundary conditions, and the material property were the same as mentioned in Figures 3.10 and 3.11.

Linear Buckling Analysis—Linear Perturbation

A four-point bending of −1 N on each loading point was applied on the deck section, coinciding with the position of the load cases used in the linear buckling analysis as the initial load. Then, the linear perturbation procedure was selected in Step and buckle as the option and subspace eigensolver. Though the number of the eigenvalue(s) required is only one - Mode 1 Eigenvalue, $n = 10$ was input as the minimum number of eigenvalues requested where $(2n, n + 8)$ is the minimum number of vectors. Hence, 18 vectors were used per iteration of a maximum of ≈ 300. A lower number of iterations was avoided to ensure convergence. The program applies increments to the load on the load control.

Non-Linear Buckling Analysis—Static Riks

First, geometrical nonlinearity and residual stresses were introduced through equivalent geometric imperfections, as recommended in EN 1993-1-1 (EC-3), as a prerequisite for designing slender structures. The imperfection was imported from the linear perturbation step. Secondly, the step was created using the general procedure Static Riks method that exploited the arc length method to account for the nonlinearity using Nonlinear geometry (Nlgeom). The maximum number of increments was set to 1.0×10^6 with an arc length of approximately 1. The load was concentrated force set as the First Eigenvalue from Linear Perturbation Analysis with similar boundary conditions, loading point positions, and material properties. Because the method does not terminate, it was terminated when the arc length is approximately less than or equal to 1. It was assumed that the structure fails when the stress values on critical members (chords) surpass $f_{p,}$ corresponding to span/800 of deflection value greater than or equal to 39.763 mm. Finally, the Load Proportionality Factor (LPF) was extracted, and the product of the values by the first eigenvalue from Linear perturbation [98] was determined and plotted against the deflection and the load-displacement curve.

3.6.4. Validation results of the model's accuracy within linear elastic region

Accuracy of the support conditions

Figure 3.12 shows the comparison of the results of different support conditions using effected deformation and stresses on the previous analytical and numerical studies [79] vis-à-vis the present numerical results. To clarify the accuracy of the support conditions on the model a similar load of 15 T was used on the model with similar boundary conditions as the previous model. A deformation profile of – 6.155 and – 6.231 mm were obtained from hinge + roller and hinge + hinge support conditions respectively. Similarly, the previous study had a corresponding characteristic displacement of approximately – 6 and – 6.3 mm in the same order illustrated in Figure 3.12 shedding light on the in-situ and ex-situ support conditions. The mises stress characteristic was also probed to understand the behavior of the support especially the right bank side i.e., stresses were more pronounced in the hinge + roller than the hinge + hinge supports indicated in the stress distribution nephogram in Figure 3.12. The pinned support that is the hinge + hinge condition brought numerical values close to the analytical and numerical values of the previous study indicating the accuracy of the model's support [79,90,99]. As a result, the support conditions were assumed as pinned support on both spans of the bailey bridge. The accuracy was also presumed to be affected by the monolithic nature of the panels modeling rather than pinned connection that is numerically simulated as beam end release [7,18] and due to the degradation of the support as a consequence of corrosion (galvanic corrosion) restricting rotational moments [99] that was evident during onsite visual inspection. However, the accuracy of the model was good.

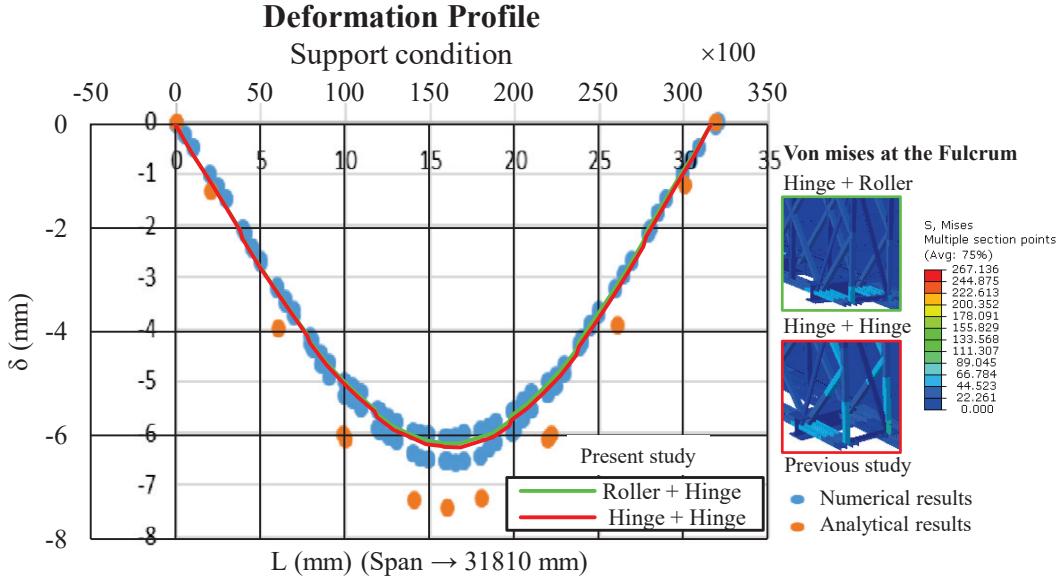

Figure 3.12. Support conditions — previous and present study (deformation and mises stress)

Static loading

Figure 3.5 - 3.6 shows the deflection and deformation results of instrumenting the bridge compared to the FEM model under the linear elastic domain (serviceability limit state - SLS). The validation coefficient (**η**) was determined from the deformation or deflection obtained from the model. The residuals and coefficients present the characteristics and agreement of the model. It further details the relationship of compressive and tension members, that is, the measurement from the top and bottom chord. Dissimilar characteristics of the model versus measurement approach and anomalous validation coefficients [20] disclose a poor connection between structural members and lower structural stiffness, prompting extensive evaluation [7,20]. The mean/average of the measured results is presented in Table 3.3 with their respective residuals and validation coefficients.

Table 3.3. Residuals and Validation Coefficient

Loading Case	F (Tons)	ẋ (*θ*)			Residuals		η	
		FEA	Transducer	Image/P	Transducer	Image/P	Transducer	Image/P
Case 1	1.57	0.0028	0.0035	0.0079	0.0007	0.0051	1.25	2.79
Case 2	12.24	0.0213	0.0357	0.0340	0.0144	0.0127	1.67	1.60
Case 3	19.66	0.0342	0.0488	0.0492	0.0146	0.0150	1.43	1.44

The mean deflection from transducers R1, R2, R3, R4, L1, and L2 recorded deflections ranging from 0.0035-0.0488 from Loading cases 1 to 3. On the other hand, the image processing approach recorded a mean ranging from 0.0079-0.0492 from Loading cases 1 to 3, a magnitude higher than the predecessor. The residuals had similar characteristics increasing from Loading cases 1-3. However, it was observed that compressive members had higher residuals than the corresponding tension members - the transducer measurements [29]. Therefore, the validation coefficient established the reliability of the model and structure, indicating a consistent ratio from both the

transducer and image processing approach. A higher ratio was realized on the image processing approach on Loading case 1, 2.79. The ratio was peradventure informed by characteristic inaccuracies of image processing on small deformations and dimension of the quadrant in comparison to the effected deflection. The coefficients show that the bridge is intact and close to the FEM model (Numerical model). The mean coefficient ratios of 1.45 and 1.94 for the transducer and image processing, respectively, indicate the model approximately fulfills the design requirements and operates within the elastic region. It is assumed the model idealized the in-situ bridge structure, paving the way for nonlinear analysis.

3.6.5. Identification of Critical Members before Determination of the Bearing Capacity

3.6.5.1. Identification Methods of Critical Members

Figure 3.13 indicates the class limits Class 1/Plastic (λ_p) and Class 2/Compact (λ_r). An assumption was made that members only shrink due to compression and not buckle by way of explanation; global buckling occurs first rather than local buckling. Therefore, critical members were identified from previous studies [7,29,79], secondly recorded field strains, thirdly FEA model and finally, Beam cross-section classification. Compression members suffer from large strains [7,79]. The principal stresses on the top chord with -261.738 Mpa are under compression of bailey bridges and the bottom chord under [7,79], which are generally under tension of 367.466 Mpa, similar to transoms identified from the linear analysis derived from Equation 3-6 and Figure 3.14a, b from the FEA model.

During loading, members experience either compression (top chord) or tension (bottom chord) and will fail when the stresses exceed the yield strength i.e., 325 Mpa. However, during compression members can also fail through buckling (local/global) that initiates a loss of stability when the critical value is reached. The structure can no longer support a load the way it was designed. Thus, the top chord of a bailey bridge is at risk of compression since it is loaded in compression [29]. Slender sections are at a greater risk of buckling than broad ones hence, long slender sections are discouraged [86] though a remedy is provided by deploying bracing members and increasing thickness. The Euler formulation ($P_{cr} = (EI\pi^2)/L_e^2$) supports this intuition in relation to slender sections as a consequence, the nondimensional parameter — the slenderness ratio is used for classification of cross-sections to identify the extent of resistance and rotation against local buckling by resolving for the Critical stress (σ_{cr}) obtained by the quotient of Critical load and cross-sectional area of the section ($\sigma_{cr} = (EI\pi^2)/AL_e^2$). Slender sections have large slenderness ratio and local critical buckling stress ($\geq \lambda_p$ & $\leq \lambda_r$) [86]. Where P_{cr} Critical Load, EI Flexural rigidity, L length of the section and A Cross-sectional area. Conversely, stocky sections have low slenderness ratios with large critical buckling stresses ($\leq \lambda_p$). Therefore, the former is classified as Compact or Class 2 which can develop their plastic moment resistance but have limited rotation capacity because of local buckling. On the other hand, the latter is classified as plastic or Class 1 sections which can form a plastic hinge with the rotation capacity required from plastic analysis without reduction of the resistance. Sections under Class 1/Plastic cross-sections is least susceptible to local buckling while Class 2/Compact likely to succumb to local buckling in that order i.e., Class 3 to Class 4.

Figure 3.14 shows the compressive and tension members when 19.66 Tons were applied to the linear elastic analysis. It was noted that critical members of rolled steel sections are essentially slender compared to their width-thickness ratio. Due to this awareness, some members experience local buckling before plastic stress is achieved, rendering the proposed approach irrelevant from the initial assumption. Therefore, critical members were classified (Class 1–4) and checked for susceptibility to local and global buckling. The Japanese [100], National Structural Code of the Philippines 2015 [84], British, and Eurocodes [86] (Eurocode 3, Clause 5.5, 6.1, and 6.2) derived the slenderness ratio (C/t) for the Web (WLB) and Flange (FLB) Local and Global buckling. The class limits Class 1/Plastic (λ_p) and Class 2/Compact (λ_r) were derived from Equation 3-7 through Equation 3-10.

Japenese code:

$$\lambda_p = \sqrt{\left((\mathrm{E}\pi^2)/\left(0.6 \times F_y\right)\right)} \qquad \text{Eq. 3-7}$$

National Structural Code of the Phillipines:

$$\mathrm{FLB} \rightarrow \begin{cases} \lambda_p = 0.38 \times \sqrt{\mathrm{E}/f_y} \\ \lambda_r = 1 \times \sqrt{\mathrm{E}/f_y} \end{cases} \qquad \text{Eq. 3-8}$$

$$\mathrm{WLB} \rightarrow \begin{cases} \lambda_p = 3.76 \times \sqrt{\mathrm{E}/f_y} \\ \lambda_r = 5.70 \times \sqrt{\mathrm{E}/f_y} \end{cases}$$

British code:

$$\mathrm{FLB} \rightarrow \begin{cases} \lambda_p = 9 \times \sqrt{275/f_y} \\ \lambda_r = 10 \times \sqrt{275/f_y} \end{cases} \qquad \text{Eq. 3-9}$$

$$\mathrm{WLB} \rightarrow \begin{cases} \lambda_p = 28 \times \sqrt{275/f_y} \\ \lambda_r = 32 \times \sqrt{275/f_y} \end{cases}$$

Eurocode:

$$\mathrm{FLB} \rightarrow \begin{cases} \lambda_p = 9 \times \sqrt{235/f_y} \\ \lambda_r = 10 \times \sqrt{235/f_y} \end{cases} \qquad \text{Eq. 3-10}$$

$$\mathrm{WLB} \rightarrow \begin{cases} \lambda_p = 72 \times \sqrt{235/f_y} \\ \lambda_r = 83 \times \sqrt{235/f_y} \end{cases}$$

Where f_y is the yield strength of steel section, C width of the section and t thickness of the section.

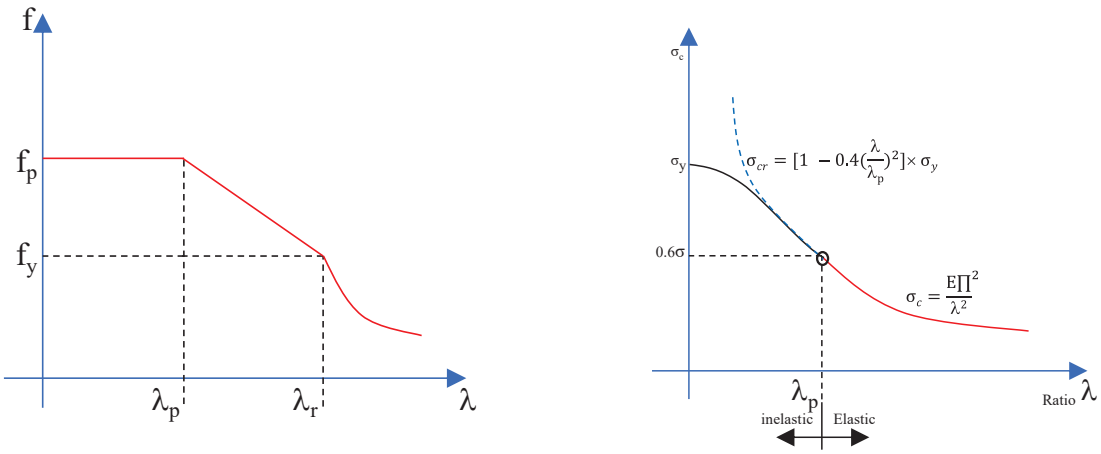

(a) Eurocode (CEN, 2011) (b) Japanese code (Miki, 2000)

Figure 3.13. Euler formulation for Slenderness Ratio

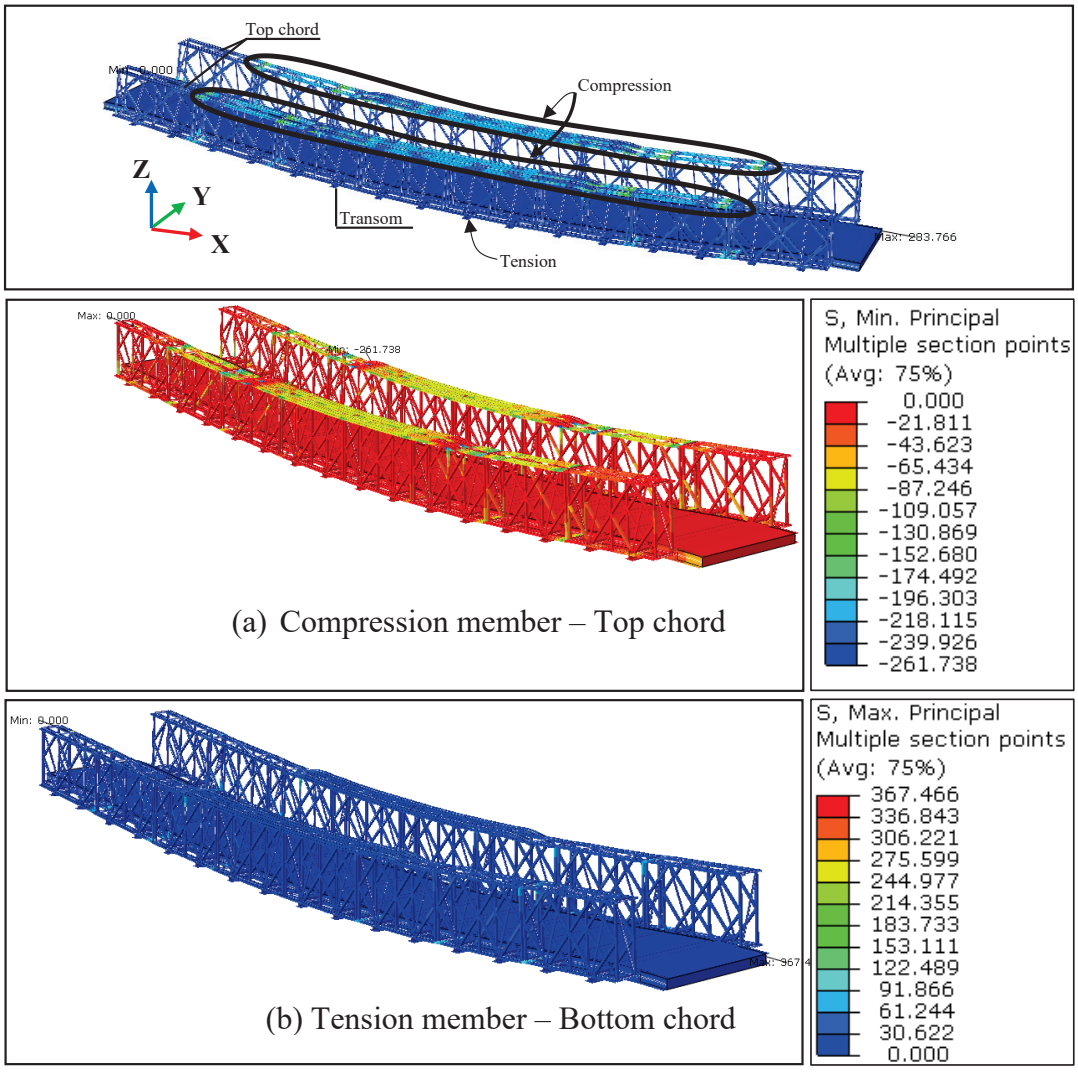

(a) Compression member – Top chord

(b) Tension member – Bottom chord

Figure 3.14. Compression and tension members nephogram of critical members

3.6.5.2. Results of Identification of Critical Members

The web and flanges of the dominant critical members from the linear perturbation procedure are slender and, as such, are prone to local buckling [86]. The arc length method is deemed immaterial without checking for local buckling using the Euler formulation for beam classification. This occurrence arose because of the compressive loading of the critical members (19.66 Tons on both linear analysis and on-site experiment). The first displacement is hence considered a failure (buckling Mode 1). It is regarded as the onset of the nonlinear response of the structure that also denotes the serviceability limit. Depending on the yield strength, members were classified according to a cross-sectional relationship of width-to-thickness ratio from plastic to slender classes according to British Standards and Class 1 to Class 4 - Eurocode [86,101]. These classes are because of their vulnerability to local buckling. The classes are organized from the least to most likely to succumb to buckling.

Table 3.4 demonstrates the class limit of both Flange Local Buckling (FLB) and Web Local buckling (WLB). Classes were derived from Class 1/ plastic (λ_p) class limits and Class 2/ compact (λ_r). The Japanese standard had a plastic limit of 56.76 on both FLB and WLB. The Eurocode had class limits of 7.65 & 8.50 and 61.22 & 70.58 for the FLB and WLB, respectively. In that order, the British standard had λ_p of 8.28 and 25.76 on the FLB and WLB; likewise, λ_r of 9.20 and 29.44. The Philippines code indicated more significant limits than the Japanese, Eurocode, and British codes. The code had λ_p of 9.43 and λ_r of 93.27 of 24.81 and 141.40 on the FLB and WLB correspondingly.

Likewise, the channel sections that experienced maximum compression FLB and WLB had a width-to-thickness ratio of 7.60 and 7.83 for FLB and WLB. In both cases, the stress distribution was well within the plastic limits - Class 1 (λ_p). Similarly, the I-section also achieved a ratio of 2.65 and 7.83 for FLB and WLB. All sections were established to be Class 1 (Plastic) using the slenderness ratio across all the standards, as presented in Table 3.4 [86]. It was found that global buckling takes precedence based on computations that is from Table 3.4. indicated that the sections are least likely to succumb due to local buckling. Therefore, the resistance of the members was considered adequate.

Table 3.4. Cross-sectional classification of critical members

σ Distribution	Standard	λ_p	λ_r	Slenderness Ratio	
				Chord	I-Section
FLB	Japanese	56.76	-	7.60	2.65
	Eurocode	7.65	8.50		
	British	8.28	9.20		
	Philippines	9.43	24.81		
WLB	Japanese	56.76	-	7.83	7.83
	Eurocode	61.22	70.58		
	British	25.76	29.44		
	Philippines	93.27	141.40		

3.6.6. Determination of the bearing Capacity by Nonlinear Elastic-Plastic Analysis

Figure 3.15a, b present the results of linear and nonlinear buckling analysis. They show the location of the local buckling mode one shape identified from the first out-of-

plane eigenvalue and the location of maximum von mises stress generation, respectively. The linear buckling process accounted for the linear response before the initial imperfection was regarded as a failure mode one, that is buckling. Hence, first, the analysis applied the weight of the concrete and superstructure preceded by the live load. Initially, the superstructure (critical members – top chords) was linear. The loads were incremented until failure mode 1 of the superstructure corresponds to a magnitude of 1. The phase is regarded as the initial imperfection caused by an incrementing load of 1 N, as described in Figure 3.15a. The resultant eigenvalue mode 1 was 1.06×10^6. The value was then used as the initial load on the subsequent nonlinear buckling analysis procedure [98]. The process is like linear buckling analysis; however, the structure experiences bifurcation when the compression chord starts to buckle on stresses beyond the yield strength of 325 MPa. With the onset of buckling, the structure begins behaving nonlinearly, indicated by stresses beyond the yield strength. The superstructure deforms with no significant load varying from a deflection more than span/800 at 353.936 MPa, as illustrated in Figure 3.15b. Due to the consequent geometric and material nonlinearity, the superstructure releases energy related to strains. The strains are associated with the LPF extracted from the failed structure presented in Figure 3.16a. The proportionality factor also corresponds to the displacement of the structure with respect to the applied load that was also extracted from the nonlinear buckling analysis, as illustrated in Figure 3.16b.

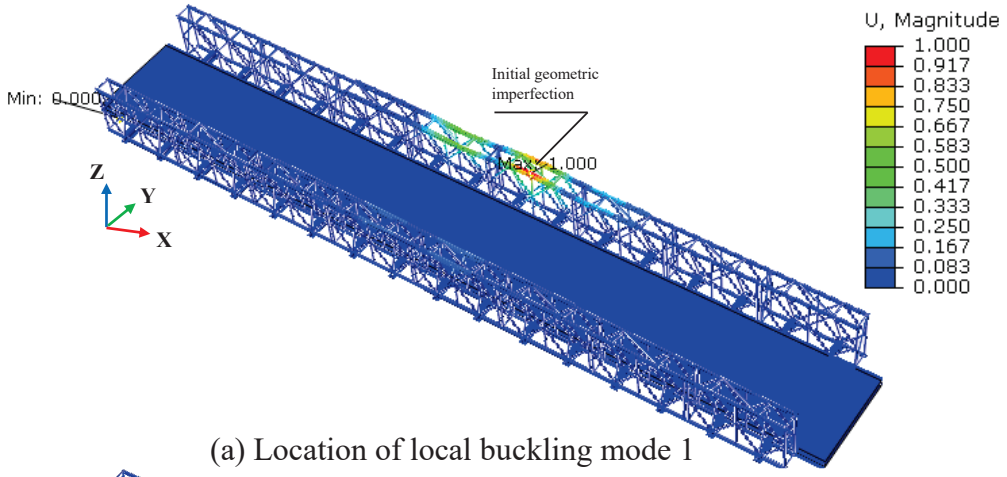

(a) Location of local buckling mode 1

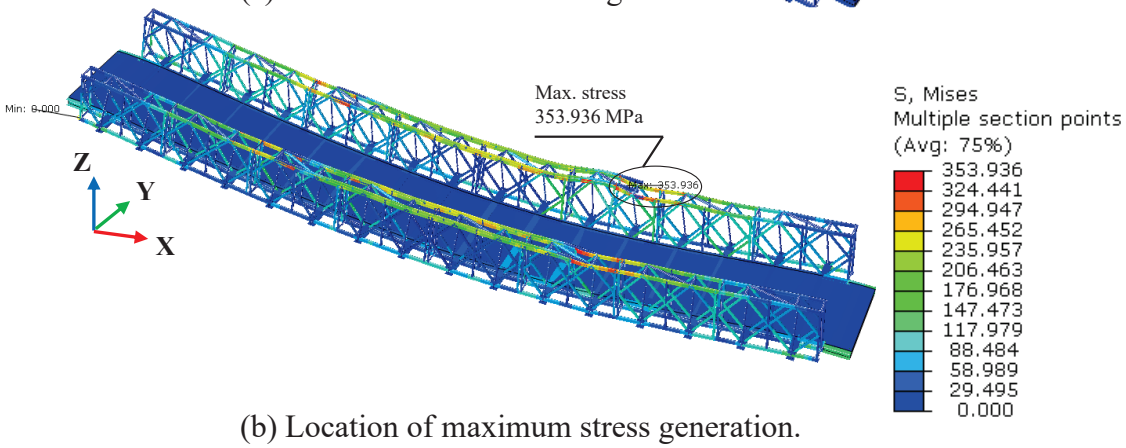

(b) Location of maximum stress generation.

Figure 3.15. Results of linear and nonlinear buckling analysis

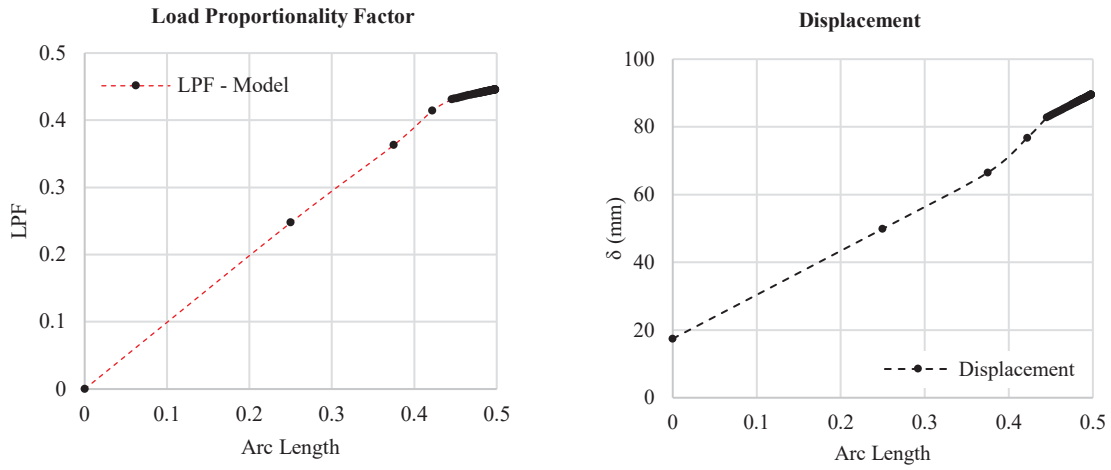

(a) LPF (b) Displacement

Figure 3.16. Relationship between Arc length and LPF/Displacement.

Figure 3.17 illustrates the location of the onset of yielding and eventual failure. Though failure occurs randomly, from the field experiment it was observed that the center span and top chord are the most vulnerable to stresses due to loading, similarly to dynamic loading [80]. In essence, the section can be used to determine the bearing capacity of the structure. A product of the LPF values by the eigenvalue mode one was considered the load or Force in Newtons ($F_n = LPF_n \times \mathbf{X}$). Where F_n Force, LPF_n^{th} Load proportionality factor and $\mathbf{X}$ eigenvalue mode 1 (constant). On the other hand, displacement was considered as the structural deformation. The onset of nonlinearity from 26.16 Tons was observed as the SLS with a material yield stress of 325 MPa. Thus, the capacity was regarded as the minimum load that caused the initial failure of the critical member. From the bilinear model, necking denotes the ULS of 47 Tons with an ultimate strength of 353 MPa, as described in Figure 3.17. The estimates agreed with the suggested hearsay of 25 Tons carrying capacity. The results indicated that the bridge was intact and operated elastically during loading and unloading within the linear-elastic region. The structure was globally linear, with a bearing capacity of approximately 26 Tons [27]. The redundancy ratio between SLS and ULS was around 1.81 ($\text{Redundancy Ratio} = 47/26$). The section can be utilized to increase the bridge's carrying capacity through structural reinforcement.

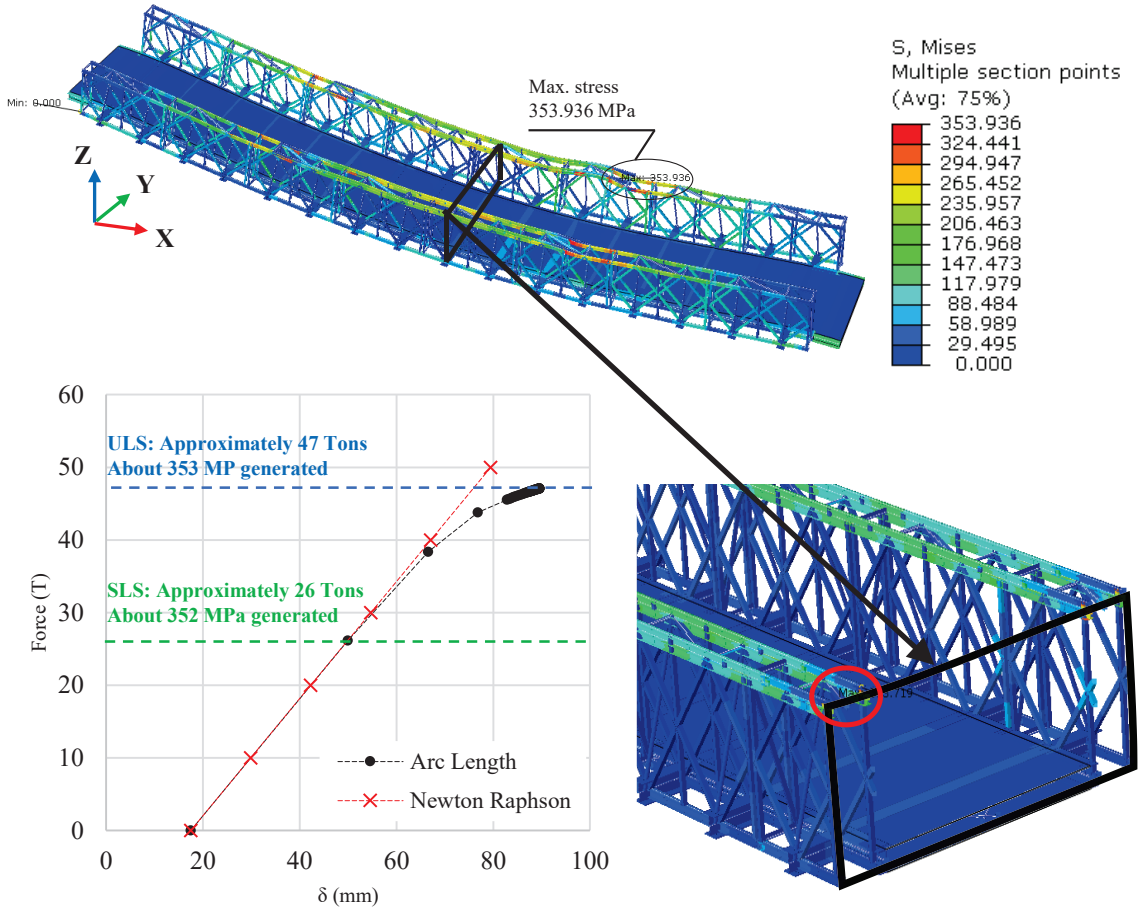

Figure 3.17. SLS and ULS

3.7. Adaptation Conversion Framework from Temporary to Permanent

Figure 3.18 present the summary of the conversion framework of bailey bridges from a temporary to permanent/semi-permanent steel bridge. Based on the field investigations and structural analysis the bridge is viable for conversion to permanent. This is also because of the strong demand from the locals. Due to its structural characteristics, it has sufficient load bearing-capacity to be accommodated as a town road. Moreover, with such proposal the municipal offices will initiate maintenance schedules in relation to the current local inspection manual and code [1,2,5]. Through the actual diagnosis of the capacity of the bridge the proposal was hereafter presented. The proposal is based on the verification of its capacity meant for temporary bridges. First the bridge was assessed for soundness by exploiting diagnostic — dynamic and static load tests (DSL) through field investigations. Further, a numerical model of the bridge was developed from onsite geometric and material measurements to evaluate for its linear and nonlinear performance and hence determine its bearing capacity. The model's accuracy was improved through clarifying its support conditions (hinge + hinge) and static loading by checking its validation coefficient on various Loading cases documented above i.e., Table 3.3. The numerical model [53] then forms the initial database of the assumed undamaged structure

that can be employed for condition assessment of the bridge during routine and periodic maintenance. The conversion process is summarised here under.

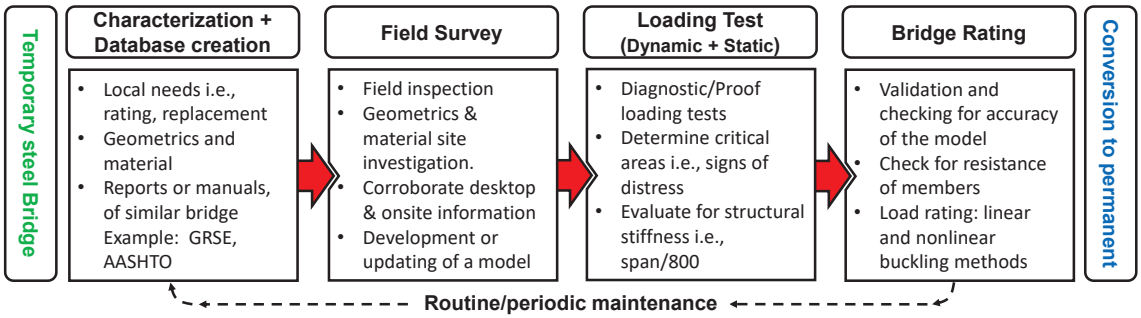

Figure 3.18. Adaptation and conversion framework

3.8. Conclusions

The research presents a study on the structural health condition and adaptation of the Acrow Bailey Bridge as a semi-permanent or permanent structure. Field experimental data were compared and validated with analytical methods for agreement making use of the present and previous studies. Further, a numerical model was deployed to establish the limit states (SLS and ULS) and bearing capacity using the Linear and Nonlinear Buckling (Linear perturbation and Riks) methods. The findings are presented hereunder.

Field experimental investigation:

Static loading

1. Loading case 1-3 gave deflection (θ) ranging from 0.0004–0.0066, 0.0166–0.0596, and 0.0278–0.0925, correspondingly, with a validation coefficient of less than 2 on both measurement approaches that were considered within the required threshold. Additionally, the support conditions were checked for correspondence with the previous study indicating a good accuracy with similar stress characteristics at the fulcrum. The maximum deformation at midspan was 13.66 mm on loading case 3.
2. In that order, the image processing approach recorded deflections (θ) of 0.0079, 0.0340, and 0.0492 from Loading case 1.
3. The transducer to image processing variance (Δθ) varied significantly, especially on Load case 1, by 0.0007 to 0.0050, indicating a good accuracy of the LVDT transducer on small deflections.
4. Stresses were derived from an SM490 steel material with young's modulus of 2.0×10^5 MPa from experimental field strains that increased from Loading cases 1–3 ($\varepsilon \approx$ 0–104.85) within the linear elastic region.
5. Static loading, under all loading conditions/cases, showed the structure operated within reasonable deflection (span/800- [39.3 mm]) and stress limits (below 325 MPa). The strain performance was also observed in typical symmetry at the center span, a trait common in Bailey Bridges.

Dynamic loading

1. The results of the structural dynamic response of 3–20 km/h were 0–15.55 mm from Loading case 1, recording higher deflection than static loading by 1.4 mm at midspan, on account of the maximum recorded deflection.
2. DAF (1 + μ) derived from Rdyn and Rstat resulted in 1.09. The DAF corresponded with the design criteria provided by Euro-code 1. The pavement condition was deemed ambient, with a limited deterioration range between 1.0–1.4.

Cumulatively the structure operated within the linear-elastic region and enjoys a good dynamic performance. Therefore, there was no problem or probable cause that would deter the normal performance of the structure.

Analytical investigation

1. DSL's field experimental and previous field study's results within the linear elastic domain validated the numerical model and elucidated the support conditions showing good agreement with a mean validation coefficient ranging from 1.4–2.0 and similar residual characteristics across all measurement approaches and accurate numerical influence line under similar support conditions.
2. The response of the model compared to similar research showed a good agreement.

The validated model defines the analytical geometry, material, and loads for nonlinear analysis (material and geometric).

Analytical assessment of the bearing capacity:

1. The results from the literature indicated that bridge structural elements operate in sync; therefore, their examination, espoused in Eurocode 3, gives conservative results.
2. The out-of-plane eigenvalue mode one vector was established to have a first eigenmode value of 1.06 × 106 from an incrementing load of an initial magnitude of 1.
3. The result of the nonlinear analysis indicated 26 Tons and 47 Tons as SLS and ULS, respectively, as the bridge's bearing capacity with a redundancy ratio of 1.8.
4. Checking for resistance of members as individuals gives conservative results. However, checking for the resistance of the whole superstructure using linear and nonlinear buckling gives non-conservative results of their interaction. These results can be deployed for evaluating structural capacity in-situ without necessarily analyzing individual members, as enshrined in Eurocode 3.

Adaptation framework:

The current condition of the bridge was established as good. From the research, a semi-permanent or permanent adoption framework for the Sukumo Bailey Bridge was put forward in consideration of the local needs (use of signages to indicate the capacity) for maintaining the bridge. From the experiment it has revealed its effectiveness notwithstanding fatigue crack evaluation being proposed in the proceeding Chapter 4.

The above-mentioned deductions were drawn from the study providing insight for further recommendations on adoption:

1. The lack of historical data can be supplemented by in situ measurement for ex situ FEM modeling. Consequently, create a numerical model of the bridge for monitoring by updating it with onsite structural data to examine its bearing capacity.
2. A bridge operates as a monolithic structure. Thus, the 3-dimensional structural analysis of the members' interactions is prudent for typical results. As a result, determine the ultimate resistance.
3. For long-span and high bridges, wind, earthquake, and temperature loads should be considered using a case-based approach with reference to local codes and the structure's condition, specifically abutment clearance.
4. The adaptation of the framework can be necessitated through employing local manuals and standards on a case-based reasoning approach.

Chapter 4

Fatigue Crack Inspection using thermographic Techniques.

4.0. Fatigue Crack Inspection Using Static and Transient Thermography for Welding Joints

The objective of this study was to propose using static and transient thermography for fatigue crack inspection and characterization for welded joint(s). Laboratory tests using plate bending fatigue test machine were performed to simulate fatigue cracks, hence the initiated cracks were inspected using an infrared thermal camera implementing Active Thermography (AT) from initiation — N_{toe} to failure — N_{20}. Simultaneously, magnetic, and beach-mark testing was conducted to demonstrate the accuracy and reliability of the detection of fatigue crack using the former. From the results, AT gives both qualitative and quantitative fatigue topology as an alternative fatigue surface crack inspection method. The parameters determined were used for onsite experimentation to determine the reliability of Impact Crack Closure Retrofitting (ICR) method. The method used passive thermography to evaluate for existence through assessing the trough sections for fatigue during pre-ICR and post-ICR conditions/situations. The study used horizontal heating mechanism to determine impedance in heat fluxes hence characterise fatigue during the situations. Passive thermography was established as an NDE approach that can supplement other traditional and conventional NDE approaches with an advantage of evaluating for structural degradation based on fracture mechanics.

4.1. Introduction

Steel bridges consist of members with welded joints. The welded joints are susceptible to fatigue due to local stress concentration during loading, high tensile residual stresses generated after welding, and degradation due to aging [102]. Since fatigue crack propagation causes a reduction of steel bridge's durability, inspecting suspected welded joints where the fatigue cracks initiate is indispensable to avoid its adverse effects. According to Japan Road Association [59], Magnetic Particle Testing (MT) and Penetrant Testing (PT) are the most used inspection approaches. The former requires magnetic particle powder and electricity supply to generate a magnetic field, and the latter needs liquid dye. It would take time to prepare for the electricity supply or dry the liquid dye for MT and PT respectively. Moreover, they are limited in the number of inspection records and evaluation based on fracture mechanics [103]. Thus, an alternative inspection method(s) to inspect suspected welded joint(s) in the actual bridge is desirable, both in-situ and ex-situ.

Thermal Non-Destructive Evaluation (NDE) has often been implemented to inspect defects or imperfections in several fields, such as aircraft [104] and composite materials [105]. The advantage of inspection by thermography is its simple application and relatively rapid assessment. The method measures the thermal contrast between a sound and a defective region. Hence, introducing InfraRed (IR) thermography will enhance and promote efficient inspection on-situ – actual bridge and ex-site – laboratory setup.

The method has been employed passively and actively in evaluating for fatigue cracks on various materials [106]. Both active and passive methods operate either on a transient or static domain in evaluating for imperfections. Sakagami et al. utilized quantum passive thermography to evaluate for fatigue cracks. He used the temperature-gap approach on orthotropic steel deck bridges [4]. The research delved into identifying fatigue and its developments [107]. On the other hand, Bilawal et al. employed pixel-

based frequency to establish the structural health of railroad surfaces using Active Microbolometers thermography [108]. Hence the potential niche to utilize isotherm field data for the characterization of fatigue cracks on welded joints on vertical stiffeners. The approach's novelty is sustainable and diverse due to the field data obtained. Apart from determining the dimension of the defect, one can monitor and establish its propagative nature from initiation to failure.

The objective of this paper was to propose using transient and static, Active-pulse thermography (AT) for fatigue crack inspection and characterization of welded joints. At first, laboratory tests using a plate-bending fatigue test machine were performed. Then, two approaches were used for fatigue crack inspection: a transient approach and a static approach. The former determines the presence of defects, and the latter determines the size of the fatigue and its propagation. Also, MT and Beach-March (BM) tests were performed to characterize crack propagation. After the fatigue test, the fractured surface was observed to demonstrate the accuracy and reliability of fatigue crack detection using the AT approach compared with the fracture surface.

4.2. Theory

The radiant amplitude provides information about the location and size of fatigue crack. The method utilizes effusivity (e) and absorptivity ($\propto$) in a stationary and transient domain, respectively.

$$e = \sqrt{\rho K C_p} \qquad \text{Eq. 4-1}$$

Where ρ - Material density; K - Thermal conductivity; C_p - Heat capacity.

$$\propto = \mathrm{K} / \rho C_p \qquad \text{Eq. 4-2}$$

Fatigue cracks are nucleated V-notches, like plate bending fatigue at N_{toe} (at the initiation stage). Thus, the V-notched characteristic of initiated cracks concentrates more radiant energy than standard surfaces devoid of surface flaws when subjected to radiative pulse energy [109], as shown in Figure 4.1 that has a direct relationship with temperature. In this way, an IR detector can detect the local thermal gradient at an angle (ø) using the Stefan-Boltzmann relation summarized in Equation 4-3. This principle is valid for all Onsager relations where evolution is on the steepest entropy – Newton's Law of cooling [106].

$$\mathrm{W} = \varepsilon \sigma T^4 \qquad \text{Eq. 4-3}$$

Where: σ - Stefan-Boltzmann's constant; T - Temperature; and ε - Emissivity. When the probed surface (welded section) experiences zero radiative transmission, using Kirchhoff's law outlined in Equation 4-4:

$$1 = \begin{cases} \propto + \rho^r \\ \varepsilon^0 + (1 - \varepsilon) \quad \tau = 0 \\ \varepsilon^0 + (1 - \varepsilon)^\alpha \end{cases} \qquad \text{Eq. 4-4}$$

Where: α - Radiant energy absorbed; ρ^r - Radiant energy reflected; τ- Radiant energy transmitted; ɑ - Fatigue crack depth/fatigue crack length in the depth direction and ε – Emissivity.

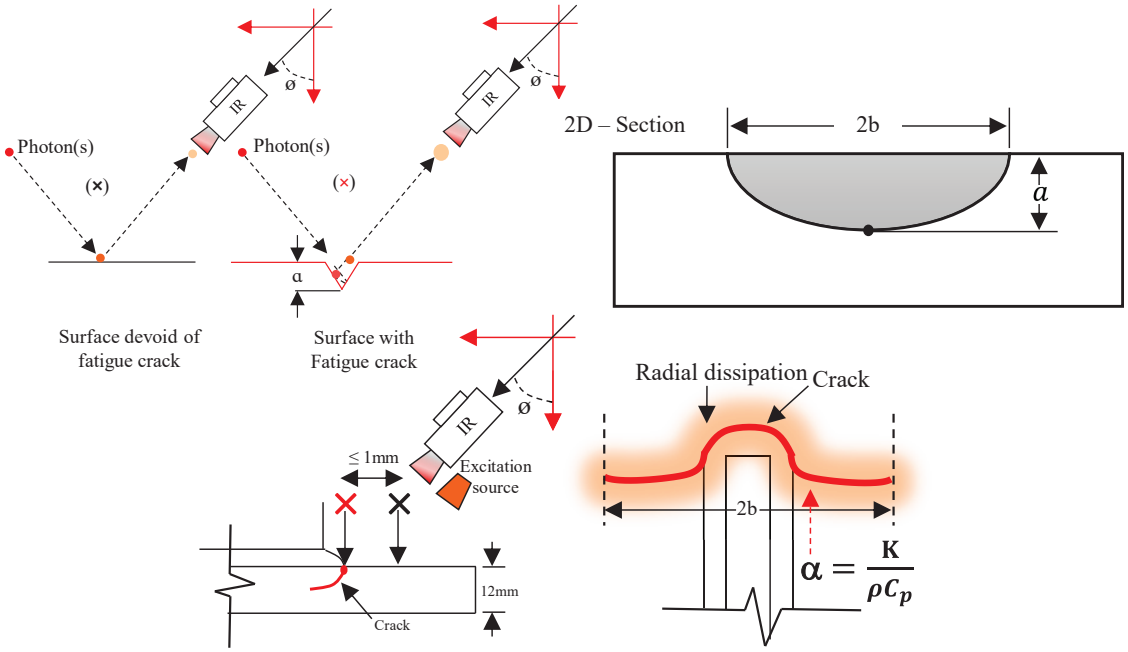

Figure 4.1. Active-Pulse thermography

Where ɑ crack length in the plate depth/thickness direction, b crack length in the in the plate width direction, IR Infrared camera, and ø tilt angle of the central axis of the IR camera.

Assumptions or Hypotheses:

i. Minimal atmospheric interference due to the proximity of the IR camera of 150 - 200 mm.
ii. The suspected region reduces noise for ambient compensation.
iii. The section is infinitely small enough to be illuminated with equal flux on the affected area.
iv. From Kirchhoff's law, α and ε are used interchangeably. That is, they are similar.
v. Emissivity (ε) or absorptivity ($\propto$) increases exponentially (inverse proportionality) with fatigue crack propagation in the depth direction.
vi. Radial dissipation decays away from the fatigue crack region - fatigue crack notch outwards.

Therefore, the surface radiant energy (L) that generates radial dissipation is due to the apparent thermal absorptivity. During fatigue crack propagation, the number of contact regions or surfaces or depth ɑ: {0, 1, 2, …n} mm would be increased:

$$L(\varepsilon_s) = L(\varepsilon_{IR}) - (1 - \varepsilon_p)L \qquad \text{Eq. 4-5}$$

Summarizing Equation 4-5 with 4-4, where the IR radiance $L(\varepsilon_{IR})$ is equated to 1 - blackbody and $\mathcal{E}_\rho$ - reflected radiant energy gives rise to:

$$\varepsilon^0 = 1 - \left(1 - \varepsilon_p\right)^a \quad \text{Eq. 4-6}$$

Fatigue cracks reflect energy depending on their geometry radially outwards from their surface notches, illustrated in Figure 4.1. As a result, this causes a gradual change in the crack's apparent emissivity (emissive energy). Consequently, the property aids in determining surface cracks common in welded dynamic members. Field isotherms or thermograms and transient energy signatures can be used to deduce flaw characteristics due to the local surface temperature variation using the Stefan-Boltzmann law of thermodynamics. Changes in field temperatures can be extracted as field isotherms and video frames to determine the presence of flaws and their evolution quantitatively. The method can be an alternative deployable, noninvasive, reliable, automated, and sustainable screening technique. Hence, its novelty in extracting radiant energy from field isotherm data using the transient and static domain.

4.3. Method

4.3.1. Experimental setup

Fatigue tests were performed using an out-of-plane gusset welded joint specimen(s); JIS-SM490YA Specimen A1 and A2, that were unpainted. The dimensional detail of the specimens is shown in Figure 4.2; a plate deck of 12 mm thick, 300 mm in width, and 700 mm lengthwise; the stiffener was 200 mm by 340 mm, in width and length, respectively. The fatigue test setup is shown in Figure 4.3. Strain gauges were glued on the specimen. The stress range was defined using strain gauges A and B, shown in Figure 4.2, set at an offset of 12 mm transversely from the weld toe condition with offsets of 50 mm across the width and 75 mm longitudinally. Crack initiation and propagation were inspected using copper wire whose diameter is 0.05 mm glued around the weld toe (circuit breaker). Fatigue cracks propagate transversely on the plate to the applied stress direction i.e., plate length direction. The fatigue crack life is defined by the dimension of the crack (2b) denoted by N_{toe}, N_b, N_{10}, and N_{20} according to the study by Yamada et al. [110]. N_{toe} is defined when the cooper wire at the weld toe is broken on crack initiation. N_b denotes the fatigue crack propagates transversely from the weld section to the plate section while N_{10} denotes the fatigue propagation at 10 mm offset from the weld section on either side of the of the test specimen. On the other hand N_{20} denotes fatigue crack propagation at an offset of 20 mm from the weld detail [110].

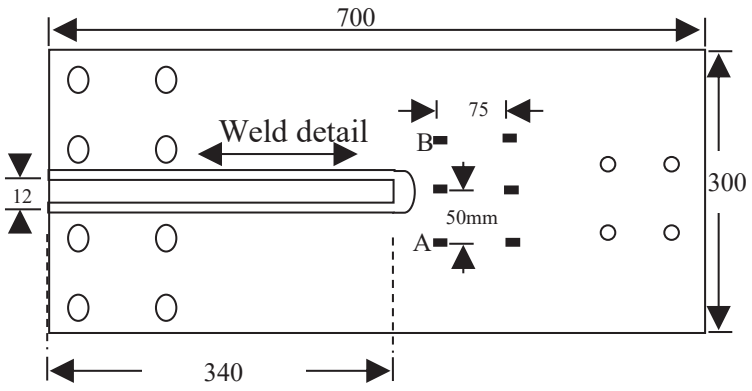

Figure 4.2. Dimensional details (unit: mm)

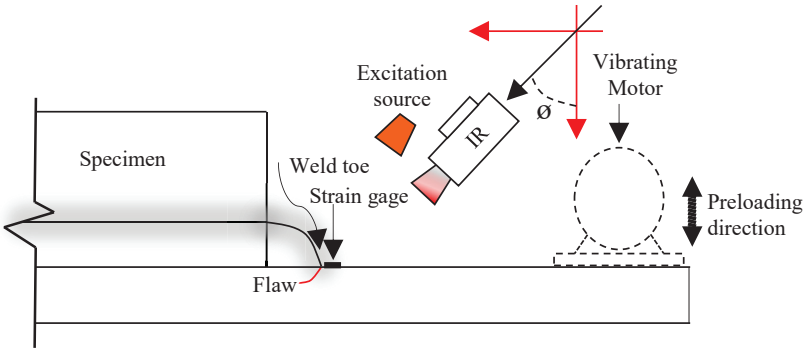

Figure 4.3. Experimental Setup

4.3.2.1. Principle

When surface cracks occur at the weld toe, they act like black bodies and will absorb more energy than the adjacent sections – fatigue crack free sections. Due to temperature contrast, a thermal gradient is realized that an IR camera can detect. The energy absorbed or emitted is determined and projected in Equation 4-7.

$$\propto^{0} = 1 - \left(1 - \propto_{\rho}\right)^{a} \qquad \text{Eq. 4-7}$$

where, $\propto^{0}$ is the apparent emissivity, absorptivity, or radiant energy, $\propto_{\rho}$ surface or specimen or steel emissivity of approximately 0.8, and a fatigue crack dimension in depth direction taken as the number of reflections or contacts in the cavity [111].

The emissivity of the crack will gradually grow to about 1 - assuming a blackbody cavity. The emissive or radiant energy depends on the number of reflections or contacts a (depth) experienced. Therefore, it gradually increases the amount of dissipated energy exponentially while emissivity (ε) is directly proportional to the radiant energy, as shown in Figure 4.4, which is also related to Equation 4-3 – Stefan Boltzmann Equation.

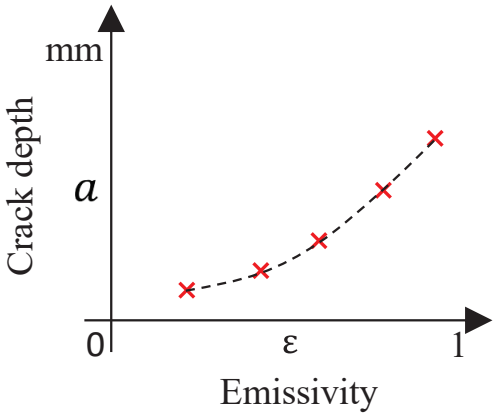

Figure 4.4. Relationship between crack depth and emissivity

4.3.2.2. Conditions for IR approach

An IR camera was used for fatigue crack inspection with a halogen pulse excitation source of 500 - 1000W for 0.5 - 1.0 second. It has a spatial resolution of 0.1 to 0.2 mm/pixel; a detector of 640 × 480 pixels; a spectral range of 8 to 14 μm; measurement

temperature range of – 40 ℃ to 650 ℃; temperature accuracy of 1℃. Fatigue detection was performed 150 to 200 mm from the suspected region to achieve a spatial resolution of 0.2 mm/pixel, as shown in Figure 4.3. The spatial resolution was determined by a manual and pixel calibration from the first experiment, presented in Table 4.1. The IR camera detection was done at all stages from N_{toe} to N_{20}, where surface temperatures were observed immediately after excitation of the specimen, and surface features (crack tips, radiance, and dimension) were extracted using the field isotherm approach illustrated in Figure 4.5. Fatigue details were populated by scan lines normal to the notch at intervals of 2.5 mm laterally in the direction of the fatigue span propagation. Data was obtained before preloading from each regime N_{toe} to N_{20} using an IR software. Surface crack dimensions were extracted along the plate width direction like the MT method.

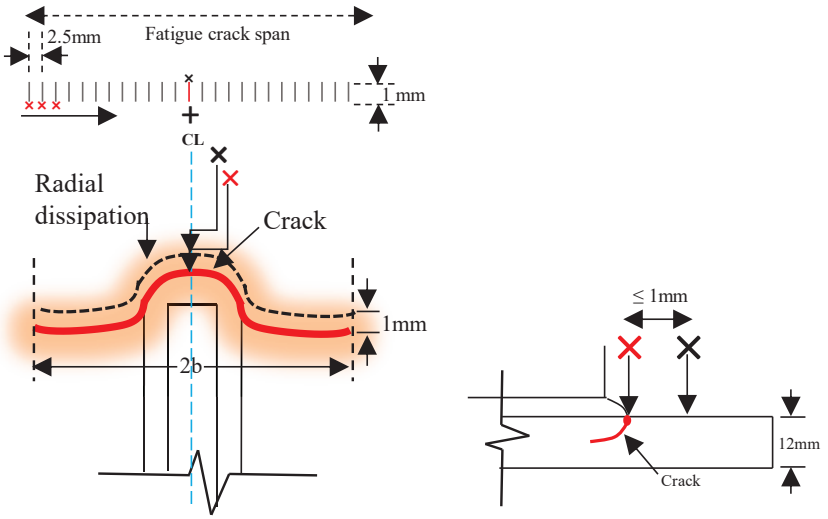

Figure 4.5. Field-isotherm data extraction scheme

Table 4.1. IR Camera specifications custom for the experiment

S/No.	Parameter	Value
1.	Temperature difference	0 - 10℃
2.	H-FOV & V-FOV	25°
3.	Observation Distance	150 – 200 mm
4.	Tilt	15 – 60°
5.	Spatial Resolution	0.1 – 0.2 mm/Pixel
6.	Thermal conductivity	3.60E-02 W/mm/℃
7.	Specific heat	4.90E+02 J/Kg/℃
8.	Density	7.84E-06 Kg/mm^3

4.3.2.3. Transient thermography

The approach entailed observing imperfections in a preselected time domain — 30 seconds. A pulse of energy from an excitation source of 500-1000 W Halogen lamp was directed to the suspected section, placed 150-200 mm away from a base plate. The distance established ensured uniform illumination of the area. The pulse lasted less than 1.0 seconds (s), confirming that the observation time exceeded the exposure time. Welded sections are most vulnerable to fatigue cracks as a result [112], selected pixels on the sound section — plate section (×) and suspected fatigue crack section (×) were observed

for their cooling behaviour for a maximum of 30 seconds at a frame rate of 2.5 Hz,, as shown in Figure 4.5. The parameters established in Table 4.1 were used during the current and preceding experiments.

The pulses were in the order of 2.0 ms from the halogen heat source. As a result, the frames were fitted onto a cooling curve that assumed the newtons decay spectral radiative curve conveyed in Equation 4-8.

$$T_n = \Delta T E^{-Kt} + T_\alpha \qquad \text{Eq. 4-8}$$

Where, T_n Apparent Temperature, ΔT Temperature change, T_α Ambient Temperature, t Time in seconds and K Thermal conductivity.

4.3.2.4. Static thermography

The presence of fatigue crack(s) was established from transient thermography prompting static thermography. Static thermography demands the acquisition of thermographic images in a time-independent state. That is, there was no reliance on time but overreliance on excitation. At least five static thermographic photos were taken immediately after each excitation phase. A minimum of 5 images were captured for the suspected sections using similar parameters as the transient approach listed in Table 4.1. Emittance or radiance data were extracted laterally on the fatigue crack section at intervals of 2.5 mm.

Temperature variation gives rise to variation in thermal contrast making fatigue sections distinct, giving rise to Equation 4-9. Thus:

$$C_t = \frac{\Delta T}{T_a} \qquad \text{Eq. 4-9}$$

Whereas C_t Constant, ΔT Temperature change and T_a Ambient or surface temperature.

4.4. Results and Discussion

The initial experiment established the parameters to be employed during the preceding experiments. However, it was noted that transient thermography should be done before static thermography for fatigue crack evaluation. It essentially verifies the presence of fatigue crack(s), followed by static thermography. Hence, specimen A1 was explicitly static thermography. On the other hand, specimen A2 had both transient and static thermography.

4.4.1. Transient approach for fatigue crack inspection

Welded sections tend to suffer from local stress concentration due to cyclic loading and intrinsic weld defects. The issue makes them vulnerable to fatigue crack(s). The degradation of steel structures is attributed to mostly welded joints. Consequently, the temperature change as a function of time was monitored for the suspected welded section [112]. Figure 4.6 shows the probing for fatigue in the transient domain. A section 1.0 mm offset, normal and horizontal to the width section of the stiffener (×), was also observed and perceived as the non-defective section — section that has no fatigue crack, portrayed in Figure 4.5. The thermal diffusivity (rate of conductivity) was high on the 1.0 mm offset

area due to the lack of development of a thermal gradient effect [4]. Further, effusivity was lower in the sound area — plate section (×) compared to the suspected section (×). Fatigue crack sections (×) forms a local hot zone where the surface temperature is higher than the surrounding causing a thermal gradient [113]. The section is arbitrary because initiation mainly occurs along the curvature of the welded section corresponding to N_{toe}. The effect positively determined fatigue, corresponding to MT measurements of the fatigue crack of approximately 24.16 mm (later shown as Figure 4.7 (b)). Fatigue sections have a slower heat decay rate due to increasing absorptivity — high effusivity and longer diffusivity rates. Bundles of radiant energy injected from the energy pulse concentrate in the area result in high Emittance [109]. The section acts like a specular object reflecting the concentrated radiant energy, as revealed in Figure 4.1. As a result, it confirms that imperfections can be localized through sequencing images or frames — heat decay.

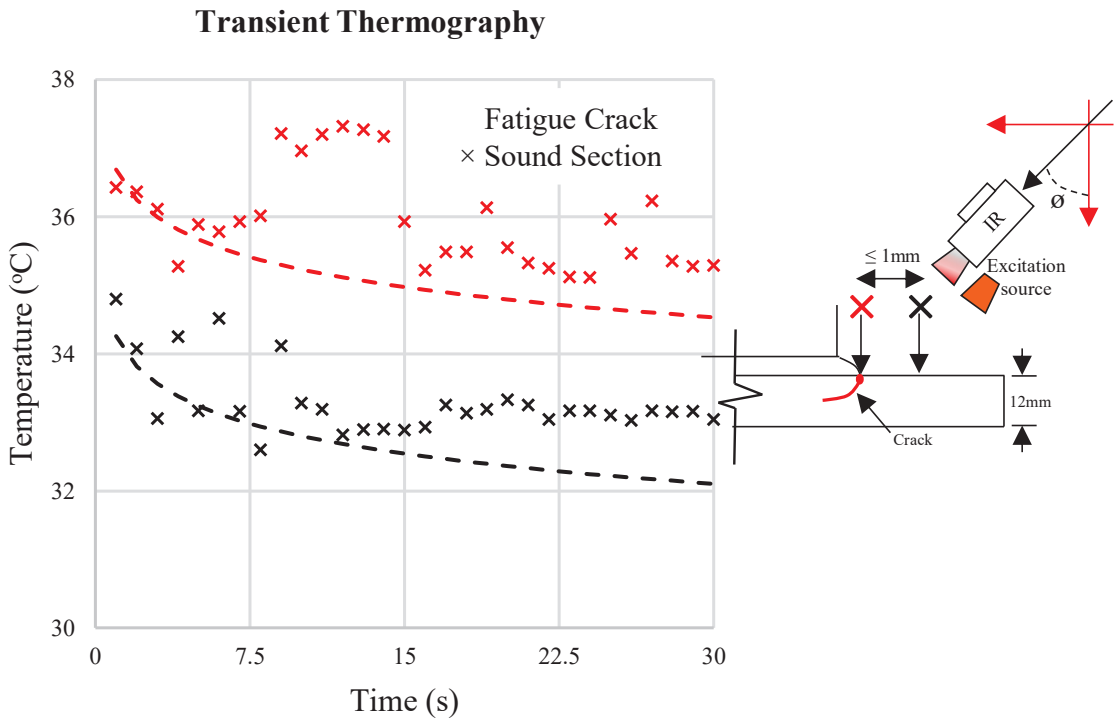

Figure 4.6. Transient thermography

4.4.2. Static approach for fatigue crack inspection

Figure 4.7. presents the initial radiance and thermal condition prior to fatigue crack simulation i.e., loading. The situation indicates approximately even thermal gradient along the probed section an indication that there is no fatigue on fitting the 4-degree polynomial along the radiance. However, due to inclusions at approximately 37.5mm and non-uniform excitation/illumination [114,115] and influence the angle of excitation [113] on all the sections of the specimen sections 0 – 50 mm tend to have lower radiance compared to the corresponding sections. Uniform excitation is recommended for probing of fatigue hence determine the thermal diffusion around the section. On the other hand, Figure 4.8.(a), 4.8.(b), 4.8.(c), and 4.8.(d) show field isotherm data and radiance amplitude (Radiance $\rightarrow$ $(W = \varepsilon\sigma\pi T^4)$) against calibrated pixels (for a consistent probing distance of approximately 150-200 mm with the axis of the IR camera between 15°-60°

achieves a spatial resolution of 2mm/pixel) to dimension taken from the crack size of N_{toe} to N_{20}. From equation 4-3 Temperature is directly proportional to radiance thus similarity in their scatter plots presented in Figure 4.7a – 4.7d. Fatigue cracks at welded sections propagate laterally in the plate width direction to the applied stress direction [112]. It assumes the curvature of the weld fillet section (along the weld line) followed by a normal to the longitudinal section from the welded detail. A 4-degree polynomial is fitted to the mean of the radiance extracted, illustrated in Figures 4.8a to 4.8d, to capture the approximate crack propagation. Therefore, the outcome demonstrates a fatigue crack section of 25 mm having a good agreement with the weld lining curvature dimension of the specimens' welded section illustrated in Figure 4.2. Similarly, this corresponds with MT results presented in figure 4.8 specimen A1 and A2. Fatigue crack radiance amplitude and contrast decreases from the crack notch towards the surface crack tips. Because temperature is a transient quantity, the static images would exhibit variation in temperature scales, however, resolving for fatigue cracks is detected through thermal gradient, and notches and crack tips through variation of the amplitude indicated by individual static images per regime. The varying thermal gradient is exhibited from figures 4.7(a) as N_{toe} from approximately 7.25-32.25 mm; 4.7.(b) as N_b from 10.76-43.43.24 mm; 4.7.(c) as N_{10} from 8.48-59.36 mm and 4.7.(c) as N_{10} from 2.30-73.01 mm. Therefore, fatigue crack notch and tip can be determined by employing field isotherm information. It can be concluded that increased thermal absorption directly affects the fatigue crack contrast suitable for the IR camera to discern cracked and sound sections [113]. Sections near the fatigue notches show a high amplitude because of their perceived increase in width and depth. The elliptical nature of weld-toe fatigue exponentially reduces in depth laterally in the plate depth direction [116,117].

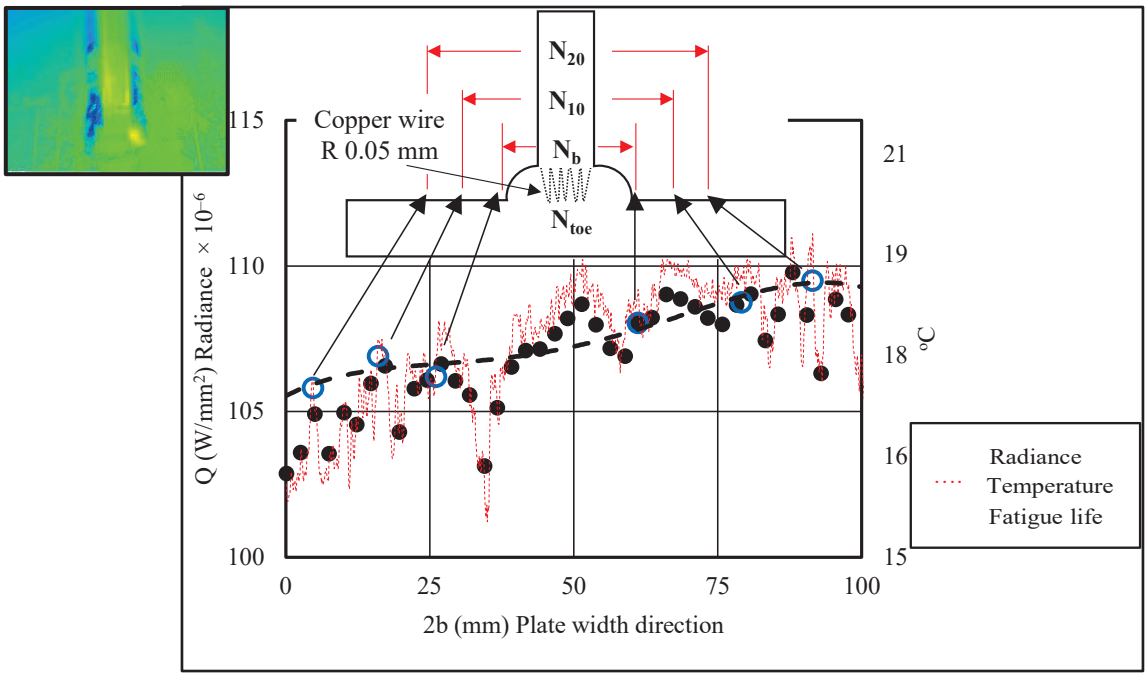

Figure 4.7. Initial conditions

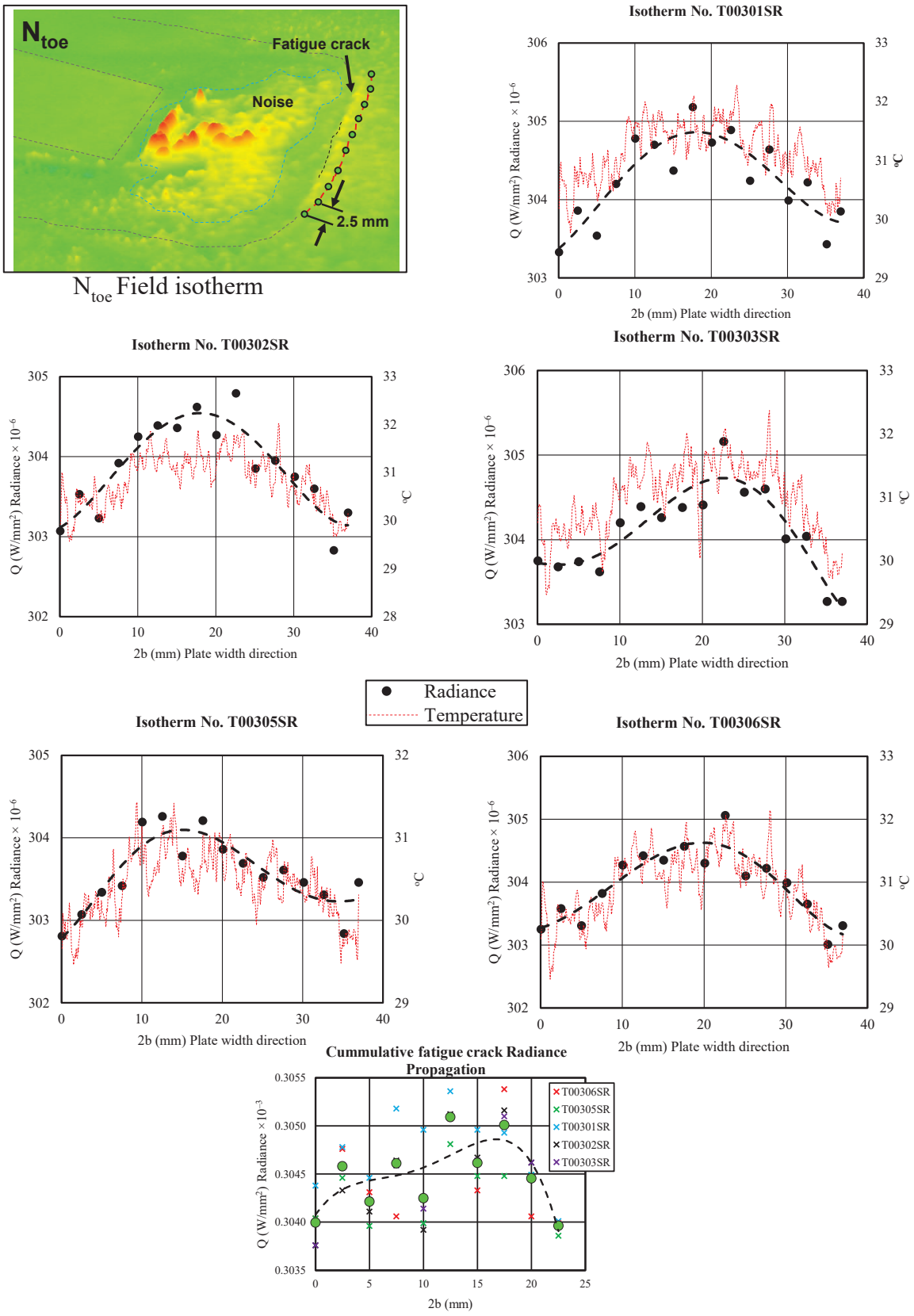

Figure 4.8. (a) Radiance Amplitude N_{toe}

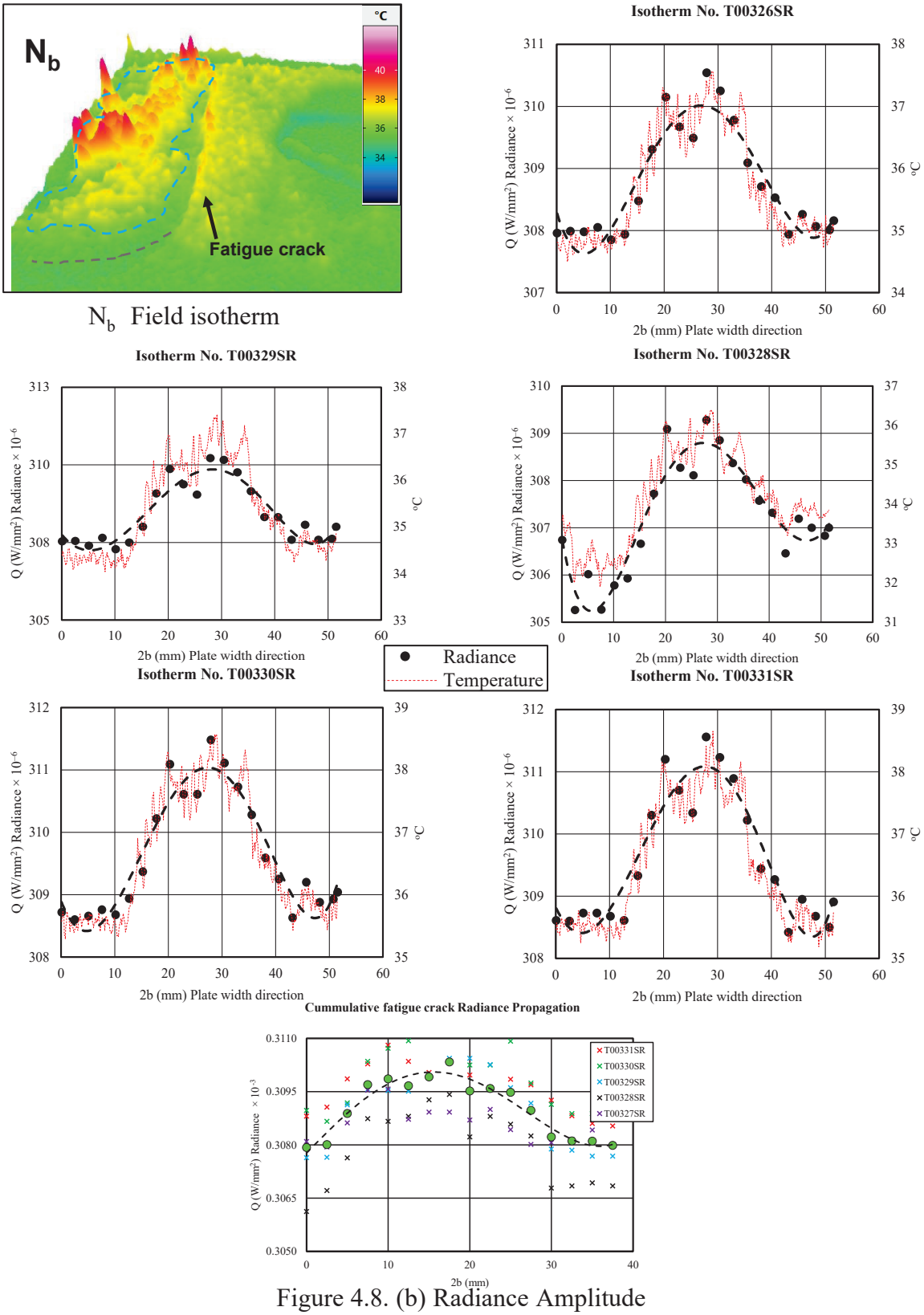

Figure 4.8. (b) Radiance Amplitude

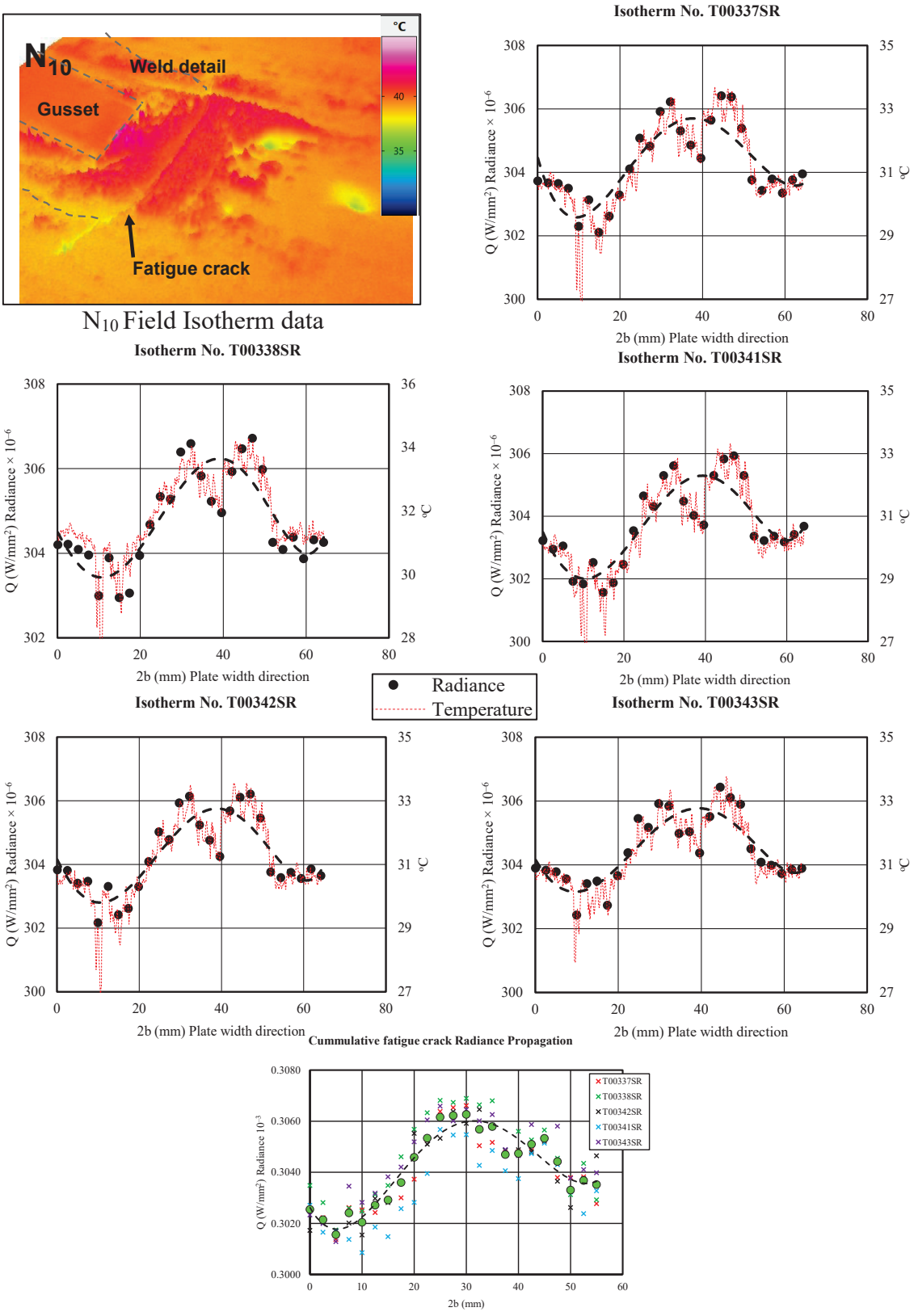

Figure 4.8. (c). Radiance Amplitude N_{10}

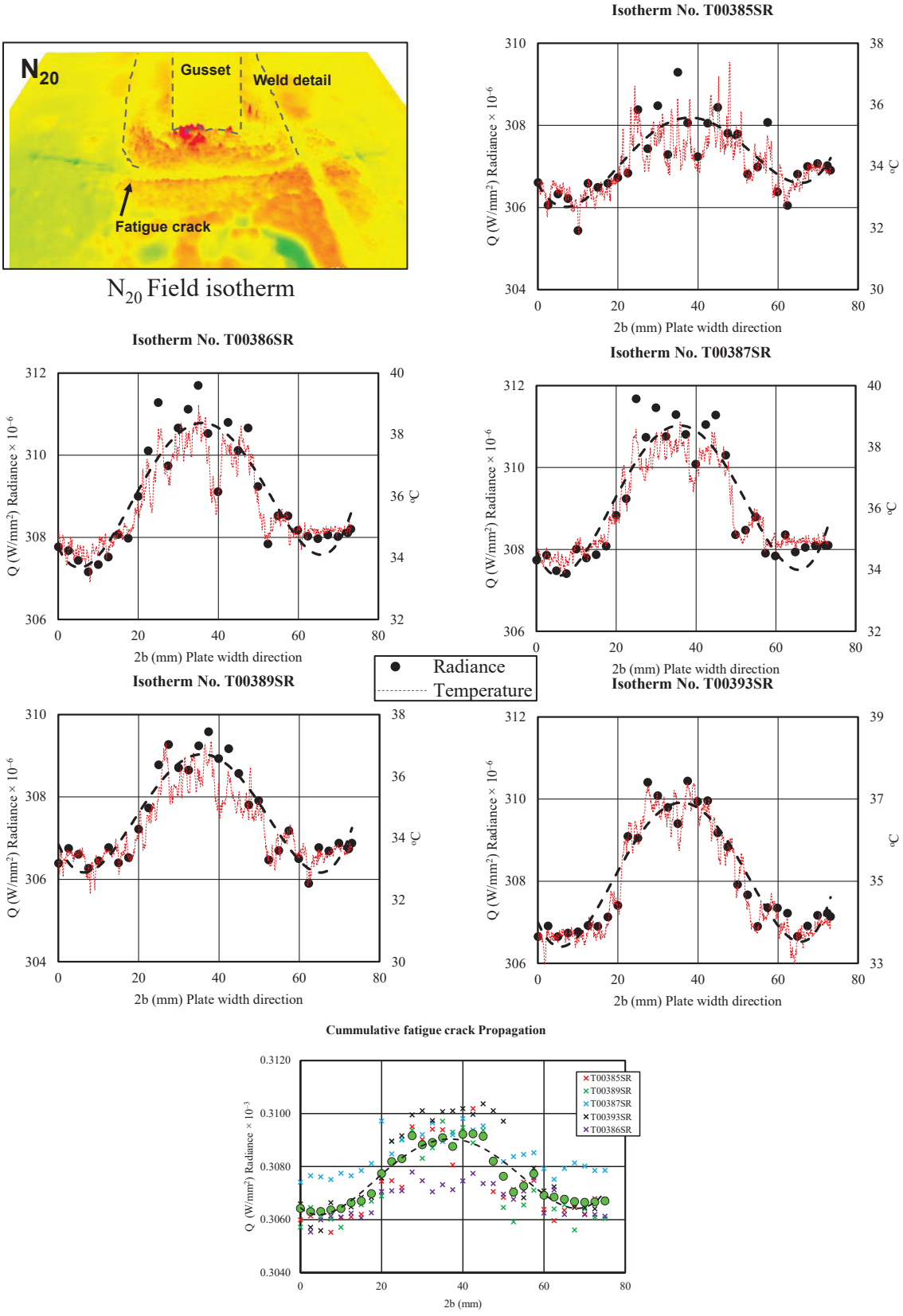

Figure 4.8. (d). Radiance Amplitude N_{20}

As such, the radiance amplitude along the fatigue path declines towards surface crack tips and increases at the notches governed by the fatigue propagation path along the depth direction, as shown in Figure 4.8. Crack tips also significantly show the actual dimension of the surface crack both laterally and along the crack path. On the other hand, the crack notch's increase in radiance indicated fatigue propagation in the depth and width direction (from approximately 0.305×10^{-3} W/mm^2 to 0.310×10^{-3} W/mm^2). Fatigue cracks absorb energy that concentrates at the V-groove and emits energy related to Newton's law of cooling for radiative energy and Fourier's Law of thermal conductivity [108].

Figures 4.9a and b from Specimen A1 and A2 show the results of fatigue crack inspection using an IR camera. Specimen A1 was used to establish the optimum parameters for fatigue evaluation, elucidated in Table 4.1. Nevertheless, the results obtained were harmonious with BM results. From the outcome, the IR camera captured all weld-toe cracks from $N_{toe} - N_{20}$. The thermal field isotherm along the weld-toe section indicates a sharp gradient between the flawed and flawless regions at N_{toe} during fatigue initiation. A median filter enhanced the sharp discontinuities, making the edges more pronounced - edge detection. Edge detection relays pixels with high radiant energy, indicating the boundary between fatigue and non-defective regions. Radiant energy data extracted at intervals of 2.5 mm was more effective in determining fatigue crack propagation along the plate and weld section rather than binary images due to the diversity of functions of the data, as shown in Figure 4.5. The presence of fatigue at the welded section results in local temperature variations due to varying thermal properties, increasing its thermal contrast (C_t) with an increase in fatigue crack in the depth direction, demonstrated in Equation 4.9 and Figure 4.9.

Figure 4.10 and Table 4.2 indicates a rapid temperature rise by the specimens' sparsely distributed hotspots. The presence of oxides and inclusions merely has a higher thermal absorptivity. The inclusions create outliers and noise on the field isotherm. The propagation of the crack meant more energy would enter the cavity, increasing its thermal characteristics [109], summarized in Equations 4.1 and 4.6. It was noted that an increase in the crack size and depth increased the number of reflections within the cavity. The thermal parameters of the affected areas increased to approximately a black body or grey body ($\varepsilon \approx 1$), resulting in less reflective thermal contrast of the crack. The former was due to absorptivity of energy; hence the least amount of radiant energy was reflected. Accordingly, the propagation of fatigue from N_{toe}-N_{20} meant a corresponding increase in crack width. Absorbed radiant energy monotonically increased from $N_{toe,}$ as shown in Figure 4.10 and as descripted in Table 4.2 as the mean emittance across 5 static thermal images.

Table 4.2. Mean Emittance

Regime	**α (mm)**	**Emittance/Radiance (W/mm^2)**					**$\dot{x}$**
		E_1	**E_2**	**E_3**	**E_4**	**E_5**	
N_{toe}	3.7337	0.7431	0.7429	0.7439	0.7425	0.7428	0.743
N_b	6.7342	0.9157	0.9154	0.9151	0.9153	0.9146	0.915
N_{10}	8.1138	0.9488	0.9487	0.9484	0.9486	0.9486	0.948
N_{20}	8.9865	0.9638	0.9639	0.9649	0.9644	0.9641	0.964

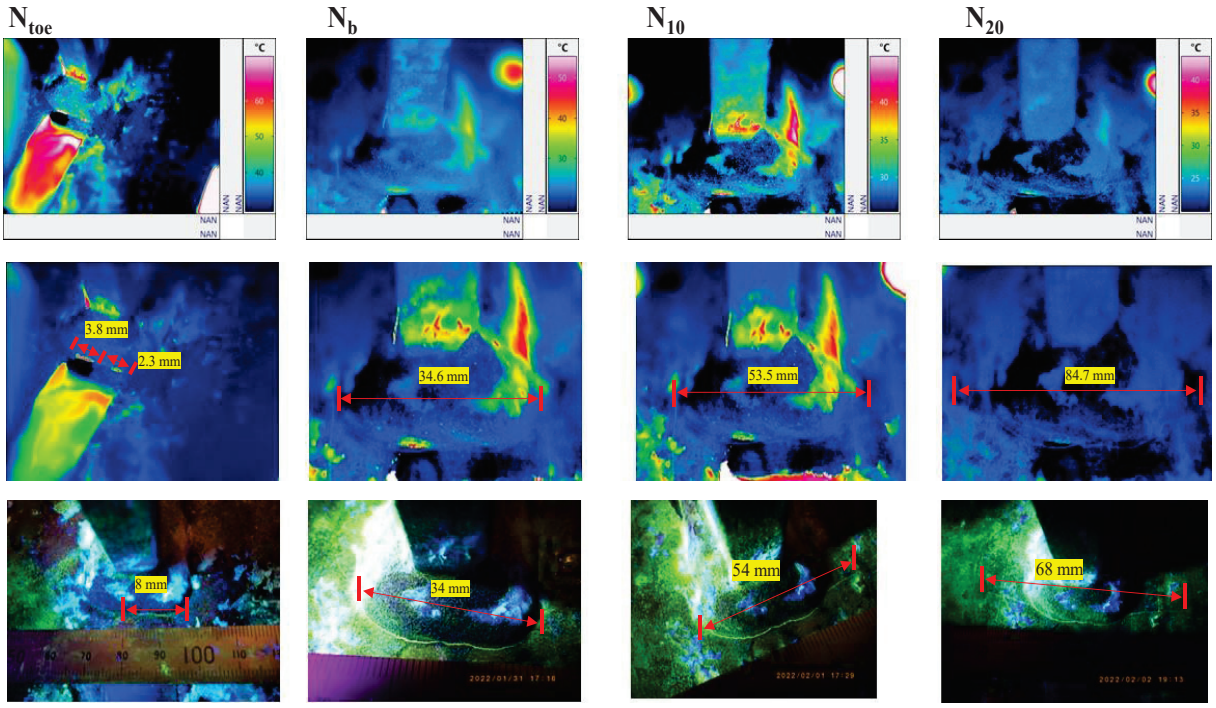

(a) Specimen A1

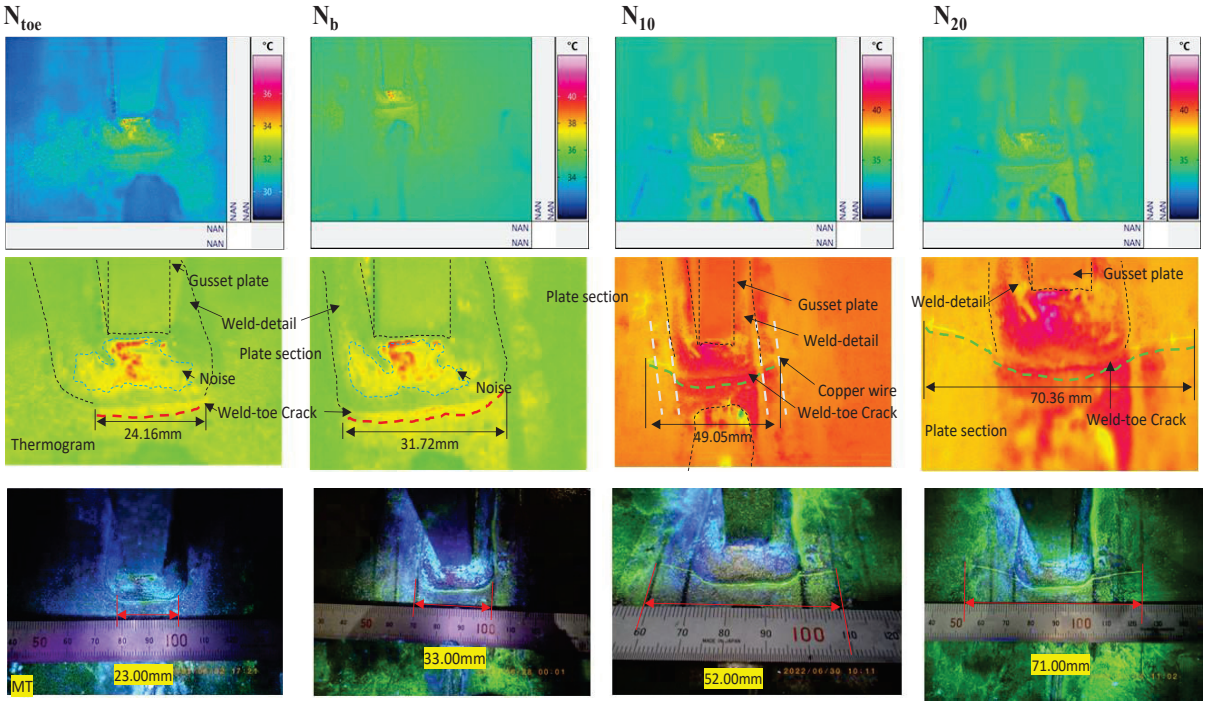

(b) Specimen A2

Figure 4.9. Fatigue Crack inspection results ITT vs. MT

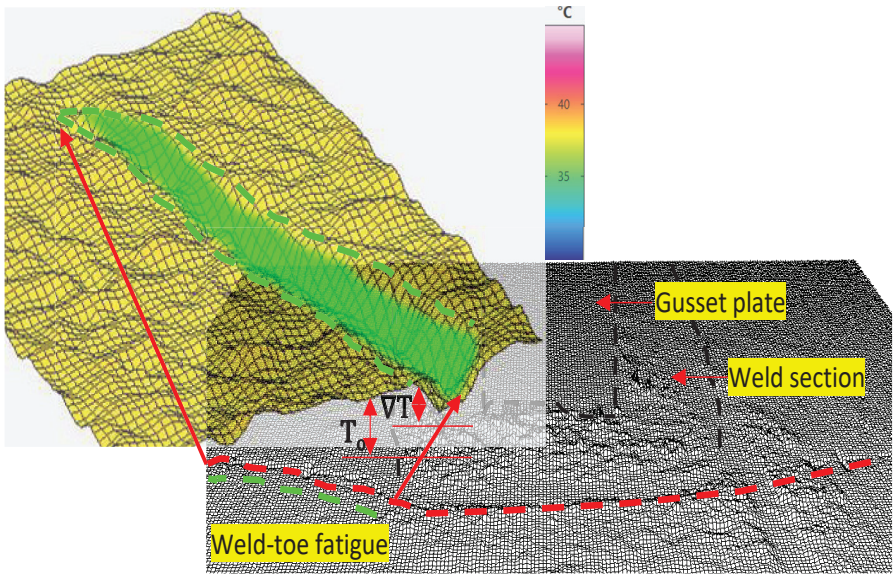

Figure 4.10. Thermal contrast around the crack tip

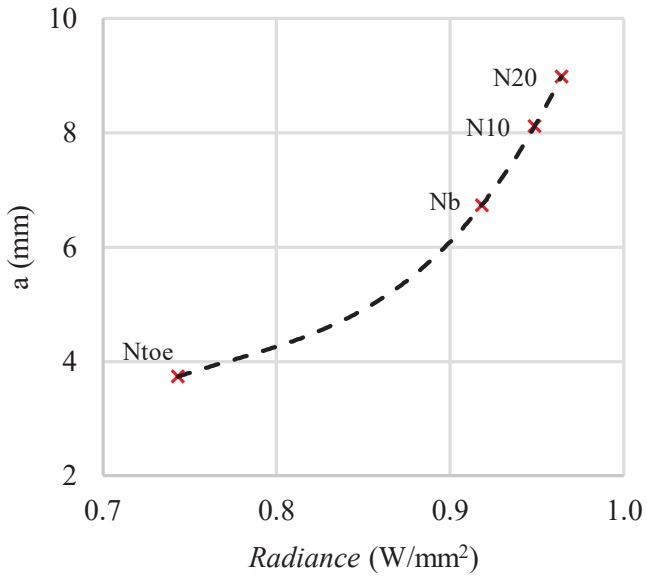

Figure 4.11. Decaying radiance with depth

Cracks with considerable depths and width have high absorption and thermal contrast from N_{toe} - 0.743; N_b - 0.918; N_{10} - 0.949 and N_{20} - 0.964 × 10^{-3} W/mm^2. Most of the excitation energy is absorbed rather than reflected, resulting in higher radial dissipation around the fatigued section due to thermal diffusivity, see Equations 4.2 to 4.6. Therefore, from the outcome, the apparent radiant energy and change in emissivity can be estimated from the surface radiant energy recorded from Equations 4.4 to 4.6. It indicates the exponential characteristics of emissivity derived from emitted or radiance energy (W) with fatigue propagation in the plate depth direction. The estimate assumes fatigue

initiation develops as a v-groove from the plate surface and reflections occur at each regime 'α' as the contact surface is extracted from the fracture surface [109].

Radiance or Emittance is drawn from the direct proportionality between radiant energy and emissivity. The relationship is drawn from the Stefan-Boltzmann law synopsized in Equation 4.2. The direct proportionality of W to ε is interchangeably used due to variability in thermal properties.

Conversely, the absorptivity was reduced with small cracks owing to their small spatial cavity. The geometry of the section constrained their detectability. The radial temperature isotherm fields on the affected areas relayed low emissive power. However, high reflective power from the excitation pulse facilitated the detection of Infra-Red Thermography readout. Moreover, since small surface cracks are easier to illuminate uniformly, this was reason enough for the probability of detection. The dimensional accuracy corresponded with BM testing from Figures 4.12 and 4.13.

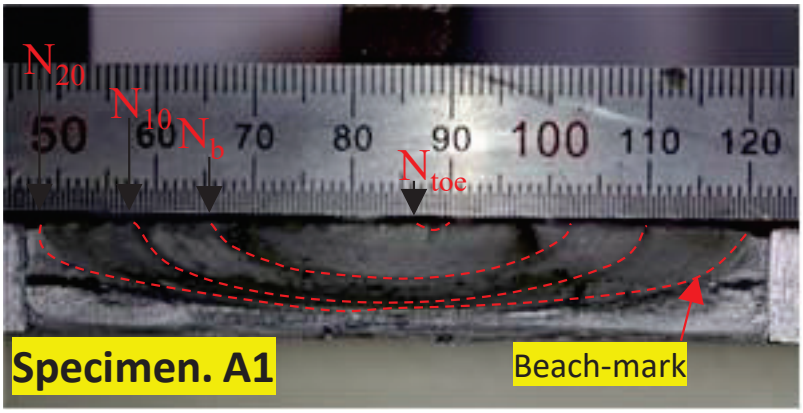

(a) Specimen A1

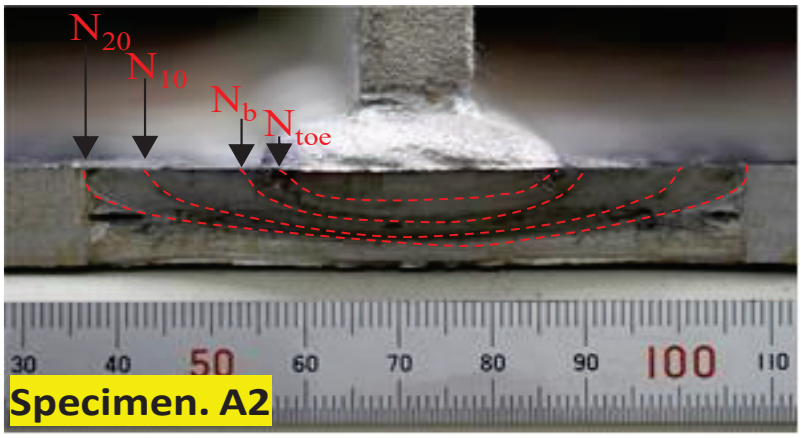

(b) Specimen A2

Figure 4.12. Beach mark

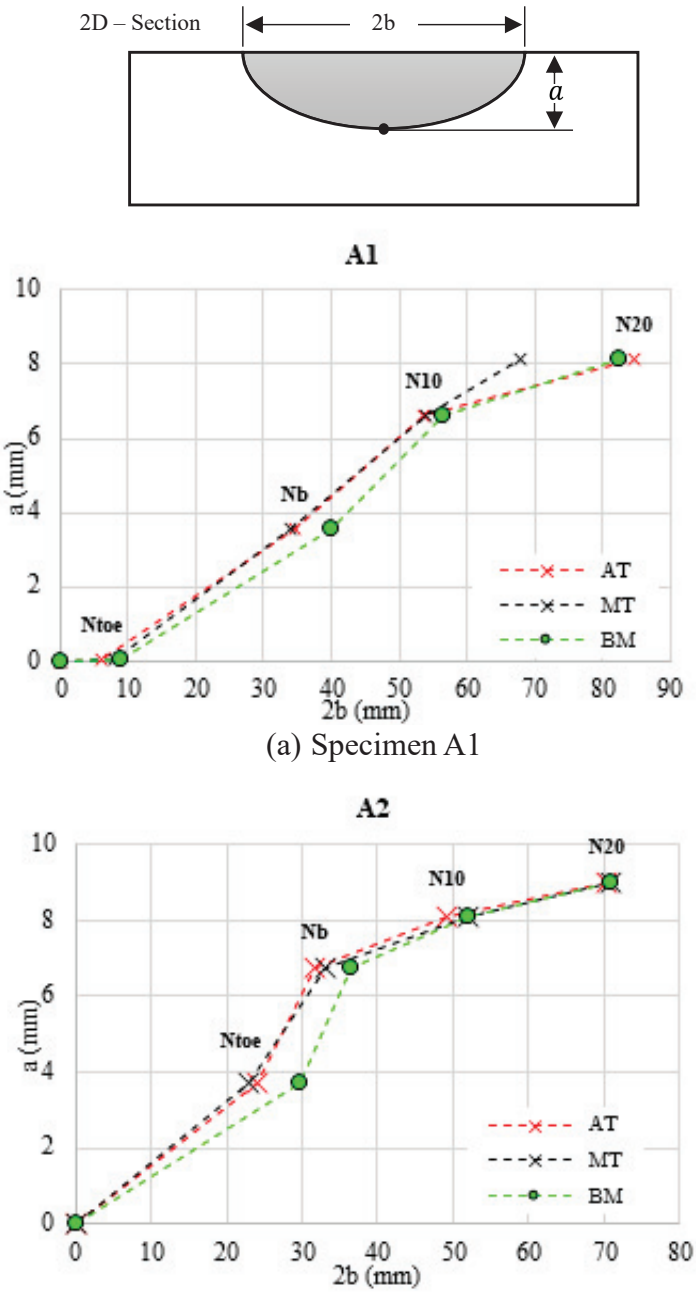

(a) Specimen A1

(b) Specimen A2

Figure 4.13. Comparison of detection of fatigue crack dimension using AT, MT, and BM

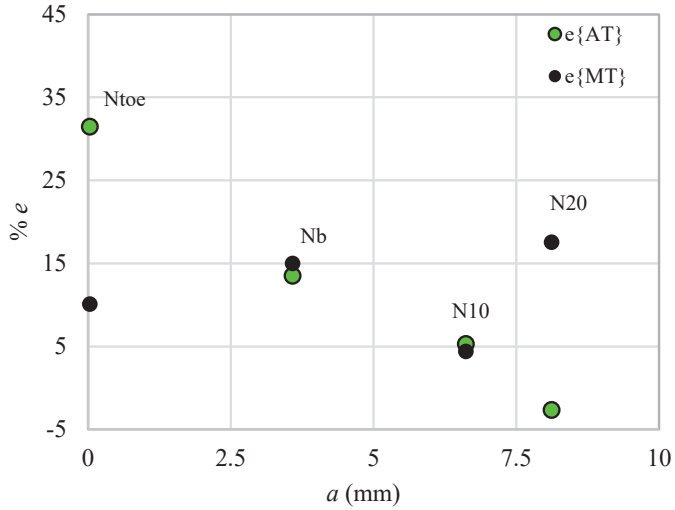

(a) Specimen A1

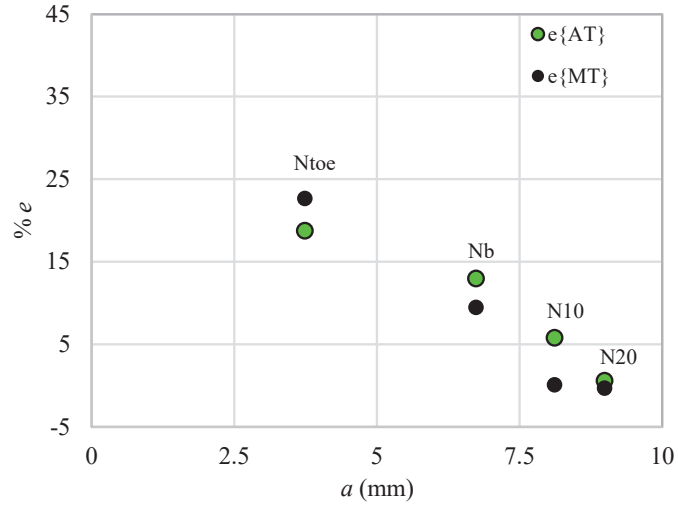

(b) Specimen A2

Figure 4.14. Absolute error between AT and MT

The absolute Error Term = 100% × [1- (Active Thermography measurement ÷ BM dimension)]. The percentage error of both IR and MT increased with fatigue depth 'α', probably due to the orientation of the fatigue path from the weld section to the plate section N_{toe} - N_b and N_{10} - N_{20}. However, AT posted consistency in percentage error in specimens A1 and A2, contrary to MT, which seemed erratic in specimen A1. Moreover, the absolute error relayed some similarities in Figure 4.13. Additionally, in comparison with MT, AT has inherent random errors with specimen A1 dipping and specimen A2 rising at N_{toe} and dipping at 7.6 mm and 8.11 mm in A1 and A2, respectively, represented in Figure 4.13. As a result, accuracy is assured from the approach with limited systematic errors.

Based on the evaluation, the dimensional measure using MT does not factor in the unevenness of crack propagation that can be addressed by Active thermography. AT

provides complete field information, though restricted by spatial and thermal resolution. While thermography indicates two initiation points of fatigue, like BM testing fracture surface and MT relays a continuous crack propagation on the surface at N_{toe} result in specimen A1. From N_{toe} to N_b, the propagation of the crack was along the weld details and propagated transversely on reaching the deck plate. Therefore, static thermography can accurately characterize fatigue propagation for rapid field screening revealed in specimens A1 and A2 using field isotherms.

4.4.3. Resolving for Depth

Subsurface defects are visible only within their diffusion length.

$$\mu = \sqrt{\frac{\propto}{(\pi f)}} \qquad \text{Eq. 4-10}$$

Where: μ thermal diffusion length, f frequency and ∝ absorptivity or diffusivity, discussed in Equation 4.2.

From the experiment, μ achieves a maximum of 1.09 mm using predefined values from Table 4.1, with frequency of 2.5 Hz, Thermal Conductivity of 3.60E-02 W/mm/ºC; Density of 7.84E-06 Kg/mm^3 and Heat flux of 2.39E-03 W/mm3. Additionally, it is confined by the crack opening width on the plate surface section by width to depth (w/α) ratio with an optimal spatial resolution of 0.2 mm/pixel. Where the width refers to the width of the tensile crack opening around the most prominent notch section, assuming mode one crack displacement. The depth resolution diminishes with the fatigue width (w), as shown in Figure 4.14. A crack width of more than 0.2 mm can have a resolved depth probe of approximately 1.5 mm. As a result, painted surfaces are limited depending on the coat thickness and color of the paint. Black paint absorbs and emits highly and is often employed to make fatigue more evident in the aeronautical industry. From literature, the probing is restricted to a maximum of 3.2 mm on a 1 mm crack width. Consequently, with the increase in crack width and decrease in modulating frequency for lock-in thermography [118], the probing depth resolution increases [119,120]. As such, it does not replicate weld toe cracks that have distinctive narrow widths during initiation at Ntoe, and as a rule of thumb, the maximum probing depth of Active Flash thermography is 1.5 - 2 mm.

Table 4.3. Width to Fatigue crack depth ratio

Regime	α (mm)	W/α Ratio		
		0.3 mm	0.2 mm	0.1 mm
N_{toe}	1	0.300	0.200	0.100
	2	0.150	0.100	0.050
	3	0.100	0.067	0.033
	4	0.075	0.050	0.025
N_b	5	0.060	0.040	0.020
	6	0.050	0.033	0.017
	7	0.043	0.029	0.014
N_{10}	8	0.038	0.025	0.013
N_{20}	9	0.033	0.022	0.011

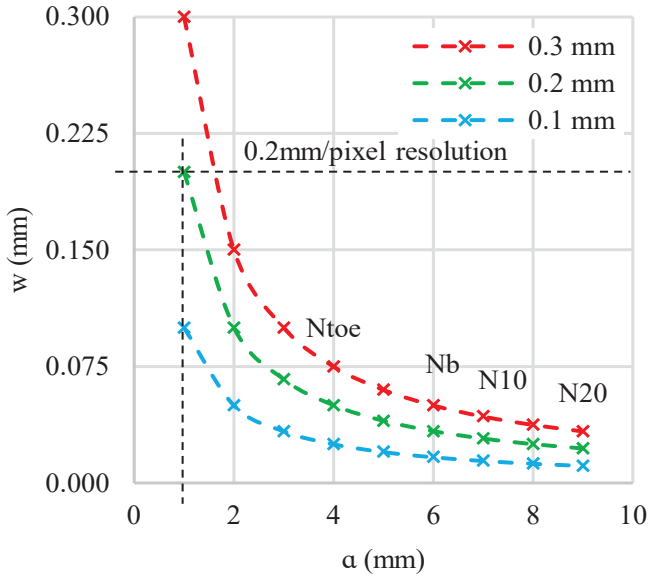

Figure 4.15. Width to depth ratio with 0.1 mm ≥ Spatial Resolution ≤ 0.3 mm

4.5. Fatigue Crack Inspection for ICR Treated Section of an OSD section Using Passive Thermography

4.5.1. Introduction

Structural degradation of Orthotropic Steel Decks (OSD) is mainly attributed to susceptibility of welded sections to fatigue [4,121]. The issue requires an immediate remedy to lessen the imminent threat it would pose if left unattended. The OSD was adopted due to the ease in fabrication, availability of material, high load bearing capacity, and ability to achieve longer spans due to its light compressive dead load. However, the structure is composed of numerous welded elements imposing complex stress distribution and ranges due to the dynamic effect of vehicular motion. The effect results in development of Root-deck, toe-deck, weld root and toe-trough fatigue cracks that at times propagate to the trough section as presented in Figure 3.18a-b [122]. As a result, the predicted design fatigue life of the structure is affected.

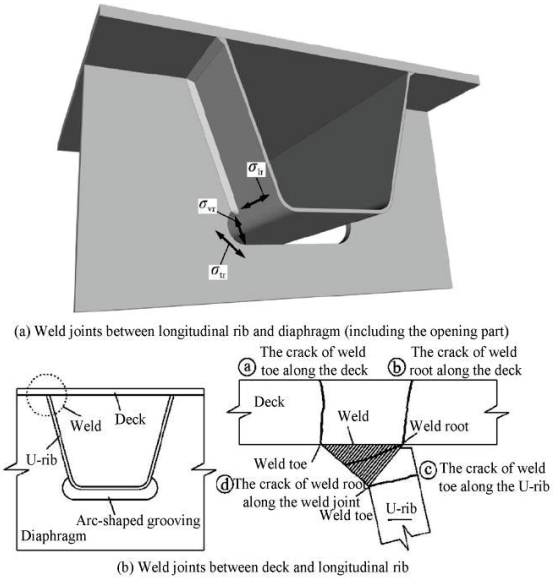

Figure 4.16. Typical Fatigue on an OSD (Zhongguo et al, 2017)

There are several post-weld treatments techniques based on change in the residual stress of the affected section such as peening. Alternatively, some tend to improve the section's topography that is improving the fatigue strength [123] – grinding, ultra-sonic impact treatment and tungsten inert gas-dressing [124]. Fatigue strength improvement is as a result of compressive residual stress [123]. Thus, the methods are deployed to enhance the fatigue strength of welded steel structures and extend the service lives of components. Impact Crack Closure Technique (ICR) was established to be simple, economical, took a few minutes to admit and required no traffic restrictions. The method introduces plastic properties (introduce residual stresses) near the crack section reducing the crack growth rates$(\mathrm{d}a/\mathrm{d}N)$ to 0.34 times accounting for approximately the power of three of the stress intensity factor (ΔK) yielding to fatigue life increase [125]. However, evaluating for reliability of the method based on fracture mechanics is vague save for engaging penetrant testing illustrated in Figure 4.16 and magnetic testing. Under such circumstances, the repercussions in case of ineffective treatment might be detrimental. Therefore, it is necessary to grasp the surface crack opening and closing phenomena to evaluate for the efficacy of the method.

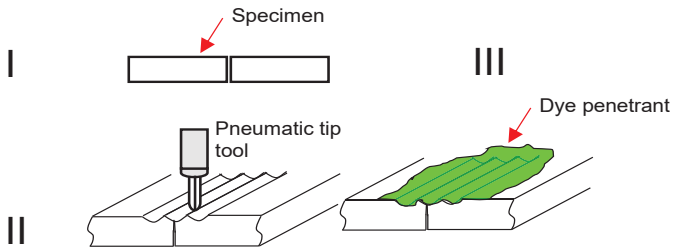

Figure 4.17. Penetrant Testing of ICR treated section.

In this study the actual surface crack opening and closing phenomenon is studied through an onsite field investigation on an in-service orthotropic steel deck bridge. The deflected fatigue crack to the trough rib from toe-trough fatigue cracks are ICR treated

were examined before and after treatment. The phenomenon is studied by passively employing remote Infra-red Thermal non-destructive probing for heat flux diffusion. Thus, the experiment will propose using passive thermography for inspection of the reliability of ICR treatment on OSD trough section.

4.6. Theory

4.6.1. Heat Flux Diffusion

Infrared thermal microbolometers obtain thermal information using the Stefan-Boltzmann's law ($W = Q/A = \varepsilon\sigma T^4$) - heat flux (W/m^2) expressed in Equation 4-3 [119]. When the object under investigation has a higher temperature than the ambient temperature, sections that have abnormalities i.e., cracks and inclusions will become apparent as hot spots on the thermometric readouts. On the other hand, when the surrounding temperature is higher than the object the affected sections will present as cold spots. The effect is due to the varying emissivity effected by the changes in thermal properties of the probed section. As a result, when heat flux is introduced into an object (steel, asphalt), higher than ambient temperature, this creates an unbalanced internal flux situation. However, Onsager relation dictates that evolution is on the steepest entropy ascent so does heat flux [126]. Because of the linearity of heat flux [126], propagation is caused. However, due to thermal insulation effected by the fatigue crack causes a sudden gradient in the continuous change in heat flux. The gradient impacts hot spots in the affected sections as illustrated in Figure 4.17 due to conduction and convection.

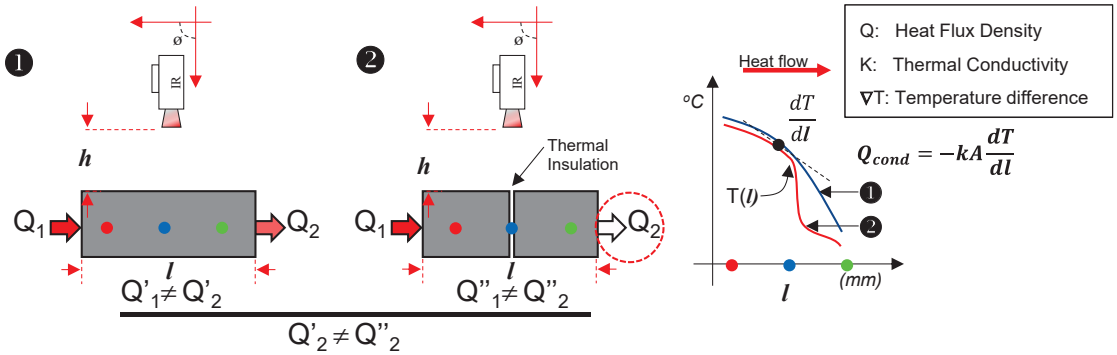

Figure 4.18. Thermal insulation situation

4.6.2. Heat Flux Diffusion in OSD setup

Using the Fourier law of thermal diffusion descripted in Equation 4.11, one-dimensional heat propagation is summarised to study the influence of urban heat profile on OSD that can aid in evaluating for fatigue cracks.

$$\left.\begin{aligned} \mathrm{Q} - KA\frac{\partial \mathrm{T}}{\partial x} \\ \mathrm{Q} - \mathrm{h}\frac{\partial \mathrm{T}}{\partial x} \end{aligned}\right\} = 0 \qquad \text{Eq. 4-11}$$

Where $\alpha = K/\rho c$ – Equation 4-2, Q heat flux density, $\partial \mathrm{T}/\partial x$ temperature gradient, h heat thermal coefficient and A area.

Due to urban heat profile the pavement section (asphalt concrete) above the OSD deck is heated up. Conduction and convection triggers 'horizontal heat transfer' [113] to propagate heat from the decking section to the trough rib as presented in Figures 4.17 and 4.18. The presence of fatigue crack at a certain depth interferes with heat propagation (cause a thermal insulation effect) prompting local surface temperature variation i.e., temperature gradient. These changes the linear propagation of heat fluxes causing localized flux differences detected by the ITT as thermal hot spots [113].

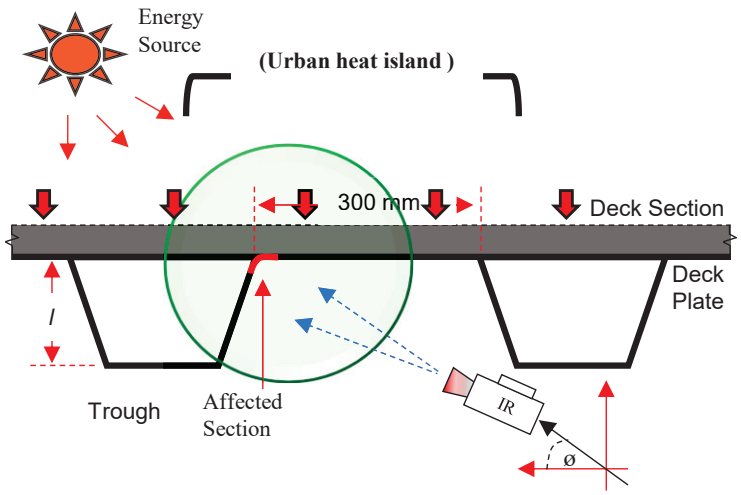

Figure 4.19. Typical illustration of heat transfer on OSD

4.7. Experimental Method

4.7.1. Field Experimentation Overview

Field experimentations were done involving capturing of through trough rib fatigue on a static domain as illustrated in Figures 4.18 and 4.19. The section was partitioned as A and B section characterised by 115 mm and 54 mm fatigue crack dimension with offsets of 80 mm and 33 mm from the deck plate to trough rib weld with stop-holes of approximately 30 mm diameter on either side respectively. The fatigue section was located at the mid span of the a suspension type bridge adopted as 'M–suspension bridge'. Prior to ICR treatment static IR images were captured from the in-service bridge (minimum of 5 thermal images per fatigue section A and B). The images were taken at approximately normal (90^{o}) to the fatigue sections and between 100 mm to 200 mm from the affected section. All other specification were similar to the laboratory experiment to ensure that the spatial resolution is consistent at 0.1-0.2mm/pixel. The IR camera setup and parameters were also corresponded to the laboratory experimentation. A similar process was repeated after treatment of the section. During each process penetrant testing was done to ensure reliability of the process.

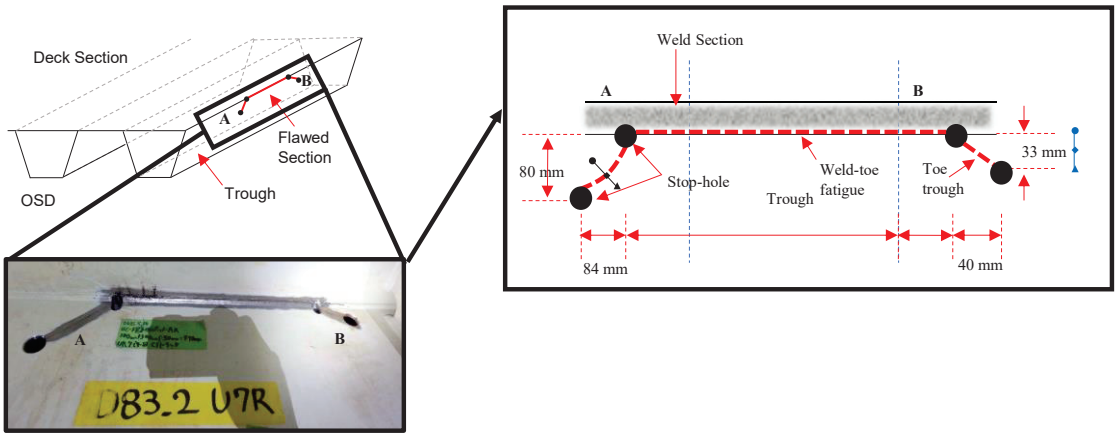

Figure 4.20. Affected trough section of the OSD.

Static thermography was similar plus the parameters to the laboratory experiment. However, the process was done in a passively with no source of heat flux excitation. The method of heat flux extraction also matched with the laboratory setup and process although at intervals of 2.5 – 5 and 5 – 10 mm.

4.8. Experimental Results and Discussion

4.8.1. Pre-ICR Condition

Figure 4.20a-e shows the pre-ICR situation. Road pavements are characteristic of high temperature (urban heat profile) i.e., the decking section composed of asphalt owing to heat conduction from both moving traffic and solar radiation [127]. This phenomenon causes the presumed 'horizontal heating angle' to propagate heat fluxes linearly at an angle of the trough rib section from the deck section of the to the OSD as illustrated in Figure 4.20c on the sound section of the trough.

However, the presence of through trough fatigue caused the impedance of thermal diffusion in sections beyond the affected section [4] causing a thermal gap effect. The flux Radiance (Q) readout of sections separated from the through trough fatigue crack ranged from 309.55 → 305.76 W/m^2 and 308.55 → 307.66 W/m^2 on sections above and below the fatigue crack 'A' respectively with the lower section having low fluxes than the corresponding upper section. The lowest radiances were observed on sections near the stop holes acting as a convectional heat boundary between the ambient section on the external and enclosed section of the trough-rib section. Similarly, fatigue crack 'B' had similar characteristics as 'A' with Radiance flux range of 308.52 → 306.89 W/m^2 and 308.04 → 307.28 W/m^2 above and below the fatigue crack respectively.

'A' had a mean radiance of 308.92 → 308.60 W/m^2 and 308.24 → 307.83 W/m^2 above and below as presented in Figure 4.20d, resulting to radiance gradient of 0.9377 → 0.6777. 'B' had a mean radiance of 308.36 → 307.87 W/m^2 and 307.90 → 307.58 W/m^2 above and below as illustrated in Figure 4.20e, resulting to radiance gradient of 0.4570 → 0.2860. The significant differences between the gradient are due to the dimensions of the fatigue cracks 'A' and 'B' that have varying radial heat dissipation with the former being high. Large fatigue sections tend to have a high dissipation due to the change in thermal properties in the section effecting high absorptivity ($\propto$) from Equation 4.1 in the fatigue crack fissures [111,128].

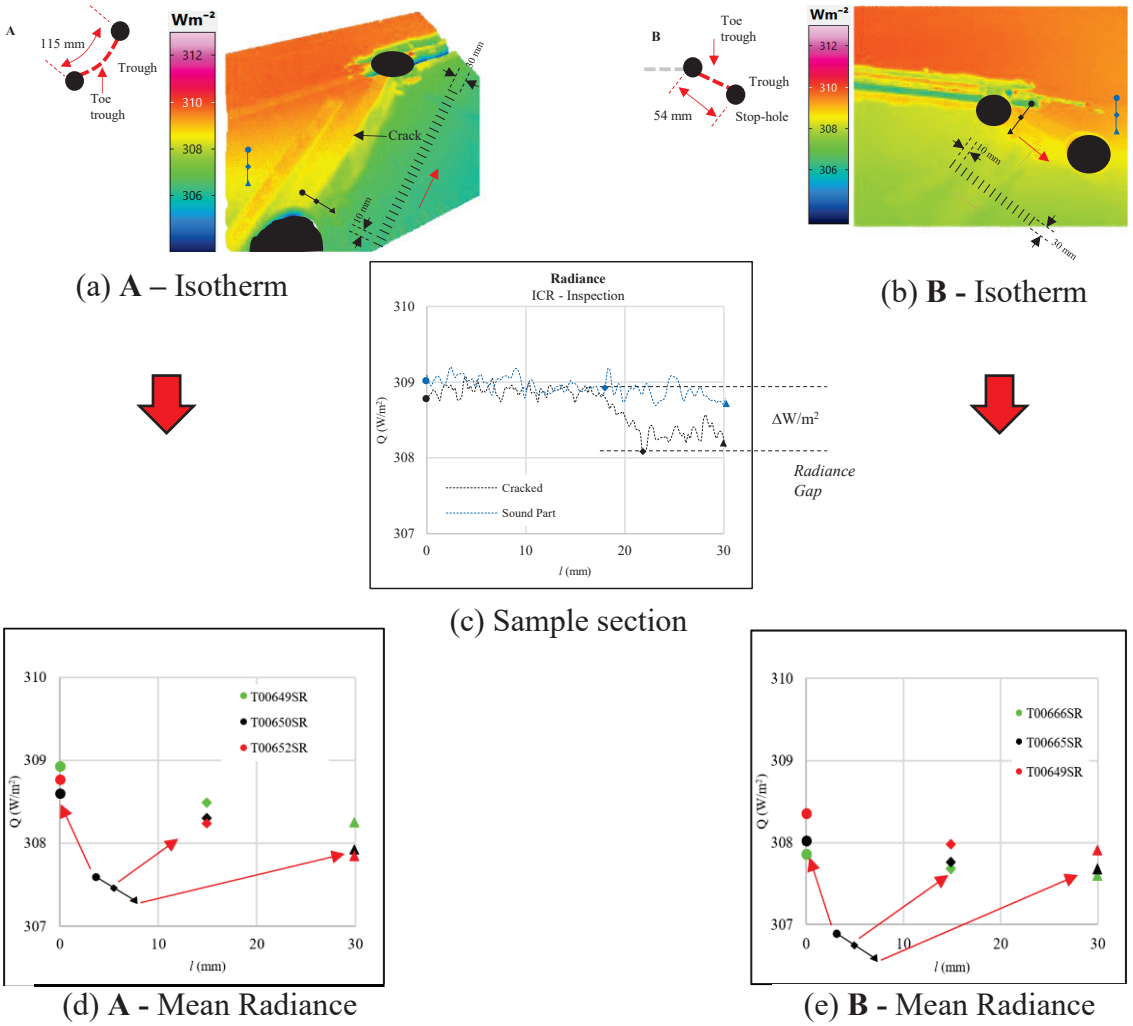

(a) **A** – Isotherm

(b) **B** - Isotherm

(c) Sample section

(d) **A** - Mean Radiance

(e) **B** - Mean Radiance

Figure 4.21. Trough section Isotherm Pre-ICR condition

4.8.2. Post-ICR Condition

Figure 4.21a-e shows the post-ICR situation. When the section is treated using ICR other than causing plastic situation in the section, it develops the thermal property of the section enhancing the propagation of the linear fluxes i.e., thermal diffusion. The formation of local hot zones around the fatigue section are inhibited giving a flux radiance range of 315.22 → 311.96 W/m^2 and 314.49 → 312.21 W/m^2 on 'A' and 313.21 → 309.24 W/m^2 and 313.21 → 311.21 W/m^2 on section 'B' with similar characteristic on the stop-hole section. The sections 'A' and 'B' had a mean radiance range of 314.68 → 318.86 and 314.08 → 313.35 W/m^2 as shown in Figure 4.21d as well as, 312.95 → 311.75 W/m^2 and 312.55 → 311.53 W/m^2 illustrated in Figure 4.21e respectively resulting into a flux rate of 0.5938 → 0.4931 and 0.3930 → 0.2180 in that order. The section presumably had a higher radiance compared to the pre-ICR experimentation. This was as a result of the transient behaviour of temperature on the decking section that changes due to the diurnal temperature profile [127]. Because of the evenness in the emissivity of the section as the heat fluxes comes from the decking section to the trough section there is a decaying transition in comparison to the gradient effect caused by the cracked section. However,

due to the groove effect of the ICR treatment the section has a reflective tendency hence limited radial dissipation making it appear as a cold spot [113]. The section illustrated in Figure 4.21c seems like a thermal chokepoint during the propagation of fluxes however there is an indication of the presence of propagation of fluxes by the resultant flux gradient.

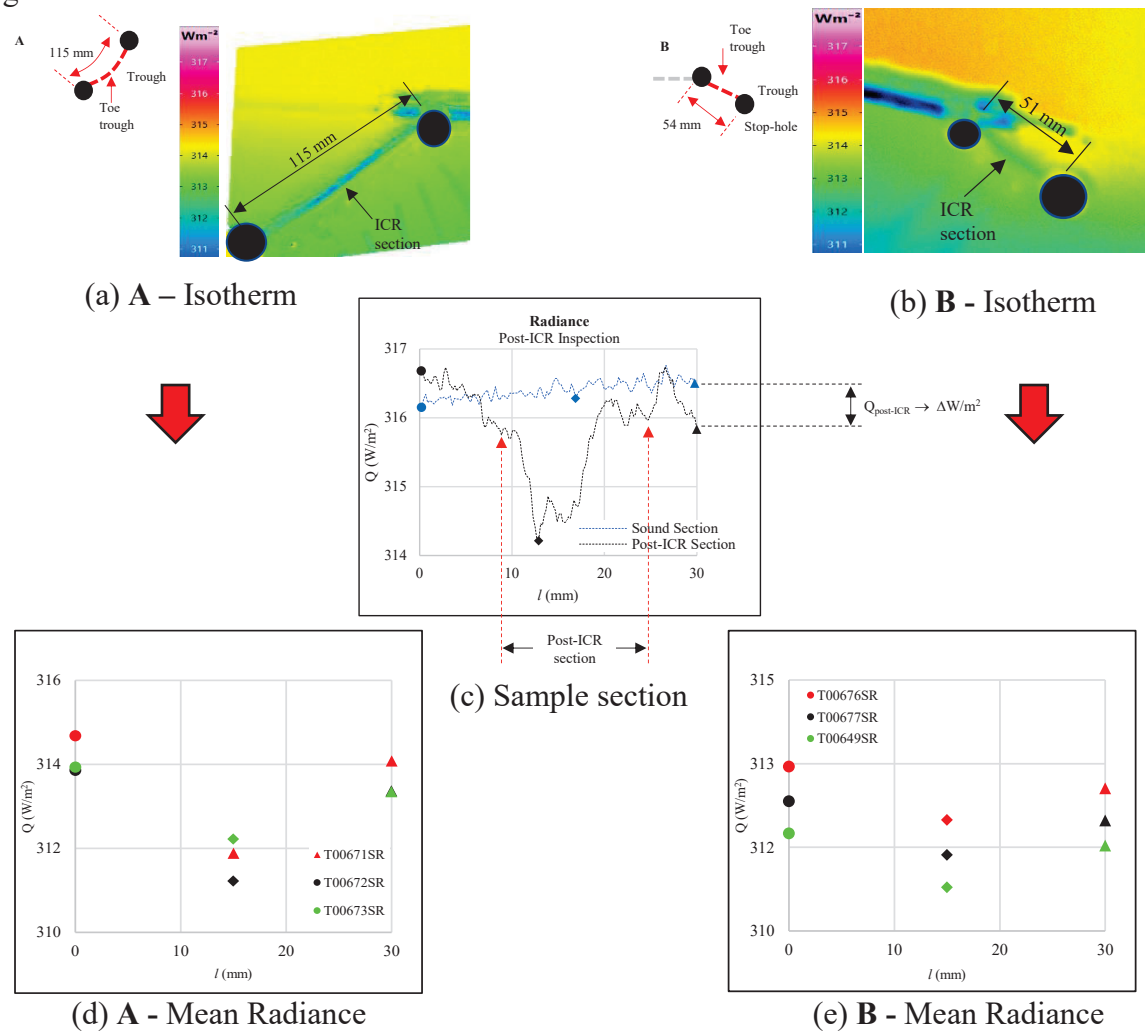

Figure 4.22. Trough section Isotherm Post-ICR condition

Table 4.4 relays the Gradient fluxes and its residuals. Residuals were determined from the mean heat fluxes of the various section of both the pre-ICR and post-ICR conditions. Positive residuals indicated adequate propagation of heat on the treated section. A negative residual would mean the section was unreliable and hence not well treated impeding heat diffusion in the region [113]. The sections both show there is propagative heat diffusion with residuals of 0.2074 and 0.0493 on 'A' and 'B' respectively with 'A' having a large residual due to the significant heat dissipation.

Table 4.4. Radiance Gradient and Residuals

$\partial T/\partial Q$	$\Delta Q_{pre\text{-}ICR}$				$\Delta Q_{post\text{-}ICR}$				Residual
	(i)	(ii)	(iii)	$\dot{x}$ $DQ_{pre\text{-}ICR}$	(i)	(ii)	(iii)	$\dot{x}$ $DQ_{pre\text{-}ICR}$	
A	0.6777	0.6792	0.9377	0.7649	0.5938	0.4931	0.5854	0.5574	0.2074
B	0.2860	0.3670	0.4570	0.3700	0.3930	0.3510	0.2180	0.3207	0.0493

Figure 4.22 shows the variation of radiance difference/gradient between pre-ICR situation versus post-ICR situation. The flux rate of the pre-ICR situation is higher than post-ICR due to the fatigue section that impedes heat diffusion in the section. The thermal gradient was observed to be significant which indicates that the rate of propagation was higher due to the presence of thermal insulation. However, on uniformity of emissivity the diffusion rate is slower approximately by 1.26 times. This indicates that cracked sections can be identified through their characteristic heat flux diffusion. The reliability of the section sections was also affirmed with penetrant testing indicating the reliability of the method.

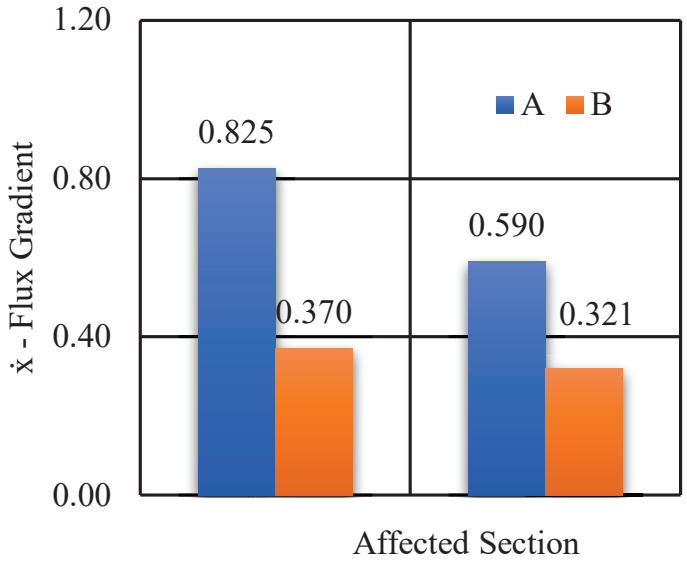

Figure 4.23. Reliability Check for ICR

4.9. Conclusions

4.9.1. Laboratory Investigation

The objective of this research was to propose using transient and static thermography for fatigue crack inspection and characterization for welded joints. Laboratory tests using an out-of-plane bending fatigue test machine were performed. AT was applied to inspect the surface fatigue crack in the welded joint. Also, MT and BM were performed to demonstrate the accuracy of the AT inspection. The primary outcomes of this study are demonstrated as follows.

1. From the transient thermography, fatigue cracks can be detected depending on the excitation source and observation of its decay in a transient domain.
2. From the static thermography, it was found that the radiant energy elliptically rises from the crack tips. Hence it directly correlates with fatigue crack propagation in the width direction.
3. From the above results, the width dimension (fatigue crack propagation in the plate width direction) can be quantitatively established from the amplitude drop.

4. From the comparison with MT and BM, it was realized that random errors are prevalent in AT. Therefore, controlling the sample is recommended to increase dimensional accuracy.
5. AT was limited to about 1.09 mm depth probe computed from the thermal diffusion length.
6. In summary, AT can be deployed as an alternative surface fatigue crack inspection and characterization method. However, the method is limited in depth direction.

4.9.2. On-site Experimentation

The objective of this research was to propose using passive thermography for inspection of the reliability of ICR treatment on OSD trough section. The conclusions of this study are demonstrated as follows.

1. Passive thermographic testing can identify the reliability of ICR treatment using the changes in the thermal properties of the fatigue crack section before and after treatment.
2. The method offers a sound approach for inspection to supplement the traditional methods.
3. The results of the testing indicate efficacy of the ICR approach on the through trough fatigue crack.

Chapter 5

Summary of Conclusions

5.1. Conclusions

This thesis aimed to investigate the structural condition of existing steel bridges based on Non-destructive evaluation. The constituent concerns were as follows with their corresponding solution with the intent to achieve the overall objective:

In **Chapter 2**: The prospects of NDE methods for assessing the current structural conditions, integrity, and redundancy are not well documented.

To determine the structural health condition based NDE of existing steel bridges the methodologies were reviewed and summarised to NDE approach for limited historical data (Acoustic and Vision based methods) and surface fatigue crack evaluation (magnetic, penetrant and thermal based methods). A framework was put forward for the conversion of temporary to semi-permanent or permanent steel bridges based on existing local manuals. A global perspective on the approaches was used for evaluating the degradation of steel structures and the NDE based approaches employed were also reviewed in a similar respect.

In **Chapter 3**: The shortcomings of the assumptions made from models fundamental in computer-based structural analysis programs are not supplemented and addressed.

This thesis proposed the development of a numerical model from onsite geometric, material properties and responses. The theoretical evaluation of structures needs accurate information about its material and geometric response and other factors such as dead loads. There is no other prudent alternative than to evaluate the structure through actual load testing. Therefore, the model was validated through in-situ static loading test with similar loading conditions and its support conditions first clarified. Idealised models are evaluated for accuracy by the corresponding dynamic and static load test measurements. Loading testing has become popular as an evaluation tool for acceptance proof of test. It has revealed to provide the following benefits: determination of the bearing capacity, deterioration/condition and safety of the structure.

In **Chapter 3**: The evaluation approaches of structural analysis of individual members in the ultimate limit state are conservative hence limited in adaptation.

Eurocode 3's prescription of analysis of structures in ultimate limit state as individual members is limited. Therefore, this shortcoming was addressed by linear and nonlinear buckling that is checking for resistance of critical members. Critical members were determined through field stresses, available literature, analytically through available locally used codes and modelling from onsite geometric measurement. The resistance of the members was evaluated for local buckling through cross-sectional classification. Linear and nonlinear buckling through the first eigenmode value to examine the serviceability and ultimate limit of the structure hence its bearing capacity, condition and structural health.

Thus, an approach for evaluation of temporary to permanent steel bridges was in this way proposed in Figure 5.1.

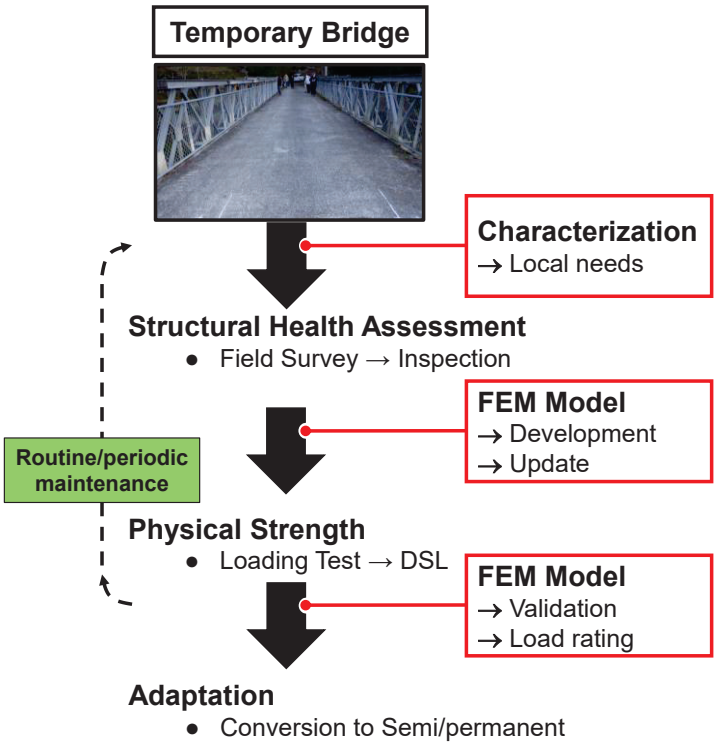

Figure 5.1. Proposed Evaluation framework.

In **Chapter 4**: The in-situ and ex-site fatigue crack inspection technologies are limited on inspection records and limited in capacity to evaluate fatigue cracks using the principles of fracture mechanics; thus, they are not simply integrative.

This thesis established T-NDE method can be an alternative deployable, non-invasive, reliable automated and sustainable screening technique. Perceived traditional methods cannot be used to evaluate for deterioration due to their inherent limitations to evaluate structural degradation based on fracture mechanics. Laboratory investigations employed transient and static thermography for evaluation of fatigue using isotherm field data. Subsequently, the former established parameters for field experimentations to evaluate for reliability of fatigue life extension using ICR treatment. The approach used passive approach through horizontal heat flux diffusion. Other than penetrant testing T-NDE was concluded to supplement other inspection methods (Magnetic and Penetrant Testing) for surface fatigue crack.

5.2. Recommendation

1. Non-destructive evaluation for limited historical data

The selection of critical location for sensors, type of information needed and instrumentation to acquire maximum global response in actual load testing is very challenging albeit the numerous benefits of load testing. Therefore, it is always recommended that redundancy checks be provided.

The conversion of temporary bridges to permanent or semi-permanent using the proposed framework can be well clarified using local manual to supplement for structural inspection.

2. Non-destructive evaluation for surface for fatigue crack

The evaluation of fatigue crack based on fracture mechanics is essential to establish the degradation of structure. Consequently, development of inspection procedures is relevant to acquire insight of the structural integrity.

5.3. Future works

1. Integration of artificial intelligence and infrared thermographic testing (ITT) for fatigue evaluation of welded sections.
2. Numerical analysis of thermographic based method for evaluation of deployed fatigue crack life extension approach.
3. The numerical evaluation of dynamic response of truss bridges to evaluate for weight in motion.
4. The evaluation of bailey bridge panels with panel pin connection vis-à-vis a monolithic model to clarify their various accuracies to examine for the bearing capacities.

References

1. Japan Road Bureau (MLIT). Roads in Japan 2018. *Minist. Land, Infastructure, Transp. Tour. Japan* **2018**, pp.2-39,42-46.
2. Japan Road Bureau (MLIT). Roads in Japan. *Minist. L. Tranasport Infrastruct. Tour.* **2021**, 1–39.
3. Fujino, Y.; Kawai, Y. Technical Developments in Structural Engineering With Emphasis on Steel Bridges in Japan. *J. JSCE* **2016**, *4*, 211–226, doi:10.2208/journalofjsce.4.1_211.
4. Sakagami, T. Remote Nondestructive Evaluation Technique Using Infrared Thermography for Fatigue Cracks in Steel Bridges. *Fatigue Fract. Eng. Mater. Struct.* **2015**, *38*, 755–779, doi:10.1111/ffe.12302.
5. Ministry of Land Transport Infrastructure and Tourism Road Maintenance in Japan : Problems and Solutions. *Minist. L. Transp. Infrastruct. Tour.* **2015**, 25.
6. Road Bureau (MLIT) Road Law Enforcement Regulations (Ministry of Construction Ordinance No. 25 of 1952). *MLIT* https://news.ge/anakliis-porti-aris-qveynis-momava.
7. Khounsida, T.; Nishikawa, T.; Nakamura, S.; Okumatsu, T.; Thepvongsa, K. Experimental and Analytical Study on Dynamic Behavior of Bailey Bridge. *Proc. Constr. Steel* **2020**, *28*, 771–777.
8. Ministry of Public Works and Transport Kingdom of Cambodia - Road Infrustructure Department Bridge Inspection Manual. *Gen. Dir. Tech.* **2018**, *1*, 210.
9. Yoshikawa, H.; Zhang, Z.; Instrumentation, A.D.; Plants, N.P. *Progress of Nuclear Safety for Symbiosis and Sustainability*; 2014; ISBN 9784431546092.
10. Ida, N.; Meyendorf, N. *Handbook of Advanced Nondestructive Evaluation*; 2020; ISBN 9783319265520.
11. Charles J, H. *Handbook of Nondestructive Evaluation*; 3rd ed.; McGraw Hill, New York, 2020; Vol. 3; ISBN 9781260441444.
12. Gorenc, B.E.; Tinyou, R.; Syam, A.A. *Steel Designers' Handbook*; 7, Ed.; UNSW Press: Sydney, 2005; ISBN 0 86840 573 6.
13. Chen, W.-F.; Duan, L. *Bridge Engineering Handbook*; wai-Fah Chen, Lian Duan, Eds.; CRC Press LLC, 2000; Vol. 37; ISBN 0849374340.
14. Chatterjee, S. *The Design of Modern Steel Bridges: Second Edition*; 2nd ed.; Blackwell Publishing: Oxford, 2008; ISBN 9780470774373.
15. Arya, C. *Design of Structural Elements*; 1994; ISBN 9789079658039.
16. Sanchez Corujo, A.; Ney, L. Footbridges Embraced by Their Users Available online: https://structurae.net/en/structures/dejima-bridge (accessed on 21 September 2022).
17. Klanker, G.; Stipanović Oslaković, I.; Škarić Palić, S. The Impact of Different Maintenance Policies on Ownerscosts: Case Studies from Croatia and the Netherlands. **2017**, 3.4-1-3.4-9, doi:10.5592/co/bshm2017.3.4.
18. Parivallal, S.; Narayanan, T.; Ravisankar, K.; Kesavan, K.; Maji, S. Instrumentation and Response Measurement of a Double-Lane Bailey Bridge during Load Test. *Strain* **2005**, *41*, 25–30, doi:10.1111/j.1475-1305.2004.00160.x.
19. King, W.S.; Wu, S.M.; Duan, L. Laboratory Load Tests and Analysis of Bailey Bridge Segments. *J. Bridg. Eng.* **2013**, *18*, 957–968, doi:10.1061/(asce)be.1943-5592.0000444.
20. Sun, S.; Lei, G.; Sun, Z. Dynamic and Static Load Tests on a Large-Span Rigid-Frame Bridge. *Math. Model. Eng. Probl.* **2019**, *6*, 409–414, doi:10.18280/mmep.060312.
21. AASHTO *AASHTO LRFD Bridge Design Specifications*; 8th ed.; American Association of State Highway and Transportation Officials, 2017; ISBN 1-56051-355-1.
22. Dong, C.; Bas, S.; Debees, M.; Alver, N.; Catbas, F.N. Bridge Load Testing for

Identifying Live Load Distribution, Load Rating, Serviceability and Dynamic Response. *Front. Built Environ.* **2020**, *6*, 1–14, doi:10.3389/fbuil.2020.00046.
23. Faber, M.H.; Val, D. V.; Stewart, M.G. Proof Load Testing for Bridge Assessment and Upgrading. *Eng. Struct.* **2000**, *22*, 1677–1689, doi:10.1016/S0141-0296(99)00111-X.
24. Lantsoght, E.O.L.; van der Veen, C.; de Boer, A.; Hordijk, D.A. State-of-the-Art on Load Testing of Concrete Bridges. *Eng. Struct.* **2017**, *150*, 231–241, doi:10.1016/j.engstruct.2017.07.050.
25. Lantsoght, E.O.L. Editorial: Diagnostic and Proof Load Tests on Bridges. *Front. Built Environ.* **2020**, *6*, doi:10.3389/fbuil.2020.586704.
26. Faber, M.H.; Val, D. V.; Stewart, M.G.; Lantsoght, E.O.L.; van der Veen, C.; Hordijk, D.A.; de Boer, A. Development of Recommendations for Proof Load Testing of Reinforced Concrete Slab Bridges. *Eng. Struct.* **2017**, *6*, 1677–1689, doi:10.1016/j.engstruct.2017.09.018.
27. Yi, P.; Vaghela, G.; Andrew, B. Condition Assessment And Load Rating of Arched Bailey Bridge. In Proceedings of the Austroads Bridge Conference; Sydney, 2014; pp. 1–11.
28. White, R.G.; Trétout, H. Acoustic Emission Detection Using a Piezoelectric Strain Gauge for Failure Mechanism Identification in Cfrp. *Composites* **1979**, *10*, 101–109, doi:10.1016/0010-4361(79)90011-9.
29. Khounsida, T.; Takafumi, N.; Shozo, N.; Toshihiro, O.; Khampaseuth, T. Study on Static and Dynamic Behavior of Bailey Bridge. *Adv. Struct. Eng. Mech.* **2019**, *46*, 9425–9428, doi:10.1016/j.matpr.2020.03.064.
30. J. Chakrabarty *Theory of Plasticity*; 3rd ed.; Elsevier Butterworth-Heinemann.: Burlington, 2006; ISBN 0750666382.
31. Berkovic, G.; Shafir, E. Optical Methods for Distance and Displacement Measurements. *Adv. Opt. Photonics* **2012**, *4*, 441, doi:10.1364/aop.4.000441.
32. Schneider, D. Terrestrial Laser Scanning for Area Based Deformation Analysis of Towers and Water Dams. *Proc. 3rd IAG/12th FIG Symp., Baden, Austria, May* **2006**, 22–24.
33. Connor, R.; Fisher, J.; Gatti, W.; Gopalaratnam, V.; Kozy, B.; Leshko, B.; McQuaid, D.L.; Medlock, R.; Mertz, D.; Murphy, T.; et al. Manual for Design, Construction, and Maintenance of Orthotropic Steel Deck Bridges. **2012**, 291.
34. Hopwood, T.; Gof, C.; Fairchild, J.; Palle, S. Nondestructive Evaluation of Steel Bridges : Methods and Applications. *Rep. No.KTC-16-26/SPR14-485-1F* **2016**, 1–95.
35. Mertz, D. *Steel Bridge Design Handbook - Design for Fatigue*; Washington, D.C., 2012; Vol. 12;.
36. Mizokami, Y.; Okumura, A.; Oto, T.; Izumi, Y.; Sakagami, T. 赤外線サーモグラフィを用いた温度ギャップ法による Ｕリブ鋼床版のビード貫通亀裂の自動検出と装置開発. **2018**, *64*, 573–582.
37. Worman, J. Index @ Www.Nationalboard.Org 2011.
38. Maros, H.; Juniar, S. *Inspection and Maintenance of Steel Girders*; 3rd ed.; Indian Railways Institute of Civil Engg: Pune, 2016; ISBN 2013206534.
39. Meyendorf, N.; Ida, N.; Singh, R.; Vrana, J. *Handbook of Nondestructive Testing*; 2005; Vol. 41; ISBN 9783030732059.
40. Yamada, Kentaro, Sitoshi Yamada, T.O. Development of a New Fatigue Testing Machine and Some Fatigue Tests for Plate Bending. *Int. Inst. Weld.* **2007**, *XIII*.
41. Furuya, Y. Visualization of Internal Small Fatigue Crack Growth. *Mater. Lett.* **2013**, *112*, 139–141, doi:10.1016/j.matlet.2013.09.015.
42. Furuya, Y.; Hirukawa, H.; Takeuchi, E. Gigacycle Fatigue in High Strength Steels. *Sci. Technol. Adv. Mater.* **2019**, *20*, 643–656, doi:10.1080/14686996.2019.1610904.
43. Department of the Army Washington - DC. Bailey Bridge. *F. Man. TM 5-277* **1986**,

2–349.
44. Godoi, F.C.; Prakash, S.; Bhandari, B.R. Prefabricated Steel Bridge Systems. FHWA SOLICITATION NO. DTFH61-03-R-00113. *Struct. Des. Rehabil.* 2005, *1*, 1–261.
45. Xu, Y.; Luo, Y.; Zhang, J. Laser-Scan Based Pose Monitoring for Guiding Erection of Precast Concrete Bridge Piers. *Autom. Constr.* **2022**, *140*, 104347, doi:10.1016/j.autcon.2022.104347.
46. Jatmiko; Psimoulis, P. Deformation Monitoring of a Steel Structure Using 3D Terrestrial Laser Scanner (TLS). *Digit. Proc. 24th EG-ICE Int. Work. Intell. Comput. Eng. 2017* **2017**, 168–177.
47. Lichti, D.D.; Gordon, S.J.; Stewart, M.P.; Franke, J.; Tsakiri, M. Comparison of Digital Photogrammetry and Laser Scanning. *ISPRS J. Photogramm. Remote Sens.* **2002**, *00*, 39–44.
48. Lee, J.J.; Shinozuka, M. A Vision-Based System for Remote Sensing of Bridge Displacement. *NDT E Int.* **2006**, *39*, 425–431, doi:10.1016/j.ndteint.2005.12.003.
49. Li, Z.W.; Liu, X.Z.; Lu, H.Y.; He, Y.L.; Zhou, Y.L. Surface Crack Detection in Precasted Slab Track in High-Speed Rail via Infrared Thermography. *MDPI-Materials* **2020**, *13*, 1–16, doi:10.3390/ma13214837.
50. Masatoshi, N.; Yuki, C.; Ichiro, A. Topological Optimum Shape of a Fundamental Module of the Periodic Structure and Cantilever Bridge. *J. Struct. Eng.* **2021**, *67A*, 90–98.
51. Chowdhury, I.S. Bailey Bridge Collapse with Stone-Laden Truck in Bhola Available online: https://www.observerbd.com/news.php?id=366184 (accessed on 27 December 2022).
52. Chajes, M.J.; Huang, J. Load Rating of Bridges Without Plans by Load Rating of Bridges Without Plans. **2007**, *19716*.
53. Duvnjak, I.; Bartolac, M.; Nilimaa, J.; Sas, G.; Blanksvärd, T.; Täljste, B.; Elfgren, L. Lessons Learnt from Full-Scale Tests of Bridges in Croatia and Sweden. *IABSE Symp. Nantes 2018 Tomorrow's Megastructures* **2018**, S24-127-S24-134, doi:10.2749/nantes.2018.s24-127.
54. American Association of State Highway and Transportation Officials (AASHTO). *AASHTO Bridge Element Inspection GuideManual*; Washington DC., 2010;
55. Ladurner, R.; Brandacher, G.; Steurer, W.; Schneeberger, S.; Bösmüller, C.; Freund, M.C.; Kreczy, A.; Königsrainer, A.; Margreiter, R. *Lessons to Be Learned from a Complicated Case of Rhino-Cerebral Mucormycosis in a Renal Allograft Recipient*; 2003; Vol. 16; ISBN 9780982085400.
56. Sindorf Trading Holland Ltd. Bailey Panel Bridge System - Triple Truss Single Storey Class 100 Available online: https://www.sindorf.nl/Portals/0/BAILEY BRIDGES.pdf.
57. nac Image Technology inc. MOVIAS Neo: Motion Analysis Available online: https://www.nacinc.jp/analysis/software/movias-neo/?add_list=MOVIAS+Neo (accessed on 4 November 2022).
58. Tokyo Measuring Instruments Ltd. *Precise and Flexible Strain Gauges*. Tokyo 2020, p. 96.
59. Japan Road Association. Fatigue of Steel Bridge. In *Japan Road Association*; Tokyo, Japan, 1997; pp. 47–309.
60. Joiner, C.J.H. The Story of the Bailey Bridge. *Proc. Inst. Civ. Eng. - Eng. Hist. Herit.* **2011**, *164*, 65–72, doi:10.1680/ehah.10.00002.
61. Gómez-Martínez, R.; Sánchez-García, R.; Escobar-Sánchez, J.A.; Arenas-García, L.M.; Mendoza-Salas, M.A.; Rosales-González, O.N. Monitoring Two Cable-Stayed Bridges during Load Tests with Fiber Optics. *Structures* **2021**, *33*, 4344–4358, doi:10.1016/j.istruc.2021.07.026.
62. Umekawa, Y.; Suganuma, H. Bridge Displacement Monitoring Using Acceleration Measurement and Development of Efficient Bridge Management System. *IABSE*

Symp. Nantes 2018 Tomorrow's Megastructures **2018**, S6-11-S6-18, doi:10.2749/nantes.2018.s6-11.
63. Tokyo Measuring Instruments Laboratory Co High Sensitive Displacement Transducer. Available online: https://tml.jp/e/product/transducers/displacement_high.html (accessed on 1 November 2022).
64. Engineers Class III -Department of Main Roads N.S.W. Repair and Strengthening of Timber Bridges. In *Repair and Strengthening of Timber Trusses.*; Wales, 1979; pp. 1–5.
65. Podder, D.; Chatterjee, S. *Introduction to Structural Analysis*; 1st ed.; CRC Press, Taylor & Francis Group: Florida, 2022; ISBN 9780367532727.
66. Bhavikatti, S.S. *Strength of Materials*; 4th ed.; VIKAS Publishing House PVT Ltd.: New Delhi, 2013; ISBN 978-93259-7157-8.
67. Bhavikatti, S.. *Structural Analysis - II*; 4th ed.; VIKAS Publishing House PVT Ltd.: New Delhi, 2013; ISBN 9789325968806, 9325968800.
68. Nautiyal, B.D. *Introduction to Structural Analysis*; New Age International: New Delhi, 2001; ISBN 9788122413168, 8122413161.
69. Ghavami, P. *Mechanics of Materials: An Introduction to Engineering Technology*; Springer: New York, 1956; Vol. 78; ISBN 9783319075716.
70. Gross, D.; Ehlers, W.; Wriggers, P.; Schröder, J.; Müller, R. Mechanics of Materials - Formulas and Problems: Engineering Mechanics 2. *Mech. Mater. - Formulas Probl. Eng. Mech. 2* 2016, 1–212.
71. Dr. R.K. Bansal *A Textbook of Strength of Materials*; 4th ed.; Laxmi Publications, 2009; ISBN 8131800008, 9788131800003.
72. Bridge Deflection Measurement Service INTEGRAL PLUS® | TTES Co., Ltd. Available online: https://ttes.co.jp/service/integral/ (accessed on 1 September 2022).
73. Umekawa, Y.; Hisatada, S.; Kinoshita, K.; Ono, T. A Study on Displacement Monitoring of Bridges Using Acceleration Data Associated with Vehicle Traffic. In Proceedings of the The 72nd Annual Conference of Japan Society of Civil Engineers; JSCE: Kyushu, 2017; Vol. 8, pp. 699–700.
74. Shimosato, T.; Tai, M.; Hisatada, S.; Umekawa, Y.; Hiyama, Y. Deflection Measurement of Bridge Using TWM System. In Proceedings of the Japan Society of Civil Engineers Western Branch Okinawa Meeting, 7th Technical Research Conference; JSCE: Okinawa, 2018; pp. 146–147.
75. Ma, M.J. Dynamic Load Test Analysis for Continuous Steel Bridge. *Appl. Mech. Mater.* **2013**, *275–277*, 1078–1081, doi:10.4028/www.scientific.net/AMM.275-277.1078.
76. Paeglite, I.; Paeglitis, A.; Smirnovs, J. Dynamic Amplification Factor for Bridges With Span Length From 10 To 35 Meters. *Eng. Struct. Technol.* **2015**, *6*, 151–158, doi:10.3846/2029882x.2014.996254.
77. Bruls, A.; Calgaro, J. A.; Mathieu, H.; Prat, M. ENV1991 –Part 3: The Main Models of Traffic Loads on Bridges: Background Studies. IABSE Colloquim, Delft. The Delft IABSE, 1996, 215–228.
78. Aashto *AASHTO LRFD Bridge Design Specifications*; 2010; ISBN 9781560514510.
79. Yuji, I.; Nakamura, S.; Kusaba, T.; Nishikawa, T. Field Measurement and Structural Analysis of Bailey Bridge for Understanding Fundamental Load-Bearing Configuration. In Proceedings of the Japan Society of Civil Engineering- West; I-023, JSCE, 2022; pp. 45–46.
80. Benčat, J.; Kohár, R. Bridges Subjected to Dynamic Loading. *Bridg. Eng.* **2018**, doi:10.5772/intechopen.73193.
81. Kalin, J.; Žnidarič, A.; Anžlin, A.; Kreslin, M. Measurements of Bridge Dynamic Amplification Factor Using Bridge Weigh-in-Motion Data. *Struct. Infrastruct. Eng.*

2022, *18*, 1164–1176, doi:10.1080/15732479.2021.1887291.
82. Plachý, T.; Polák, M.; Ryjáček, P. Assessment of an Old Steel Railway Bridge Using Dynamic Tests. *Procedia Eng.* **2017**, *199*, 3053–3058, doi:10.1016/j.proeng.2017.09.555.
83. Umekawa, Y.; Hisatada, S.; Kinoshita, K.; Ono, T. A Study on Displacement Response Monitoring Using Acceleration Response. In Proceedings of the JSCE Western Branch Okinawa Meeting, 6th Technical Research Presentation; JSCE: Onna, Okinawa; Vol. 8, pp. 88–89.
84. Association of Structural Engineers of The Philippines National Structural Code of the Philippines. *Nscp C101-15* 2015, 1–1008.
85. Garden Reach Shipbuilders and Engineers Limited Kolkata 2016, pp. 1–93.
86. CEN Design of Steel Structures - Part 1-1: General Rules and Rules for Buildings. 2011, *1–1*.
87. CEN *Eurocode 1: Actions on Structures – Part 2: Traffic Loads on Bridges on Bridges.*; 2003; Vol. 1;.
88. Tian, Q.; Hang, C.; Wan, Z.; Zou, Y. Local Optimization Analysis of Bailey Beam Bracket Based on Multiscale Model. *Key Eng. Mater.* **2019**, *815 KEM*, 229–234, doi:10.4028/www.scientific.net/KEM.815.229.
89. Vaidya, S.M. *Bridge Bearings*; 2nd ed.; Indian Institute of Civil Engineering.: Pune, 2014;
90. Ramberger, G.; Robra, J. *Structural Bearings and Expansion Joints for Bridges*; 2003; Vol. 13; ISBN 3857481056.
91. Holmes, J.D. *Wind Loading of Structures*; 2nd ed.; Spon Press is an imprint of the Taylor & Francis Group: New York, 2018; ISBN 041924610X.
92. Çiftçioğlu, A.Ö.; Yildizel, S.A.; Yildirim, M.S.; Doğan, E. Wind Load Design of Hangar-Type Closed Steel Structures with Different Roof Pitches Using Abaqus CAE Software. *TEM J.* **2017**, *6*, 336–341, doi:10.18421/TEM62-19.
93. LRFD Steel Girder SuperStructure Design Example - LRFD - Structures - Bridges & Structures - Federal Highway Administration Available online: https://www.fhwa.dot.gov/bridge/lrfd/us_ds8.cfm#designstep86_5 (accessed on 19 October 2022).
94. Poddaeva, O.; Fedosova, A.; Gribach, J. The Study of Wind Effects on the Bridge Constructions. *E3S Web Conf.* **2019**, *97*, doi:10.1051/e3sconf/20199703030.
95. Ochshorn, J. *Structural Elements for Architects and Builders: Design of Columns, Beams, and Tension Elements in Wood, Steel, and Reinforced Concrete*; Elsevier: New York, 2009; ISBN 9781856177719.
96. American Society of Civil Engineers. *American Society of Civil Engineers Design Loads on Structures During Construction American Society of Civil Engineers Design Loads on Structures During Construction*; American Society of Civil Engineers, Structural Engineering Institute: Virginia, 2003; ISBN 0784406189.
97. Kumamoto, T. Seismic Hazard Maps of Japan and Computational Differences in Models and Parameters. *Geogr. Rev. Japan, Ser. B* **1999**, *72*, 135–161, doi:10.4157/grj1984b.72.135.
98. Dassault Systèmes Simulia Abaqus CAE User's Manual (6.12). *Manuals* 2012, 1174.
99. Gibe, H.A.; Tamai, H.; Sonoda, Y. Numerical Study on Failure Process and Ultimate State of Steel Bearing under Combined Load. *Heliyon* **2020**, *6*, e03764, doi:10.1016/j.heliyon.2020.e03764.
100. Miki, C. *Civil Engineering: Steel Structures*; 10th ed.; Kyoritsu Publishing, 2000; ISBN 9784320073913.
101. Civil Engineering and Building Structures Standards Policy Committee *British Standard 5950-1:2000: Structural Use of Steel Work in Buildings Part 1*; BSI, 2001; ISBN 0 580 33238 X.
102. Lebet, J.; Hirt, M.A.; Couchman, G. Steel Bridges.

103. Jung, M. jae; Park, B. cheol; Bae, J. hoon; Shin, S. chul PAUT-Based Defect Detection Method for Submarine Pressure Hulls. *Int. J. Nav. Archit. Ocean Eng.* **2018**, *10*, 153–169, doi:10.1016/j.ijnaoe.2017.06.002.
104. Avdelidis, N.P.; Hawtin, B.C.; Almond, D.P. Transient Thermography in the Assessment of Defects of Aircraft Composites. *NDT E Int.* **2003**, *36*, 433–439, doi:10.1016/S0963-8695(03)00052-5.
105. Kretzmann, JE; Venter, G. Thermography on Composite Materials. *R D J. South African Inst. Mech. Eng.* **2016**, *32*, 35–43.
106. Ida, N.; Meyendorf, N. *Handbook of Advanced Nondestructive Evaluation*; 2020; ISBN 9783319265520.
107. Kubo.T, T.; Sakagami Development of New Crack Identification Technique Based on Near-Tip Singular Electrothermal Field Measured by Lock-in Infrared Thermography 2001, 528–534.
108. Ramzan, B.; Malik, M.S.; Martarelli, M.; Ali, H.T.; Yusuf, M.; Ahmad, S.M. Pixel Frequency Based Railroad Surface Flaw Detection Using Active Infrared Thermography for Structural Health Monitoring. *Case Stud. Therm. Eng.* **2021**, *27*, doi:10.1016/j.csite.2021.101234.
109. Sparrow. S. H. and Lin. S. H Absorption of Thermal Radiation in a V-Groove Cavity," International Journal of Heat and Mass Transfer. *Int. J. Heat Mass Transf.* **1962**, *5*, 1111–1115.
110. Yamada, Kentaro, Sitoshi Yamada, T.O. A New Fatigue Machine for Plate Bending. *Proc. 9th Korea-Japan Jt. Symp. Steel Bridg. Incheaon. Korea* **2007**, 22–24.
111. Li, Z.W.; Liu, X.Z.; Lu, H.Y.; He, Y.L.; Zhou, Y.L. Surface Crack Detection in Precasted Slab Track in High-Speed Rail via Infrared Thermography. *Materials (Basel).* **2020**, *13*, 1–16, doi:10.3390/ma13214837.
112. Development of a New Fatigue Testing Machine and Some Fatigue Tests for Plate Bending.
113. Yang, J.; Wang, W.; Lin, G.; Li, Q.; Sun, Y.; Sun, Y. Infrared Thermal Imaging-Based Crack Detection Using Deep Learning. *IEEE Access* **2019**, *7*, 182060–182077, doi:10.1109/ACCESS.2019.2958264.
114. Rodríguez-Martín, M.; Lagüela, S.; González-Aguilera, D.; Martinez, J. Prediction of Depth Model for Cracks in Steel Using Infrared Thermography. *Infrared Phys. Technol.* **2015**, *71*, 492–500, doi:10.1016/j.infrared.2015.06.013.
115. Broberg, P. Surface Crack Detection in Welds Using Thermography. *NDT E Int.* **2013**, *57*, 69–73, doi:10.1016/j.ndteint.2013.03.008.
116. Kinoshita, K.; Arakawa, S. Out-of-Plane Gusset Welded Joints Subject to Plate Bending by XFEM Fatigue Crack Growth Path Simulation. *58*.
117. Kawahara, M.; Kurihara, M. Fatigue Crack Growth From a Surface Flaw. *Fracture* **1978**, *2 B*, 1361–1373, doi:10.1016/b978-0-08-022140-3.50096-3.
118. Lahiri, B.B.; Bagavathiappan, S.; Saravanan, T.; Rajkumar, K. V; Kumar, A.; Philip, J.; Jayakumar, T. Defect Detection in Weld Joints by Infrared Thermography. *Int. Conf. NDE Steel allied Ind. NDESAI* **2011**, 191–197.
119. Ranjit, S.; Kim, W.T. Detection of Subsurface Defects in Metal Materials Using Infrared Thermography; Image Processing and Finite Element Modeling. *J. Korean Soc. Nondestruct. Test.* **2014**, *34*, 128–134, doi:10.7779/jksnt.2014.34.2.128.
120. Streza, M.; Fedala, Y.; Roger, J.P.; Tessier, G.; Boue, C. Heat Transfer Modeling for Surface Crack Depth Evaluation. *Meas. Sci. Technol.* **2013**, *24*, doi:10.1088/0957-0233/24/4/045602.
121. Al-Karawi, H.; von Bock und Polach, R.U.F.; Al-Emrani, M. Fatigue Life Extension of Existing Welded Structures via High Frequency Mechanical Impact (HFMI) Treatment. *Eng. Struct.* **2021**, *239*, 112234, doi:10.1016/j.engstruct.2021.112234.
122. Zhang, Q.H.; Bu, Y.Z.; Li, Q. Review on Fatigue Problems of Orthotropic Steel

Bridge Deck. *Zhongguo Gonglu Xuebao/China J. Highw. Transp.* **2017**, *30*.
123. Yamada, K.; Ishikawa, T.; Kakiichi, T. Rehabilitation and Improvement of Fatigue Life of Welded Joints by ICR Treatment. *Adv. Steel Constr.* **2015**, *11*, 294–304, doi:10.18057/IJASC.2015.11.3.4.
124. Al-Karawi, H.; Al-Emrani, M. The Efficiency of HFMI Treatment and TIG Remelting for Extending the Fatigue Life of Existing Welded Structures. *Steel Constr.* **2021**, *14*, 95–106, doi:10.1002/stco.202000053.
125. T. L. Anderson *Fracture Mechanics: Fundamentals and Applications*; 3rd ed.; Taylor & Francis Group, LLC: New York, 2005; ISBN 978-1-4200-5821-5.
126. Monroe, C.W.; Newman, J. An Introduction to the Onsager Reciprocal Relations. *Chem. Eng. Educ.* **2007**, *41*, 233–238.
127. Yoshida, N.; Nishimura, T.; Hino, Y. Experimental Study on Association of Surface Characteristics of Road Pavement with Surface Temperature. *J-STAGE* **2000**, *29*, 66-74. (in Japanese).
128. Ranjit, S.; Kim, W.T. Detection of Subsurface Defects in Metal Materials Using Infrared Thermography; Image Processing and Finite Element Modeling. *J. Korean Soc. Nondestruct. Test.* **2014**, *34*, 128–134, doi:10.7779/jksnt.2014.34.2.128.